UNIVERSITÀ
DEGLI STUDI
DI PADOVA

UNIVERSITY OF STUDIES OF PADOVA

DEPARTMENT OF PHYSICS AND ASTRONOMY
'GALILEO GALILEI'

DOCTORAL SCHOOL OF RESEARCH IN ASTRONOMY

CYCLE XXVII
PHD THESIS

THE IMPACT OF STELLAR EVOLUTION AND DYNAMICS ON THE FORMATION OF COMPACT-OBJECT BINARIES

Director of the PhD school: Ch.mo Prof. Giampaolo Piotto

Supervisors: Dr. Michela Mapelli

Prof. Giuseppe Tormen

PhD Student: Brunetto Marco Ziosi

2012-2015

UNIVERSITÀ
DEGLI STUDI
DI PADOVA

UNIVERSITÀ DEGLI STUDI DI PADOVA

DIPARTIMENTO DI FISICA E ASTRONOMIA
'GALILEO GALILEI'

SCUOLA DI DOTTORATO DI RICERCA IN ASTRONOMIA

CICLO XXVII

TESI DI DOTTORATO

THE IMPACT OF STELLAR EVOLUTION AND DYNAMICS ON THE FORMATION OF COMPACT-OBJECT BINARIES

Direttore della scuola di Dottorato: Ch.mo Prof. Giampaolo Piotto

Supervisors: Dott.ssa Michela Mapelli

Prof. Giuseppe Tormen

Studente di Dottorato: Brunetto Marco Ziosi

2012-2015

“Simplicity is the ultimate sophistication.”
(Leonardo da Vinci)

“If you want to go fast, go alone.
If you want to go far, go together.”
(African proverb)

“If fifty million people say a foolish thing,
it is still a foolish thing.”
(Anatole France)

CONTENTS

LIST OF FIGURES

List of Tables

SUMMARY

The aim of this work is to study the formation and evolution of double compact-object binaries (DCOBs, i.e. black hole-black hole, black hole-neutron star and neutron star-neutron star binaries) in young (< 100 Myr) dense ($\gtrsim 10^3$ star/pc^3) star clusters (YSCs). DCOBs, when merging, are expected to be powerful sources of gravitational waves (GWs) observable by Virgo and LIGO detectors. Best merger candidates (BMCs), i.e. those sources with a chance to be observed, have a coalescence timescale shorter than one Hubble time ($t_{\rm H}$) and produce a signal strong enough (strain $h \gtrsim 10^{-21}$) to be visible from Earth. This project is particularly timely because the second generation Virgo and LIGO detectors are expected to start operating in 2016. The importance of choosing YSCs as environment for this study has two motivations. First, YSCs are the place where $\gtrsim 80\%$ of the stars form, in particular the most massive ones. The remnants of these massive stars will dominate the dynamics of the cluster and will form the kind of binaries we are looking for. This makes YSCs the best environment where to look for DCOBs. Second, YSCs are collisional environments (2-body relaxation timescale $t_{\rm relax} \sim 10\,{\rm Myr}\left(\frac{M_{\rm tot}}{3500\,{\rm M}_\odot}\right)^{1/2}\left(\frac{r_{\rm hm}}{1\,{\rm pc}}\right)^{3/2}$, where $M_{\rm tot}$ and $r_{\rm hm}$ are the total mass and the half mass radius of the YSC, respectively). Close encounters between single stars and binaries may result in the binary getting closer or even in an exchange, i.e. the single star taking the place of one of the binary members. In the field (i.e. the galactic disk), instead, a binary exists only if the two stars were born already bound, can shrink only because of stellar and binary evolution (GW emission, common envelope, ...) and does not undergo exchanges. Thus, dynamical processes

have a fundamental role in shaping the DCOB population in YSCs. Moreover, YSCs have a short lifetime: they are thought to dissolve into the galactic disk in $\mathcal{O}(10^2)$ Myr, releasing their DCOB content into the disk. Thus, the estimate of the population of GW source candidates in the field has to take into account the population of DCOBs in YSCs.

In order to study the population of DCOBs in YSCs, I performed and analyzed $\gtrsim 10^3$ direct N-body simulations coupled with stellar evolution recipes of YSCs. The simulations were run with the software environment STARLAB (Portegies Zwart et al., 2001), modified to include up-to-date metallicity dependent stellar evolution recipes (Mapelli and Bressan, 2013). These recipes take into account metallicity dependent stellar winds and the possibility that a massive star collapses directly to a black hole (BH), without supernova (SN) explosion. This BH formation process, called "direct collapse" or "failed SN", allows the formation of more massive BHs.

In addition, I developed SLTOOLS, a suite of programs to help the production and management of simulations. They provide tools to automate most of the steps needed to obtain clean datasets ready for the analysis, including an automated quality control and error management.

In my analysis, I traced the life of compact-object binaries and I investigated the impact of dynamical interactions, metallicity and structural properties of the host YSCs on the population of BMCs.

I focused on how many DCOBs per YSC are produced (~ 4 stable BH-BH binaries, ~ 1 unstable BH-BH binaries, ~ 0.1 NS-NS and ~ 0.1 BH-NS per YSC along the entire simulation) and how this quantity changes with time: hard BH-BH binaries grows monotonically in time from 0 to $\langle n_{\rm BH-BH,hard}\rangle_{SC}(t = 100\,{\rm Myr}) \sim 0.2-0.4$ while soft BH-BH binaries show a peak (after the core collapse, which occurs at different times for different densities) and then decrease to ~ 0.05.

I found that $\gtrsim 90\%$ of BH-BH binaries form from exchanges. This result indicates that BHs are extremely efficient in finding companions through dynamical exchanges.

Moreover, low metallicity, thanks to the higher masses allowed for the remnants,

favors the early formation of these heavy and stable BH-BH binaries.

I also found that NS-NS binaries are, at least, ten times less numerous than BH-BH ones, despite the initial mass function.

My analysis showed that BH-BH formation is favored also by high density ($\sim 3\times10^3\,M_\odot pc^{-3}$) and high concentration (dimensionless central potential $W_0 \gtrsim 3$), while it is not very sensitive to primordial binary fraction.

However, it is worth noting that only 23% of BH-BH BMCs come from exchanges, while the rest are primordial binaries. On the other hand, dynamical encounters are important also in primordial binaries, because they are responsible for the shrinking of BH-BH binary semi-major axis (SMA) a. Then, BH-BH binaries are able to reach values of the SMA short enough that the binary evolution is dominated by GW emission. Without dynamics, this process would have taken much more time. As to NS-NS binaries, I found that only 6% of NS-NS BMCs come from exchanges. The fact that the vast majority of NS-NS binaries are primordial is consistent with our expectations, because it is unlikely for a NS to acquire a NS companion if the dynamical interactions are dominated by BHs.

Thus, it is interesting that we found even also some NS-NS binaries (6%) formed through exchanges.

I also analyzed DCOB properties, i.e. masses and chirp masses ($m_{\rm chirp} = \frac{(m_1 m_2)^{3/5}}{(m_1+m_2)^{1/5}}$, where m_1 and m_2 are the masses of the two members of the binary), SMAs, and eccentricities. In my simulations, BHs are heavier at low metallicity (maximum BH mass $\sim 80\,M_\odot$ at $Z = 0.01\,Z_\odot$) because of the stellar evolution and failed SN recipes I adopted. In addition, even more massive BHs can form because of mergers with stellar companion. Thus, the maximum BH mass I find in BH-BH binaries is $\sim 125\,M_\odot$.

This trend is reflected by the chirp mass values which are up to $\sim 80\,M_\odot$. However, the maximum chirp mass for a BMC binary is quite lower ($\sim 40\,M_\odot$) and the rest of BMCs chirp masses are below $20\,M_\odot$.

Semi-major axis distributions show that, while NS-NS binaries are much less numerous than BH-BH, their SMA are much shorter (minimum SMA for NS-NS

$a_{\rm min,NS-NS} \sim 10^{-3}$ AU compared to $a_{\rm min,BH-BH} \sim 10^{-1}$ AU). This is a selection effect: the NS-NS binaries I found come from binaries close enough to survive two SN explosions and dynamical encounters.

This result is reflected by the coalescence timescale (time a binary needs to merge only because GWs emission, $t_{\rm GW} \propto {a^4(1-e^2)^{7/2}}/{m_1 m_2 m_{\rm tot}}$, where G is the gravitational constant, m_1 are m_2 the masses of the two members of the binary, a is the semi-major axis and e is the eccentricity): NS-NS binaries have shorter coalescence timescales ($t_{\rm GW,min,NS-NS} \sim 10^{-5}$ Gyr compared to $t_{\rm GW,min,BH-BH} \sim 10^{-1}$ Gyr for BH-BH). In fact, I found that 76% of NS-NS BMC binaries merge during the simulations (36% of all the NS-NS binaries), while none of BH-BH binaries does.

While there is not observational evidence of BH-BH binaries in our Galaxy, we observe 10 NS-NS binaries (Lorimer, 2008).

I compared the observed NS-NS binaries properties (period, eccentricity and coalescence timescale) to the ones from my simulations. The agreement is very good. The only differences can be found at the shortest and longest periods. The differences are due to selection effects: at very short periods ($\lesssim 2$ hours) NS-NS binaries merge very fast and it is hard to observe them in this state, while the longest periods ($\gtrsim 10^3$ days) are too long to be observed since now.

Finally, I derived the expected merger rate from my simulations, and I investigated whether it depends on YSC properties (mass, density, concentration primordial binary fractions, metallicity). I found no significant dependence of BH-BH merger rates on the structural properties of YSCs, within the considered ranges. However, uncertainties are still quite large.

The global merger rate for BH-BH binaries derived from my simulations is $R_{\rm merger,BH-BH} = 0.0019 \pm 0.0007\,{\rm Mpc^{-3}Myr^{-1}}$. The final BH-BH detection rate shows a dependence (though not very significant because of the large uncertainties) on the density and concentration of the host YSC: they are higher for more dense and concentrated clusters, in agreement with the average number of BH-BH binaries produced during the cluster life. Moreover, the BH-BH detection rate anti-correlates with the primordial binary fraction. This result

needs further investigations. The global detection rate for BH-BH binaries is $R_{\mathrm{detection,BH-BH}} = 0.8 \pm 0.2\,\mathrm{yr}^{-1}$. Merger and detection rates for NS-NS and BH-NS are $R_{\mathrm{merger,NS-NS}} = 0.258 \pm 0.005\,\mathrm{Mpc}^{-3}\mathrm{Myr}^{-1}$, $R_{\mathrm{merger,BH-NS}} = 0.0009 \pm 0.0002\,\mathrm{Mpc}^{-3}\mathrm{Myr}^{-1}$, $R_{\mathrm{detection,NS-NS}} = 0.65 \pm 0.01\,\mathrm{yr}^{-1}$, $R_{\mathrm{detection,BH-NS}} = 0.0107 \pm 0.0006\,\mathrm{yr}^{-1}$ for NS-NS and BH-NS, respectively.

The merger and detection rates of BH-BH and NS-NS binaries are consistent with the pessimistic rates provided by Virgo and LIGO collaboration (Abadie et al., 2010). The BH-NS merger and detection rate are even lower than the most pessimistic prediction in literature because BH-NS mergers are disfavored by dynamical processes that favor BH-BH production at the expense of BH-NS ones.

RIASSUNTO

L'obiettivo di questo lavoro è studiare la fomazione ed evolutione di binarie di oggetti compatti (DCOBs, ovvero buchi neri binari, stelle di neutroni binarie e binarie buco nero-stella di neutroni) in ammassi stellari (YSCs) giovani (< 100 Myr) e densi ($\gtrsim 10^3$ stelle/pc^3). La teoria prevede che i DCOBs, coalescendo, diventino potenti sorgenti di onde gravitazionali (GWs) osservabili dai rivelatori Virgo and LIGO. I migliori candidati per l'osservazione (BMCs), hanno un tempo scala di coalescenza minore di un tempo di Hubble ($t_{\rm H}$) e producono un segnale sufficientemente forte (strain $h \gtrsim 10^{-21}$) da essere osservabile da Terra. Questo è proprio il momento giusto per svolgere un progetto del genere in quanto la seconda generazione dei rivelatori Virgo e LIGO inizierà le osservazioni nel 2016. La scelta degli YSCs come ambiente per lo studio dei DCOBs è particolarmente importante per due motivazioni. Innanzitutto, gli YSCs sono il luogo in cui $\gtrsim 80\%$ delle stelle si forma, in particolare le più massive. Gli oggetti compatti che si formano alla morte di queste stelle massive dominano la dinamica del cluster e formano il tipo di binarie che vogliamo studiare. Questo rende gli YSC il migliore ambiente dove cercare DCOBs. Secondo, gli YSCs sono collisionali (tempo scala di rilassamento a due corpi $t_{\rm relax} \sim 10\,{\rm Myr}\left(\frac{M_{\rm tot}}{3500\,{\rm M}_\odot}\right)^{1/2}\left(\frac{r_{\rm hm}}{1\,{\rm pc}}\right)^{3/2}$, dove $M_{\rm tot}$ e $r_{\rm hm}$ sono la massa totale e il raggio di metà massa dello YSC, rispettivamente). Incontri ravvicinati tra singole stelle e binarie possono rendere la binaria più stretta o perfino portare la stella singola a prendere il posto di uno dei componenti della binaria. Nel campo (disco galattico), invece, una binaria esiste solo se le due stelle che la compongono si sono formate già legate, piò stringersi solo a causa di

effetti legati all'evolutione stellare o in binaria (emissione di GW, common envelope, ...) e non può essere oggetto di scambi dinamici. Per queste ragioni, i processi dinamici hanno un ruolo fondamentale nel dare forma alla popolazione di DCOBs negli YSCs. Inoltre, gli YSCs hanno un tempo di vita breve: essi tendono a dissolversi nel disco galattico in $\mathcal{O}(10^2)$ Myr, rilasciando il loro contenuto di DCOBs nel disco. Questo implica che le stime sulla popolazione di DCOBs nel disco galattico devono tenere conto della popolazione di DCOBs negli YSCs. Allo scopo di studiare la popolazione di DCOBs negli YSCs, ho effettuato e analizzato $\gtrsim 10^3$ simulazioni dirette a N-corpi di YSCs accoppiate ad un programma di evoluzione stellare, Le simulazioni sono state prodotte con l'ambiente software STARLAB (Portegies Zwart et al., 2001), modificato per includere algoritmi aggiornati di evoluzione stellare in funzione della metallicità (Mapelli and Bressan, 2013). Questi algoritmi comprendono venti stellari in funzione della metallicità e la possibilità che una stella massiva collassi direttamente in un buco nero (BH), senza esplosione di supernova (SN). Questo processo di formazione dei BH, chiamato "collasso diretto" o "SN fallita", permette la formazione di BHs più massivi. In aggiunta, ho sviluppato SLTOOLS, una suite di programmi che facilitano la produzione e gestione delle simulazioni. Questi provvedono strumenti per automatizzare la maggior parte dei passaggi necessari per ottenere dati puliti e pronti per essere analizzati, inclusi un controllo della qualità automatico e la gestione degli errori. Nella mia analisi ho seguito la vita delle binarie di oggetti compatti e ho investigato l'impatto delle interazioni dinamiche, della metallicità e delle proprietà strutturali degli YSCs ospiti sulla popolazione di BMCs. Mi sono focalizzato su quanti DCOBs vengono prodotti in media per YSCs (~ 4 binarie BH-BH stabili, ~ 1 binarie BH-BH instabili, ~ 0.1 NS-NS e ~ 0.1 BH-NS per YSC durante tutta la simulazione) e su come questa quantità cambia nel tempo: se considero solo le binarie BH-BH stabili, trovo che il loro numero cresce monotonicamente nel tempo da 0 a ~ 0.4, mentre le binarie BH-BH instabili mostrano un picco dopo il collasso del core e poi una decrescita fino a ~ 0.05.

Ho trovato che $\gtrsim 90\%$ delle binarie BH-BH si formano da scambi. I risultati

indicano che i BHs sono estremamente efficienti nell'acquisire compagni attraverso scambi dinamici. Inoltre, una metallicità bassa, grazie al fatto che i BH possono averemasse maggiori, favorisce la formazione di binarie BH-BH massicce e stabili in tempi più brevi. Ho anche trovato che le binarie NS-NS sono, almeno, dieci volte meno numerose delle binarie BH-BH, nonostante la funzione di massa iniziale. La mia analisi ha mostrato che la formazione di BH-BH è anche favorita da alta densità ($\sim 3 \times 10^3\,\mathrm{M_\odot pc^{-3}}$) e alta concentrazione (potenziale centrale adimensionale $W_0 \gtrsim 3$), mentre non è molto sensibile alla frazione di binarie primordiali. Vale comunque la pena notare che solo il 23% dei BMCs tra le binarie BH-BH viene da scambi, mentre il resto è costituito da binarie primordiali. D'altra parte, gli incontri dinamici sono importanti anche per le binarie primordiali, in quanti sono responsabili per la diminuzione del semiasse maggiore a della binarie BH-BH (SMA). Le binarie BH-BH sono in grado di raggiungere valori dello SMA sufficientemente bassi che l'evoluzione della binaria è dominata dall'emissione di GWs. Senza la dinamica, questo processo avrebbe impiegato un tempo molto maggiore. Ho trovato che solo 6% dei BMCs NS-NS si sono formati attraverso scambi. Il fatto che la maggior parte delle binarie NS-NS sia primordiale è consistente con le nostre aspettative percheé è poco probabile che una NS acquisisca una compagna NS se le interazioni dinamiche sono dominate dai BHs. Per questa ragione è interessante che io abbia trovato alcune binarie NS-NS (6%) formate attraverso scambi.

Ho anche analizzato le proprietà dei DCOBs: masse, masse chirp ($m_{\rm chirp} = \frac{(m_1 m_2)^{3/5}}{(m_1+m_2)^{1/5}}$, dove m_1 e m_2 sono le masse dei due membri della binaria), SMAs e eccentricità. Nelle mie simulazioni i BHs sono più massivi a metallicità minori (massa massima di un BH $\sim 80\,\mathrm{M_\odot}$ a $Z = 0.01\,\mathrm{Z_\odot}$) grazie agli algoritmi di evoluzione stellare e di collasso diretto adottati. In aggiunta, BHs ancora più massivi si possono formare grazie a coalescenza con compagni stellari. Di conseguenza, la massa massima che trovo per i BH è $\sim 125\,\mathrm{M_\odot}$. Questo andamento si riflette nelle masse chirp, che raggiungono valori di $\sim 80\,\mathrm{M_\odot}$. Tuttavia, la massa chirp per una binaria BMC è più bassa ($\sim 40\,\mathrm{M_\odot}$) e il resto

delle masse dei BMCs sono inferiori a $20\,M_{\odot}$.

La distribuzione dei SMA mostra che, sebbene le binarie NS-NS siano molto meno numerose delle binarie BH-BH, i loro SMA sono molto minori (SMA minimo per le binarie NS-NS $a_{\mathrm{min,NS-NS}} \sim 10^{-3}\,\mathrm{AU}$ in confronto a $a_{\mathrm{min,BH-BH}} \sim 10^{-1}\,\mathrm{AU}$). Questo è un effetto di selezione: le binarie NS-NS che trovo provengono da binarie sufficientemente strette da sopravvivere a due esplosioni di SN e agli incontri dinamici.

Questo risultato si ritrova nei tempi scala di coalescenza (tempo necessario perché una binaria coalesca solo per effetto dell'emissione di GWs, $t_{\mathrm{GW}} \propto a^4(1-e^2)^{7/2}/m_1 m_2 m_{\mathrm{tot}}$, dove G è la costante gravitazionale, m_1 e m_2 sono le masse dei due membri della binaria, a è il semiasse maggiore e e è l'eccentricità): le binarie NS-NS hanno tempi scala più corti ($t_{\mathrm{GW,min,NS-NS}} \sim 10^{-5}\,\mathrm{Gyr}$ in confronto a $t_{\mathrm{GW,min,BH-BH}} \sim 10^{-1}\,\mathrm{Gyr}$ per i BH-BH). Infatti, trovo che il 76% delle binarie NS-NS coalesce durante le simulazioni (36% di tutte le binarie NS-NS), mentre nessuna delle binarie BH-BH coalesce.

Mentre non esistono evidenze osservative delle binarie BH-BH, nella nostra galassia sono state osservate 10 binarie NS-NS (Lorimer, 2008).

Ho confrontato le proprietà delle binarie NS-NS osservate (periodo, eccentricità e tempo scala di coalescenza) con quelle delle binarie NS-NS nelle mie simulazioni e ho trovato un accordo molto buono. Le uniche differenze si possono trovare ai periodi più corti e più lunghi. Queste differenze sono dovute a effetti di selezione: per periodi molto corti ($\lesssim 2$ hours) le binarie NS-NS coalescono in tempi molto brevi ed è difficile osservarle in questo stato. Periodi molto lunghi ($\gtrsim 10^3$ days) sono troppo lunghi per essere osservati fino ad ora.

Infine, ho derivato il tasso di coalescenza atteso nelle mie simulazioni e ho investigato se questo tasso dipende dalle proprietà dello YSC (massa, densità, concentrazione, frazione di binarie primordiali e metallicità). Non ho trovato alcuna dipendenza significativa del rate di coalescenza delle binarie BH-BH dalle proprietà strutturali degli YSCs all'interno dei valori considerati. Le incertezze, comunque, sono abbastanza grandi.

Il tasso di coalescenza globale per le binarie BH-BH derivato dalle mie sim-

ulazioni è $R_{\mathrm{merger,BH-BH}} = 0.0019 \pm 0.0007\,\mathrm{Mpc^{-3}Myr^{-1}}$. Il tasso di detezioni mostra una dipendenza (sebbene non molto significativa, a causa delle incertezze) dalla densità e dalla concentrazione dello YSC ospite: il tasso di detezioni è più alto tanto più l'ammasso è denso e concentrato, in accordo con quanto trovato per il numero medio di binarie BH-BH prodotto durante la vita dell'ammasso. Inoltre, il tasso di detezioni per le binarie BH-BH anticorrela con la frazione di binarie primordiali. Questo risultato necessita di maggiori approfondimenti.

Il tasso globale di osservazione per le binarie BH-BH è
$R_{\mathrm{detection,BH-BH}} = 0.8 \pm 0.2\,\mathrm{yr^{-1}}$.

I tassi di coalescenza e osservazioni attesi per le binarie NS-NS and BH-NS sono $R_{\mathrm{merger,NS-NS}} = 0.258 \pm 0.005\ \mathrm{Mpc^{-3}Myr^{-1}}$, $R_{\mathrm{merger,BH-NS}} = 0.0009 \pm 0.0002\ \mathrm{Mpc^{-3}Myr^{-1}}$, $R_{\mathrm{detection,NS-NS}} = 0.65 \pm 0.01\ \mathrm{yr^{-1}}$, $R_{\mathrm{detection,BH-NS}} = 0.0107 \pm 0.0006\ \mathrm{yr^{-1}}$ per binarie NS-NS e BH-NS, rispettivamente.

I tassi di coalescenza e osservazione di binarie BH-BH e NS-NS sono consistenti con le previsioni pessimistiche fornite dalla collaborazione Virgo/LIGO (Abadie et al., 2010). I tassi di coalescenza e osservazione di binarie BH-NS sono minori della previsione più pessimistica in letteratura dal momento che la formazine di binarie BH-NS è sfavorita dai processi dinamici che favoriscono la produzione di binarie BH-BH a discapito delle binarie BH-NS.

MOTIVATION

Gravitational waves (GWs) are among the "most wanted" predictions of General Relativity: while indirect confirmations of GWs came from observations of pulsar binaries, a direct detection of GWs is still missing. The most promising effort to achieve a direct observation of GWs is a network of ground based GWs detector made of Michelson's interferometers. The second-generation of such detectors, Advanced Virgo and LIGO, will start operating within 2016, prompting the expectations of the astrophysics community. In order to meet the challenge of the first direct GW detection, it is very important to improve our knowledge of the possible sources of GWs, and to make predictions on their demographics. Mergers of double compact-object binaries (DCOBs), i.e. black hole-black hole (BH-BH), neutron star-neutron star (NS-NS) and neutron star-black hole (NS-BH) binaries, are among the most promising sources of GWs in the frequency range that will be explored by Advanced Virgo and LIGO (~10-10000 Hz). Moreover, since no electromagnetic emission is expected from BH-BH binaries, their presence might be revealed either from peculiar dynamical effects (e.g. perturbations on the signal of a pulsar that is gravitationally bound to a BH-BH binary), or from GW emission. Currently, no stellar BH-BH binaries have ever been observed. Thus, theoretical models and simulations are the only way to investigate the demographics of such binaries, before the first GW detection.

The purpose of my PhD project is to study DCOBs in YSCs as possible sources of detectable gravitational waves, improving our knowledge of their demographics and properties. I will derive accurate predictions for Advanced Virgo

and LIGO.

In Chapter 1 I will introduce the topic of gravitational waves. In Chapter 2 I will review the main dynamical processes and properties of star clusters and I will discuss how we can simulate star clusters. Chapter 3 discusses the properties and the evolution of BH-BH, NS-NS, BH-NS binaries that form in intermediate mass ($\sim 3000-4000\,M_{\odot}$) young ($< 100\,$Myr) star cluster, according to the results published in Ziosi et al. (2014). Chapter 4 discusses the influence of the structural properties of the host star cluster (density, concentration, metallicity, mass, primordial binary fraction) on the formation and evolution of BH-BH, NS-NS, BH-NS binaries. In Chapter 5 I describe the new routines for the host galaxy tidal field that I implemented in STARLAB. This will allow me to account for the importance of the external tidal field on the evolution of DCOBs. Chapter 6 is dedicated to the conclusions.

CHAPTER 1

GRAVITATIONAL WAVES

Gravitational waves (GWs) are perturbations in the spacetime that propagates at the speed of light. They deform the spacetime during their passage. Fig. 1.1 shows how the two polarization modes of a GW stretch and compress a ring of test masses as a function of the wave phase. GWs were predicted by Einstein's general relativity (GR) but have never been observed directly. The main reason is that the effect caused by the passage of a GW is very small. The required sensitivity is very high and the technological effort matched the requirements only recently. In my thesis I focus on GWs emitted by double compact object binaries (DCOBs), i.e. binaries composed of two stellar compact objects such as black holes (BHs) or neutron stars (NSs). White dwarfs (WDs) are not taken into account because the signal they emit is two weak to be detected in the near future and with the available detectors. In particular I will focus on the three ground based GW detectors part of the Virgo/LIGO consortium.

In Section 1.1 I will briefly present the basic formalism needed to deal with GWs. In Section 1.2 I will derive some results about GWs emitted by DCOBs. Section 1.3 is devoted to the GW sources and in Section 1.4 I will present some

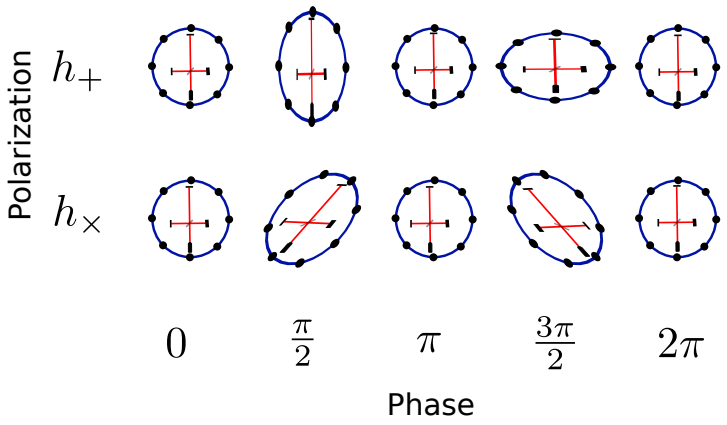

Figure 1.1: Effect of the passage of a GW on a ring of test masses. The deformation is shown for the two polarization modes as a function of the phase of the wave.

of the GW detectors interesting for my research.

1.1 Gravitational wave formalism

There are two ways of studying GWs. The first is to perturb the metric and follow that perturbation, the other implies solving the Einstein's equations exactly to describe both the source and the wave. No exact solution has ever been found for the general case, although it is possible to find a solution by imposing some symmetries. Both the approaches result in GR calculations I will avoid here. Instead, I will provide the most intuitive approximations and the most important results for GW astrophysics, leaving the details to GR textbooks.
Let us consider a small perturbation of the flat Cartesian metric:

$$g_{\alpha\beta}(\mathbf{x}) = \eta_{\alpha\beta} + h_{\alpha\beta}(\mathbf{x}) \tag{1.1}$$

with $\eta_{\alpha\beta}$ the Minkowsky metric. Let us consider the Einstein equation

$$R_{\alpha\beta} - \frac{1}{2} g_{\alpha\beta} R = \frac{8\pi G}{c^4} T_{\alpha\beta} \tag{1.2}$$

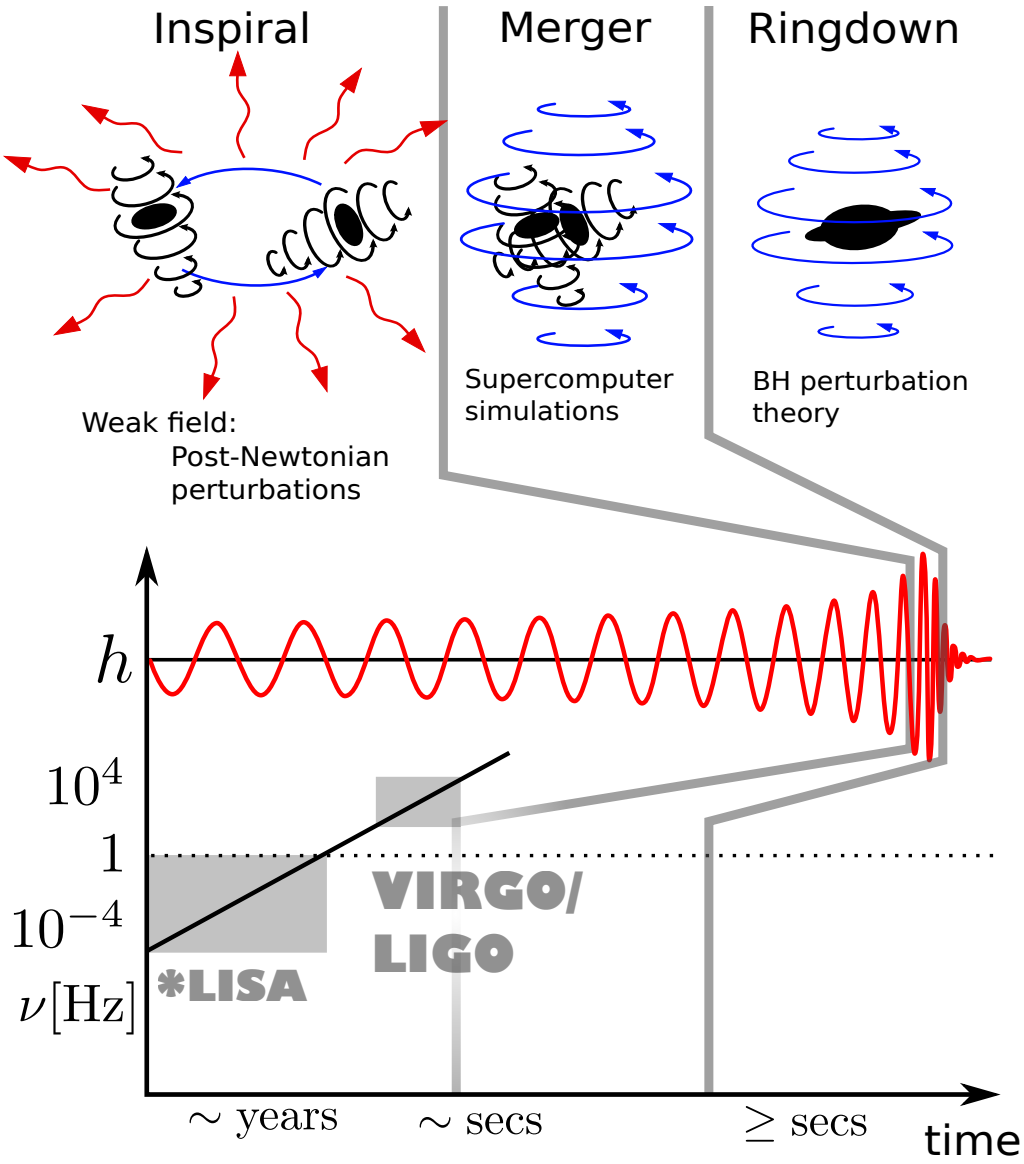

Figure 1.2: **Upper part:** representation of the three phases of a DCOB merger: inspiral, when the two members of the binary are orbiting one around each other, merger, when they coalesce, and ring-down, when the new-born single object settles down. Annotations show the most used methods to study the three different phases of a DCOB merger. **Lower part:** schematic representation of the strain of the GWs emitted by the three phases of a DCOB merger coupled with the associated frequency of the wave and the range in frequency observable by different GW detectors.

where $R_{\alpha\beta}$ is the Ricci tensor, R is the scalar curvature and $T_{\alpha\beta}$ is the stress-energy tensor.

For the metric (1.1) and in vacuum ($T_{\alpha\beta} = 0$) the (1.2) becomes simply

$$\partial_\beta h^\beta_\alpha(\mathbf{x}) - \frac{1}{2}\partial_\alpha h^\beta_\beta(\mathbf{x}) = 0 \tag{1.3}$$

Equation (1.3) can be rewritten using the D'Alambert operator as

$$\Box h_{\alpha\beta}(\mathbf{x}) = 0 \tag{1.4}$$

In this equation we can recognize the functional form of the *wave equation*. The simplest solution has form

$$h_{\alpha\beta}(\mathbf{x}) = \begin{pmatrix} h_+ & h_\times \\ h_\times & -h_+ \end{pmatrix} e^{i(kz-\omega t)} \tag{1.5}$$

which represents a polarized wave which propagate along the z-axis, with frequency ω. and constant amplitudes $h_+, h_\times$ for the two polarizations.

We can now remove the assumption to be in vacuum because we need a mass density to be the source of the wave. It can be shown that 1.4 becomes

$$\Box h_{\alpha\beta}(\mathbf{x}) = -\frac{16\pi G}{c^4} T_{\alpha\beta} \tag{1.6}$$

With some simplifying assumptions, equation (1.6) can be integrated and gives (if the source is a distribution of masses at rest, at a distance r from the observer)

$$h^{ij}(t,\mathbf{x}) \sim \frac{2G}{rc^4}\frac{\mathrm{d}^2}{\mathrm{d}t^2}\left[I^{ij}(t-r/c)\right] \tag{1.7}$$

where $t-r/c$ is the delayed time and I^{ij} is the second mass moment or moment of inertia, that is the quadrupole moment of the mass, $I^{ij} \equiv \int \mathrm{d}^3x\rho(t,\mathbf{x})x^i x^j$. This result is very important. It shows that the first term in a mass distribution contributing to the emission of GWs is the quadrupole.

1.2 Gravitational waves from binaries

1.2.1 Strain

It can be shown that given $h^{ij}(t,\mathbf{x})$ in equation (1.6), for a gravitational wave emitted by a compact object binary during the inspiral, the two polarization modes of the relative deformation can be written as

$$h_+(t,\theta,\phi,r) = \frac{1}{r}\frac{4G\mu\omega_{\rm orb}^2 a^2}{c^4}\frac{1+\cos^2\theta}{2}\cos\left(2\omega_{\rm orb}\,t_{\rm ret}+\phi\right) \tag{1.8}$$

$$h_\times(t,\theta,\phi,r) = \frac{1}{r}\frac{4G\mu\omega_{\rm orb}^2 a^2}{c^4}\cos\theta\sin\left(2\omega_{\rm orb}\,t_{\rm ret}+\phi\right) \tag{1.9}$$

in spherical coordinates (r,ϕ,θ). $\mu \equiv \frac{m_1 m_2}{m_1+m_2}$ is the reduced mass of the binary, a is semi-major axis, $\omega_{\rm orb}$ is the orbital angular frequency and $e = 0$ is the eccentricity. $t_{\rm ret} = t - r/c$ is the retarded time and the orbital angular velocity is given by $\omega_{\rm orb}^2 = \frac{GM}{a^3} \equiv \frac{G(m_1+m_2)}{a^3}$.
As only the frequency term of $h_+(t,\theta,\phi,r)$ and $h_\times(t,\theta,\phi,r)$ is $2\omega_{\rm orb}$, frequency of the GW is

$$\omega_{\rm GW} = 2\omega_{\rm orb} \tag{1.10}$$

From the expressions of the two wave polarizations, we can derive the relative deformation induced in the spacetime by the passage of a GW. This relative deformation is called strain. The final form of the strain of the GW is

$$\sqrt{h_+^2 + h_\times^2} = 4\frac{G\mu\omega_{\rm orb}^2 a^2}{c^4}\frac{1}{r}\sqrt{\frac{(1+\cos^2\theta)^2}{4}+\cos^2\theta} \tag{1.11}$$

If the binary is observed edge-on, $\theta = \frac{\pi}{2}$ and averaging over all the angles, the strain becomes

$$h = \frac{4G}{c^4}\frac{\mu\omega_{\rm orb}^2 a^2}{r} \tag{1.12}$$

Substituting the semi-major axis or the angular frequency from Kepler equations we can rewrite the strain as

$$h = \frac{4G^2}{c^4}\frac{m_1 m_2}{ar} \tag{1.13}$$

$$= \frac{4G^{5/3}}{c^4}\frac{m_1 m_2}{(m_1+m_2)^{1/3}}\omega_{\rm orb}^{2/3} = \frac{4G^{5/3}}{c^4} m_{\rm chirp}^{5/3}\omega_{\rm orb}^{2/3} \tag{1.14}$$

where

$$m_{\rm chirp} \equiv \left(\frac{m_1 m_2}{m_1+m_2}\right)^{3/5}(m_1+m_2)^{2/5} = \frac{(m_1 m_2)^{3/5}}{(m_1+m_2)^{1/5}} \tag{1.15}$$

is the chirp mass, a useful combination of the masses on which both the frequency and the strain of GWs emitted during the inspiral of a DCOB depend. A useful approximation in this regime is given by

$$h \sim 10^{-21}\left(\frac{m_{\rm chirp}}{\mathrm{M}_\odot}\right)^{5/3}\left(\frac{P_{\rm b}}{\rm hours}\right)^{-2/3}\left(\frac{r}{\rm kpc}\right)^{-1} \tag{1.16}$$

At the last stable orbit, LSO (also called innermost stable circular orbit, ISCO), where

$$a_{\rm ISCO} = 3R_{\rm s} = 3\frac{2G(m_1+m_2)}{c^2} \sim 1.19\times10^{-6}\left(\frac{m_1+m_2}{20\,\mathrm{M}_\odot}\right)\mathrm{AU} \tag{1.17}$$

(where $R_{\rm s}$ is the Schwarzschild radius) the angular frequency becomes

$$\omega_{\rm orb;ISCO} = \frac{2c^3}{6^{2/3}G}\frac{1}{m_1+m_2} \sim 6129.7\left(\frac{m_1+m_2}{20\,\mathrm{M}_\odot}\right)^{-1}\mathrm{rad/s} \tag{1.18}$$

that is

$$f_{\rm GW} \sim 975.6\left(\frac{m_1+m_2}{20\,\mathrm{M}_\odot}\right)\mathrm{Hz} \tag{1.19}$$

The strain can be written as

$$h_{\rm ISCO} = \frac{G}{c^2}\frac{1}{r}\frac{m_1 m_2}{m_1+m_2} \sim 2.47\times10^{-19}\frac{10^6\,\mathrm{pc}}{r}\frac{m_1 m_2}{m_1+m_2}5\,\mathrm{M}_\odot \tag{1.20}$$

These can be considered as the maximum frequency and strain achieved during the inspiral phase, immediately before the merger.

1.2.2 Energy loss by a binary radiating GWs

Binary hardening and coalescence timescale

It can be shown that the quadrupole moment of a mass radiates a power

$$P = \frac{32}{5}\frac{G^4}{c^5}\frac{1}{a^5}(m_1 m_2)^2(m_1+m_2) \tag{1.21}$$

The energy radiated is lost by the binary, thus we can write the power also as

$$\begin{aligned} P &= -\frac{\mathrm{d}E_{\mathrm{orb}}}{\mathrm{d}t} = -\frac{\mathrm{d}}{\mathrm{d}t}\left(\frac{Gm_1m_2}{2a}\right) \\ &\text{(if } m_1, m_2 = const\text{)} \\ &= -\frac{Gm_1m_2}{2}\frac{\mathrm{d}}{\mathrm{d}t}\left(\frac{1}{a}\right) = \frac{Gm_1m_2}{2}a^{-2}\frac{\mathrm{d}a}{\mathrm{d}t} \end{aligned} \tag{1.22}$$

Combining (1.21) and (1.22) we find

$$\begin{aligned} \frac{Gm_1m_2}{2}a^{-2}\frac{\mathrm{d}a}{\mathrm{d}t} &= \frac{32}{5}\frac{G^4}{c^5}a^{-5}(m_1m_2)^2(m_1+m_2) \\ \frac{\mathrm{d}a}{\mathrm{d}t} &= \frac{64}{5}\frac{G^3}{c^5}a^{-3}(m_1m_2)(m_1+m_2) \\ \int \mathrm{d}t &= \left[\frac{64}{5}\frac{G^3}{c^5}(m_1m_2)(m_1+m_2)\right]^{-1}\int a^3\,\mathrm{d}a \end{aligned}$$

Integrating from the initial semi-major axis to zero, when the binary can be considered merged, we find the time a binary needs in order to merge only because of GW emission. It is called coalescence timescale, or Peter's timescale:

$$t_{\mathrm{GW}} = \frac{5}{256}\frac{c^5}{G^3}\frac{a^4}{(m_1m_2)(m_1+m_2)} \tag{1.23}$$

This approximation holds only if the binary has a circular orbit.

Non circular orbits: Peters equations

If eccentricity is not zero, calculations become much more complicated. A good approximation is given by Peters (1964) and Peters and Mathews (1963).

Binaries can harden transferring energy during a three body encounter but also emitting GWs. Given the equation of the relative orbit

$$r = \frac{a(1-e^2)}{1+\cos\psi} \tag{1.24}$$

and the expression of semi-major axis and angular momentum:

$$a = -\frac{Gm_1m_2}{2E} \tag{1.25}$$

$$L^2 = \frac{Gm_1^2m_2^2}{m_1+m_2}a(1-e^2) \tag{1.26}$$

where L is the angular momentum, the time average of the energy (Peters and Mathews, 1963) and the average angular momentum (Peters, 1964) emitted by gravitational wave radiation are thus

$$\langle\frac{\mathrm{d}E}{\mathrm{d}t}\rangle = -\frac{32}{5}\frac{G^4m_1^2m_2^2(m_1+m_2)}{c^5a^5(1-e^2)^{7/2}}\left(1+\frac{73}{24}e^2+\frac{37}{96}e^4\right) \tag{1.27}$$

$$\langle\frac{\mathrm{d}L}{\mathrm{d}t}\rangle = -\frac{32}{5}\frac{G^{7/2}m_1^2m_2^2(m_1+m_2)^{1/2}}{c^5a^{7/2}(1-e^2)^2}(1+\frac{7}{8}e^2) \tag{1.28}$$

From equations (1.27) and (1.28) we can derive an equation for the average time variation of the semi-major axis and eccentricity:

$$\langle\frac{\mathrm{d}a}{\mathrm{d}t}\rangle = -\frac{64}{5}\frac{G^3m_1m_2(m_1+m_2)}{c^5a^3(1-e^2)^{7/2}}\left(1+\frac{73}{24}e^2+\frac{37}{96}e^4\right) \tag{1.29}$$

$$\langle\frac{\mathrm{d}e}{\mathrm{d}t}\rangle = -\frac{304}{15}e\frac{G^3m_1m_2(m_1+m_2)^3}{c^5a^4(1-e^2)^{5/2}}\left(1+\frac{121}{304}e^2\right) \tag{1.30}$$

Considering a binary for which the orbit decay includes GW emission as the only energy loss process, the relation between the semi-major axis a and the eccentricity e is

$$\langle\frac{\mathrm{d}a}{\mathrm{d}e}\rangle = \frac{12}{19}\frac{a}{e}\frac{\left[1+\frac{73}{24}e^2+\frac{36}{96}e^4\right]}{(1-e^2)\left[1+\frac{121}{304}e^2\right]} \tag{1.31}$$

These equations are enough to determine the decay, given initial values a_0 and e_0. If $e_0 = 0$, from (1.29):

$$\langle \frac{\mathrm{d}a}{\mathrm{d}t} \rangle = -\frac{64}{5} \frac{G^3 m_1^2 m_2^2 (m_1 + m_2)}{c^5 a^3} \tag{1.32}$$

and integrating from a_0 to a and from $t = 0$ to t we obtain:

$$a(t) = (a_0^4 - 4Ct)^{1/4} \tag{1.33}$$

with $C = \frac{64}{5} \frac{G^3 m_1^2 m_2^2 (m_1+m_2)}{c^5}$.
Thus the system merges in a time

$$t_{\mathrm{mgr}}(e_0 = 0) = \frac{a_0^4}{4C} \tag{1.34}$$

that is the time necessary to go from $a = a_0$ to $a = 0$.
In the case $e_0 \neq 0$, from (1.31)

$$a(e) = \frac{c_0 e^{12/19}}{(1 - e^2)} \left[1 + \frac{121}{304} e^2 \right]^{870/2299} \tag{1.35}$$

with $c_0(a_0, e_0) = a_0 \frac{(1-e_0^2)}{e_0^{12/19}} \left[1 + \frac{121}{304} e_0^2 \right]^{-870/2299}$. This also means that

$$a \frac{e^{12/19}}{(1 - e^2)} \left[1 + \frac{121}{304} e^2 \right]^{870/2299} = const. \tag{1.36}$$

In the limits of $e \to 0$ and $e \to 0$ Eq. (1.31) becomes

$$a(e \sim 0) \sim c_0 e^{12/19} \tag{1.37}$$

$$a(e \sim 1) \sim c_0 \left(\frac{425}{304} \right)^{870/2299} \frac{1}{(1 - e^2)} \sim 1.1352 c_0 \frac{1}{(1 - e^2)}. \tag{1.38}$$

Thus, in most situations, it is possible to consider

$$a(e) \sim \frac{c_0 e^{12/19}}{(1 - e^2)} \tag{1.39}$$

From (1.30) and (1.35) an exact relation can be derived for the decay time in the case of eccentricity not negligible. Combining the two equations we get

$$\begin{aligned}\langle\frac{\mathrm{d}e}{\mathrm{d}t}\rangle &= -\frac{19}{12}\frac{C}{c_0^4}\frac{e^{-29/19}(1-e^2)^{3/2}}{\left[1+\frac{121}{304}e^2\right]^{1181/2299}} \\ &= -\frac{19}{12}\frac{\frac{64}{5}\frac{G^3m_1^2m_2^2(m_1+m_2)}{c^5}}{\left(a_0\frac{(1-e_0^2)}{e_0^{12/19}}\left[1+\frac{121}{304}e_0^2\right]^{-870/2299}\right)^4}\frac{e^{-29/19}(1-e^2)^{3/2}}{\left[1+\frac{121}{304}e^2\right]^{1181/2299}}\end{aligned} \tag{1.40}$$

Thus, the time the system need to merge is given by

$$t_{\mathrm{mgr}} = \frac{12}{19}\frac{c_0^4}{C}\int_0^{e_0}\mathrm{d}e\frac{e^{29/19}\left[1+\frac{121}{304}e^2\right]^{1181/2299}}{(1-e^2)^{3/2}} \tag{1.41}$$

In the limit of $e_0 \sim 0$ and $e_0 \sim 1$ Eq. (1.41) become

$$t_{\mathrm{mgr}}(e\to 0) \sim \frac{12}{19}\frac{c_0^4}{C}\int_0^{e_0} e^{29/19}\,\mathrm{d}e \sim \frac{c_0^4}{4C}e^{48/19} \sim \frac{a_0^4}{4C} \tag{1.42}$$

similar to the $e = 0$ case, and

$$\begin{aligned}t_{\mathrm{mgr}}(e\to 1) &\sim \frac{768}{425}t_{\mathrm{mgr}}(e_0=0)(1-e^2)^{7/2} = \frac{768}{425}\frac{a_0^4}{4C}(1-e^2)^{7/2} \\ &= \frac{768}{425}\frac{5}{256}\frac{c^5}{G^3}\frac{a^4(1-e^2)^{7/2}}{(m_1m_2)(m_1+m_2)} \\ &\sim 1.8\frac{5}{256}\frac{c^5}{G^3}\frac{a^4(1-e^2)^{7/2}}{(m_1m_2)(m_1+m_2)}\end{aligned} \tag{1.43}$$

Often a slightly different version is used in the literature:

$$t_{\mathrm{GW}} = \frac{5}{256}\frac{c^5}{G^3}\frac{a^4(1-e^2)^{7/2}}{(m_1m_2)(m_1+m_2)} \tag{1.44}$$

In the same way, for the semi-major axis shrinking, we find

$$a(t) = \left(a_0^4 - 4C\frac{t}{(1-e^2)^{7/2}}\right)^{1/4} \tag{1.45}$$

Frequency change of GWs

From (1.21), substituting $a = \frac{[G(m_1+m_2)]^{1/3}}{\omega_{\rm orb}^{2/3}}$ and remembering that

$$m_{\rm chirp}^{5/3} = \left[\frac{(m_1 m_2)^{3/5}}{(m_1+m_2)^{1/5}}\right]^{5/3} = \frac{m_1 m_2}{(m_1+m_2)^{1/3}}$$

we obtain

$$P = \frac{32}{5}\frac{c^5}{G}\left(\frac{G m_{\rm chirp}\omega_{\rm GW}}{2c^3}\right)^{10/3} \tag{1.46}$$

Then, from the binary binding energy, with the same substitution, we find

$$E_{\rm orb} = -\frac{G m_1 m_2}{2a} = -\frac{G m_1 m_2}{2}\frac{\omega_{\rm orb}^{2/3}}{[G(m_1+m_2)]^{1/3}} = -\frac{G^{2/3}}{2} m_{\rm chirp}^{5/3}\left(\frac{\omega_{\rm GW}}{2}\right)^{2/3}$$

$$\Rightarrow \frac{{\rm d}E}{{\rm d}t} = -\frac{G^{2/3} m_{\rm chirp}^{5/3}}{2^{5/3}}\frac{2/3}{\omega_{\rm GW}^{1/3}}\frac{{\rm d}\omega_{\rm GW}}{{\rm d}t} \tag{1.47}$$

Equating (1.46) and (1.47) we find

$$\frac{32}{5}\frac{c^5}{G}\left(\frac{G m_{\rm chirp}\omega_{\rm GW}}{2c^3}\right)^{10/3} = -\frac{G^{2/3} m_{\rm chirp}^{5/3}}{2^{5/3}}\frac{2/3}{\omega_{\rm GW}^{1/3}}\frac{{\rm d}\omega_{\rm GW}}{{\rm d}t} \tag{1.48}$$

thus

$$\begin{aligned}\frac{{\rm d}\omega_{\rm GW}}{{\rm d}t}\omega_{\rm GW}^{-11/3} &= -\frac{32}{5}\frac{3}{2}2^{5/3-10/3} G^{-2/3-1+10/3} c^{5-10} m_{\rm chirp}^{10/3-5/3} \\ &= -\frac{16\cdot 3}{5} 2^{-5/3}\frac{G^{5/3}}{c^5} m_{\rm chirp}^{5/3}\end{aligned} \tag{1.49}$$

That is

$$\frac{{\rm d}\omega_{\rm GW}}{{\rm d}t} = \omega_{\rm GW}^{11/3} m_{\rm chirp}^{5/3} \tag{1.50}$$

Integrating

$$
\begin{aligned}
-\int \frac{\mathrm{d}\omega_{\mathrm{GW}}}{\omega_{\mathrm{GW}}^{11/3}} &= \frac{24}{5\cdot 2^{2/3}} \frac{G^{5/3}}{c^5} m_{\mathrm{chirp}}^{5/3} \int \mathrm{d}t \\
\frac{3}{8}\omega_{\mathrm{GW}}^{-8/3} &= \frac{24}{5\cdot 2^{2/3}} \frac{G^{5/3}}{c^5} m_{\mathrm{chirp}}^{5/3} t_{\mathrm{GW}} \\
\omega_{\mathrm{GW}} &= \left(\frac{64}{5\cdot 2^{2/3}}\right)^{-3/8} \frac{G^{-5/8}}{c^{-15/8}} m_{\mathrm{chirp}}^{-5/8} t_{\mathrm{GW}}^{-3/8} \\
&= \left(\frac{64}{5\cdot 2^{2/3}}\right)^{-3/8} \frac{G m_{\mathrm{chirp}}}{c^3}^{-5/8} t_{\mathrm{GW}}^{-3/8}
\end{aligned} \tag{1.51}
$$

Thus, $\omega_{\mathrm{GW}} \propto m_{\mathrm{chirp}}^{-5/8} t_{\mathrm{GW}}^{-3/8}$.

1.3 Gravitational wave sources

Fig. 1.6 shows the frequency spectrum of GWs. The range of frequencies emitted is very broad and there also is a large variety of possible sources. I will not discuss each source in detail here. However, a brief summary of these sources and their associated frequencies can be useful to understand the nature of GWs. At the lower end, at about $f_{\mathrm{GW}} \sim 10^{-16}$Hz, we find the GWs generated by the quantum fluctuations at the beginning of the universe. At these scales the BICEP2 experiment was looking for the marks GWs left on the polarization of the cosmic microwave background. At higher frequencies the characteristic sources are binaries of compact massive objects. Binary supermassive black holes (SMBHs) at the centers of galaxies emit at frequencies $\sim 10^{-9} - 10^{-2}$Hz. At these frequencies the best way to investigate GWs is to look at the perturbation they induce in the periods of the near pulsars. This technique is called Pulsar Timing Array (PTA). We saw in 1.2.1 that $\omega_{\mathrm{GW}} = 2\omega_{\mathrm{orb}}$ and, since the period of a binary is $\propto (m_1 + m_2)^{-1/2}$, GWs emitted at higher frequencies are emitted by less massive binaries. Between 10^{-5} and 10^{-2}Hz the GW sources we encounter are IMRI (intermediate mass ratio inspirals) and EMRI (extreme mass ratio inspirals). These are binaries composed of a supermassive black hole (SMBH) and a less compact massive object, such as a

Figure 1.3: Semi-major axis, eccentricity and coalescence timescale for the simulated best merger candidates in Ziosi et al. (2014).

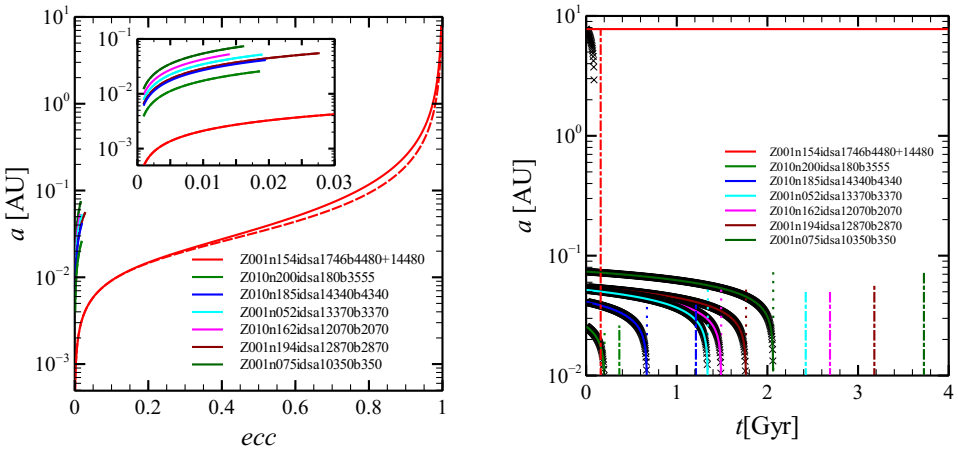

(a) Semi-major axis a as a function of the eccentricity as given by equations (1.35) (solid line) and the approximated version (1.39) (dashed lines). The inset shows a zoom on the binaries with $e \sim 0$ while in the main panel it is possible to see the whole trend for a very eccentric binary ($e \sim 0.997$) with a larger separation. The labels correspond to the identifiers of the simulated systems I will describe in Chapter 3

(b) Semi-major axis evolution as a function of time using the approximations valid for all the eccentricities in Eq. (1.45) (crosses) and that for $e \sim 0$ Eq. (1.33) (solid line). Vertical lines represents the expected merger time from the $e \sim 0$ (dotted lines) and $e \sim 1$ (dash-dotted lines) approximation (Eq. (1.42) and (1.43) respectively).

stellar BH (the mass ratio between the SMBH and the other object is $\gtrsim 10^5$ for an EMRI, and $\gtrsim 10^2$ for an IMRI). At frequencies in the range $10^{-4} - 10^4$Hz the sources are the double compact object binaries (DCOB), binaries composed of two compact stellar object (BH or NS). Rotating NSs and supernova (SN) explosions emit at frequencies between 10 and 10^5Hz. However, in Section 1.1 we saw that to emit GWs it is necessary to have a non-zero quadrupole moment of the mass. In the case of rotating NSs this correspond to deviations from the (almost perfect) spherical shape. For SNs it is necessary that the explosion has some asymmetries.

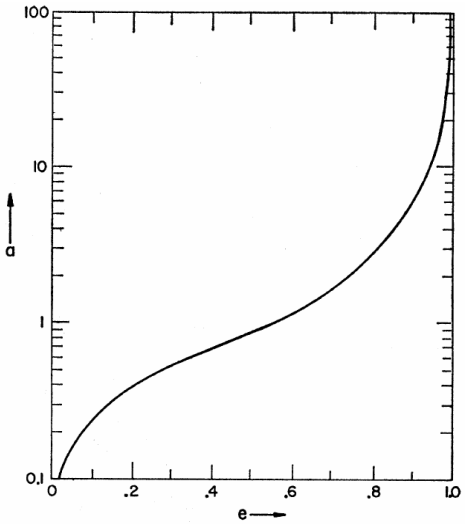

FIG. 1. The semimajor axis a as a function of the eccentricity e in the decay of a two-point mass system. Here, c_0 is chosen to be 1.

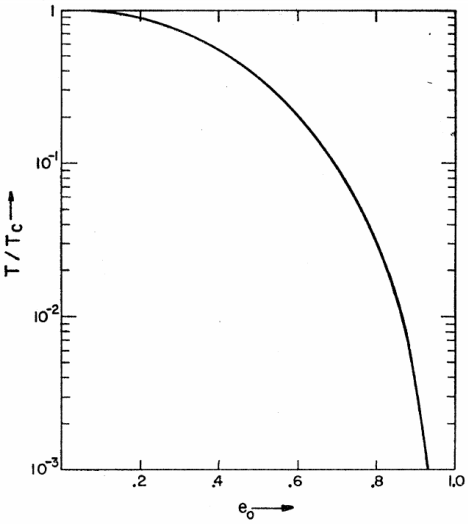

FIG. 2. The ratio of the lifetime of an eccentric system to that of a circular one plotted against the initial eccentricity. This ratio is independent of the initial value of the semimajor axis.

Figure 1.4: Original illustrations from Peters (1964) paper showing the relations between the semi-major axis and the eccentricity and between the lifetime of a system over the lifetime of a circular one as a function of the eccentricity.

In my thesis, I investigate DCOBs. Double compact object binaries (DCOBs), such as BH-BH or NS-NS binaries, are expected to be powerful sources of detectable GWs. DCOB members, at the end of their life, are close enough to lose a considerable amount of energy because of GW emission.

Every (bound) system of two masses emits GWs throughout its whole life. However, as I showed in Section 1.2.1, the strain of a GW emitted by a binary is $\propto \frac{G^2 m_1 m_2}{c^4 ar}$ and it is very small. Thus, GWs are able to remove enough energy to considerably modify the orbit of the binary and to have a strain higher than the detectors sensitivity only for those binaries with a combination of very high masses and very small semi-major axis. Fig. 1.5 shows the order of magnitude of the strain associated to a GW emitted by a binary as a function of the masses of the components (equals, for simplicity) and semi-major axis. For example, let us consider a binary composed of two stars, both with mass $10M_\odot$, placed at 1 Mpc from us. To be able to emit a strain of 10^{-21}, the minimum strain we will be able to detect, the semi-major axis of the system should be $\sim 2\times10^{-4}$AU $\sim 4\times10^{-2}R_\odot$. A binary composed of two Sun-like stars, should have a semi-major axis of $\sim 2\times10^{-6}$AU $\sim 4\times10^{-4}R_\odot$ Such binaries do not exist because they would have merger much earlier emitting undetectable GWs. For this reason, only binaries composed of two compact objects have a chance to be detected by the current GW detectors.

The three main phases during which DCOBs emit GWs are the inspiral, the merger and the ring-down (see Fig. 1.2). During the inspiral the two members of the binary are close enough to lose enough energy by GW radiation to cause a non-negligible shrink of the orbit but they are still orbiting one around each other. The merger is the moment in which the two members of the binary come in contact and become a single object, that, in the subsequent moments, settle down during the ring-down.

During the inspiral, the frequency emitted is twice the orbital frequency of the binary.

DCOBs containing a NS, NS-NS and BH-NS binaries, are very interesting because there is the possibility to observe their electromagnetic counterpart.

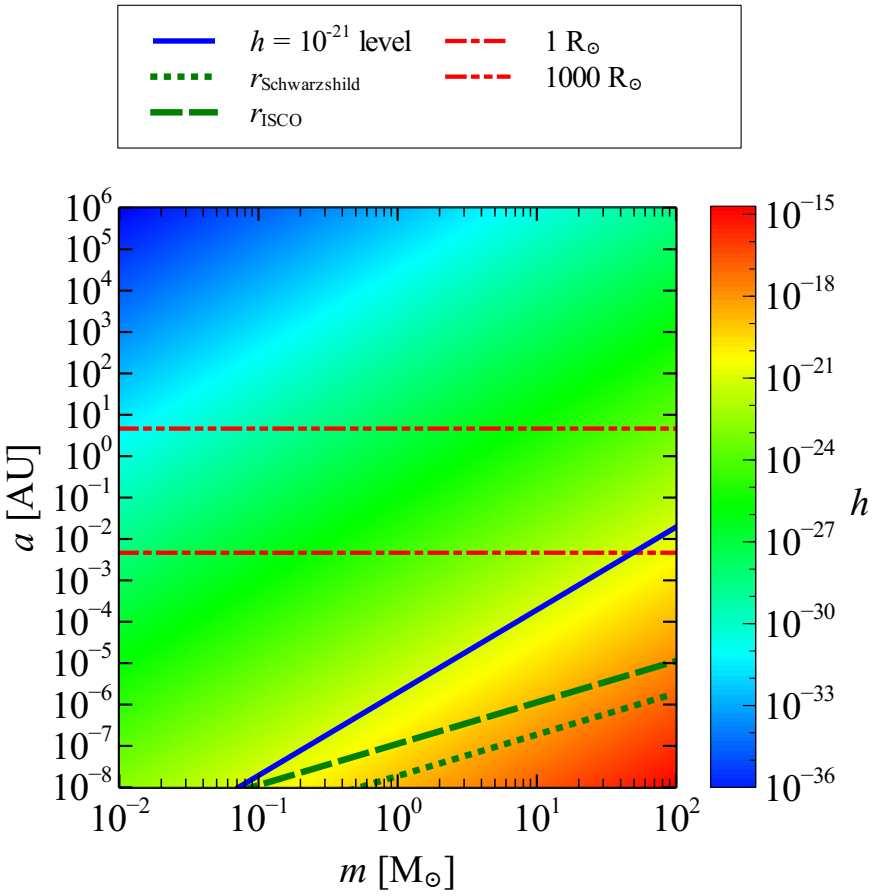

Figure 1.5: Strain of a GW emitted by a binary of two equal mass stars placed at 1 Mpc as a function of the masses of the stars and the semi-major axis of the binary. The solid blue line shows the contour at 10^{-21}, that is the Virgo/LIGO sensitivity. The green dashed line shows the last stable orbit of a binary as a function of the masses of the binary, the green dotted line shows the Schwarzschild radius as a function of the mass. The two red horizontal lines show $1\,R_\odot$ and $10^3\,R_\odot$.

Such counterpart might be a short gamma-ray burst or a kilonova (e.g. Clark et al. (2014)). Furthermore, while BH-BH and BH-NS binaries have never been observed directly, 10 NS-NS binaries have been detected in our Galaxy. The detection of a NS-NS binary is possible if one of the members of the binary is a pulsar. Pulsars are highly magnetized, rotating NS that emit a beam of electromagnetic radiation.
If during the NS rotation the beam is pointing to Earth, it is possible to observe the emitted radiation as a radio pulse in the sky. The periods of the observed pulsars span from $\sim 10^{-3}$ to ~ 10 seconds and are extremely stable. They are so stable they can be used as reference clocks by astronomers. In 1974 Joseph Hooton Taylor, Jr. and Russell Hulse discovered a pulsar (Hulse and Taylor, 1975) with a time shift of $\sim 80\mu$s a day, while known secular changes of the period are of the order of 10μs. They found that the period shift was due to the fact that the pulsar was member of a binary with another compact object.
The residual period change, $\dot{P}_{\rm b} \sim 2 \times 10^{-12}$ s Hz, was the effect of GW emission. As it can be seen from Fig. 1.8, the agreement with GR expectations is almost perfect.
Since 1974 few other systems were observed. Fig. 1.8 shows the orbital properties (period and eccentricity) of such NS-NS systems. Among the others, J0737-3039 is of great interest being the first double pulsar observed (Burgay et al., 2003).

1.4 Detecting gravitational waves

Different techniques are adopted in the attempt to directly detect a gravitational wave.

1.4.1 Pulsar Timing Array

PTA (Pulsar Timing Array) makes use of an excellent detector provided by nature. The idea behind PTA is that, even if pulsars are so precise clocks that pulse Time of Arrivals (TOAs) can be predicted at the μs scale, sometimes the

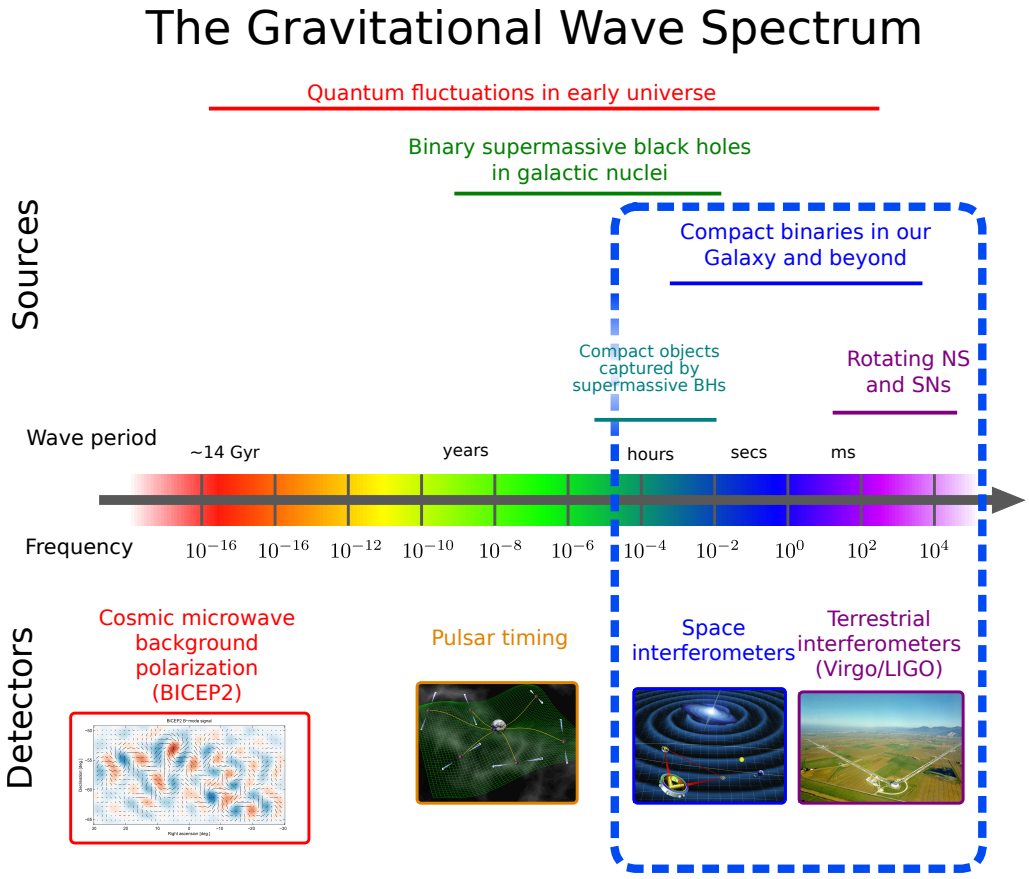

Figure 1.6: Schematic representation of the frequency spectrum of GWs together with the sources expected to emit at each different frequency range and the detectors able to observe at different frequencies. The rainbow colors associated to the frequency scale are only a graphic representation and are not related to the electromagnetic spectrum. The blue dashed rectangle highlights the frequency region in which Virgo/LIGO are able to detect GWs. Inspired by a NASA cartoon.

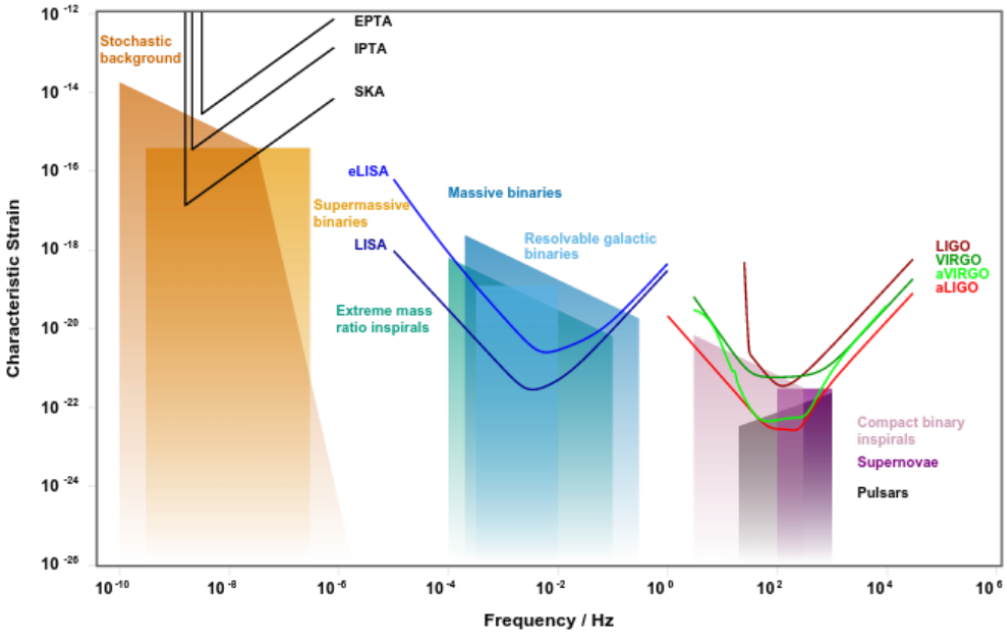

Figure 1.7: Scheme of the characteristic strain of the signal of different GW sources together with the sensitivity curves of most of the GW detectors. From `rhcole.com/apps/GWplotter`.

observed TOAs shows deviations form the predicted ones. Thus, the model and the analysis are missing some physical effect that took part in the pulse emission, propagation and detection. GWs are thought to be the missing part of the model (Hobbs, 2011). The consequence is that, looking at the residuals between the expected and observed TOAs, it would be possible to have a sign of the passage of a GW. Because of the uncertainties about the origin of a residual (e.g. errors in the terrestrial time standards or in the planetary ephemeris, or irregular spin-down of the pulsar), it is necessary to look at the correlation in the timing residuals between pairs of pulsars in a network of 20-50 known pulsars (Hobbs, 2011).

PTA is sensitive in the ultra-low frequency range, at about 10^{-9} to 10^{-8}Hz (see also Fig. 1.6 and 1.7), because pulsars are typically observed only once every few weeks, the observations span years and the data require to be fitted to a

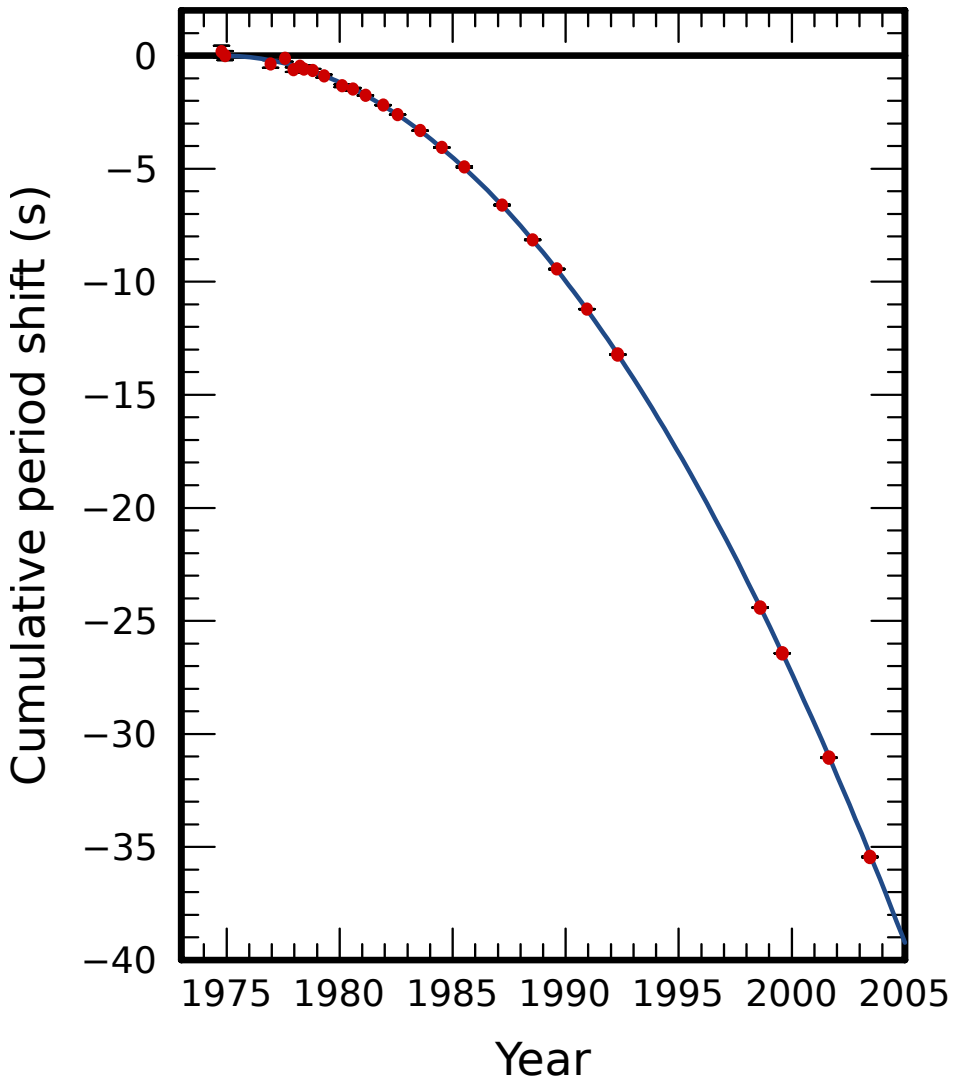

Figure 1.8: Red dots show the cumulative period change of the Hulse-Taylor pulsar over a period of 30 years. The blue line is the GR theoretical prediction.

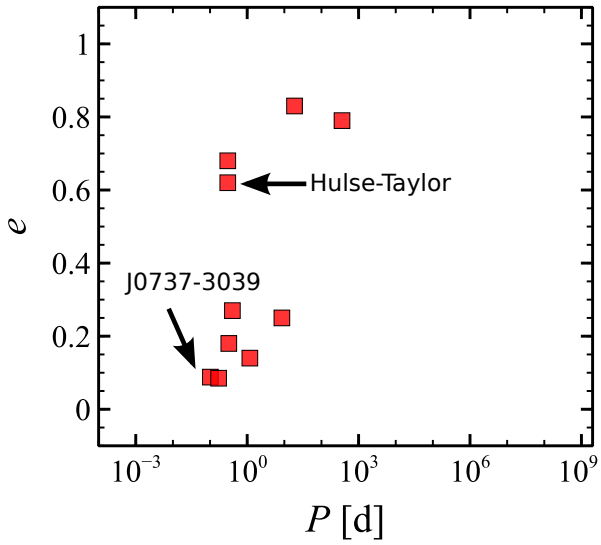

Figure 1.9: Period (in days) and eccentricity of few NS-NS systems containing at least one pulsar observed since 1974. From Lorimer, 2008.

pulsar timing model.

The sources observable by using PTA should emit at the right frequencies and be strong enough to be detected. They can be divided among periodic sources, bursts and background. SMBH binaries are perfect candidates as periodic sources detectable by PTA; however, none has been found yet. Sources of bursts are the formation of a SMBH and SMBH binaries with high eccentricity. The stochastic background can be generated by the early phases of a SMBH binary coalescence or by the relic GWs from the first phases of the universe. Fig. 1.7 shows the strain of these sources.

All PTA experiments so far resulted in a non-detection and set an upper limit on the rate of events which could have been detected (Zhu et al., 2014; Wang et al., 2015).

1.4.2 Resonant-mass detectors

This kind of detector was the first proper man-built GW detector. Resonant-mass detectors are heavy (metal) masses with regular shapes, cylinders or spheres, isolated from vibrations. The idea is that a GW, while passing, would excite the resonant vibration modes of the mass or deform it. These vibrations or deformations, caught by the sensors and amplified would give the signal.

The MiniGRAIL detector, at the University of Leiden, for example, is a sphere of 1300 kg of a copper-aluminum alloy. The peak strain sensitivity is $\sim 10^{-20}\mathrm{Hz}^{-1/2}$ at $\sim 3000 \pm 30$ Hz (Weber, 1968).

1.4.3 Interferometers

Virgo and the two LIGO detectors are three huge Michelson laser interferometers. They are built to be able to detect GWs with frequencies in the range emitted by DCOBs at the end of the inspiral, just before the merger, between 10 and 10^4 Hz. Moreover, the spacetime deformation should exceed the minimum deformation detectable by such detectors. LIGO (Laser Interferometer Gravitational-Wave Observatory) started the observations in 2002 and was stopped in 2010, while Virgo started in 2007. The initial strain sensitivity was $\mathcal{O}(10^{-21})$. The three detectors are now being upgraded to gain one order of magnitude in sensitivity, reaching slightly more than 10^{-22}. Their enhanced configurations, called Advanced Virgo and Advanced LIGO (aVirgo/aLIGO), are expected to start observing in 2016-2017.

Each arm of the detectors is a 3-4 km Fabry-Perot cavity. The Virgo interferometer, described in Aasi et al. (2012), is built to look at the dark fringes resulting from the interference of the laser coming from the two arms. The signal is obtained from the fluctuations in the intensity of the light measured by photo-diodes.

The detector outputs are affected by a number of noise events and non-stationarities which can contain and hide the signal of transient bursts, weak continuous and periodic sources or the stochastic background.

To reduce the noise as much as possible, the laser beam is enclosed in high-vacuum pipes, with both acoustic and electromagnetic isolation. Moreover, the mirrors are decoupled from seismic fluctuations through the use of sophisticated super-attenuators. These are composed of an eight meters chain of five mechanical pendula, with three elastic connections to the ground, forming an inverse pendulum. The whole detector site is monitored constantly by microphones, magnetometers, photo-diodes, seismometers, monitors for current and voltage, cameras and thermometers. All of these sensors cooperate in tracing the noise sources, helping the Virgo staff in reducing them or at least in producing vetoes to remove false-alarms.
The usual noise control pipeline follows these actions:

1. Identify the events
2. Correlate the event with detector problems or human or environmental disturbance
3. Check the event against scheduled events (start/stop of some devices, ...)
4. Find out how many channels are interested by the event
5. Find out how the noise event couples with the detector signal
6. Remove the noise source and/or reduce the coupling with the detector signal.

Known sources of noise are: seismic activity, acoustic noise (from the internal apparatus but even from the airplanes flying over the site), electrical glitches, laser instability, dust (or spiders and flies) crossing the laser beam in the part not in vacuum, alignment problems, thermal disturbance, mirror glitches, ...
Along the noise monitoring, GW searches operate in parallel with different methods and aims. Searches are performed to look for a variety of transient signals, spanning all the frequencies and without a precise model of waveform. Targeted searches are focused on few candidates already known by

radio/optical observations, while all-sky searches produce a list of candidate continuous wave signals to be verified. In the case of confirmed signals, an alert would be triggered to activate the EM follow-up searching for a visible (X-ray/optical/radio) counterpart.
Virgo, LIGO and GEO600 collaborate in forming a network of GW detectors. The possibility to observe GW events from multiple detectors can reduce the number of false-alarms due to instrumental or environmental noise. However, coincidence in the detector glitches happened. More details about the noise sources, modelling and countermeasures can be found in Aasi et al., 2012.
A network of detectors also allows a better sky localization of the sources, though uncertainty regions in sky are still of the order of tens of square degrees.
GW detection using interferometers is not necessarily limited to ground based installations. A project was proposed by NASA about using three satellites to build a laser interferometer in space. These detector, with triangular shape, would be able to detect GWs with frequencies lower than Virgo and LIGO, allowing the observations of DCOBs inspirals and emission by binary WDs. The project was stopped due to budget problems and is now reborn as eLISA (enhanced LISA), an ESA mission. The new launch date is expected in ~ 2034.

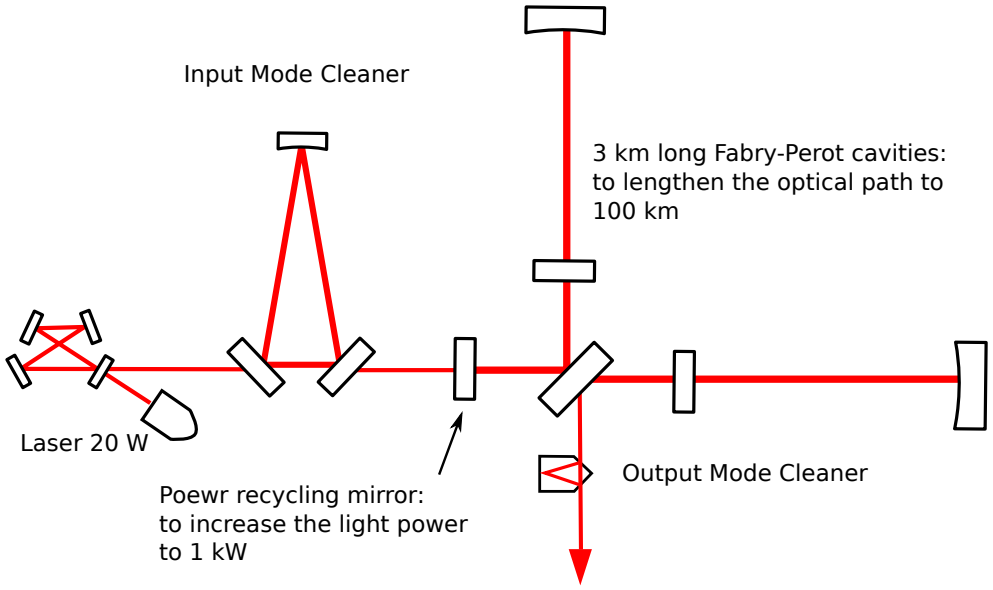

Figure 1.10: Simple scheme of the Virgo interferometer. The red lines represent the laser path across the detector. After the laser beam is generated, the laser modes are cleaned to make it as monochromatic as possible and then the laser beam is injected into the interferometer. Along the optical path some mirrors and cavities are used to increase the power and to lengthen the optical path. The laser beam is split with a beam splitter and reflected at the end of the two arms. Then, the two beams are recombined and interfere before hitting the photo-detector.

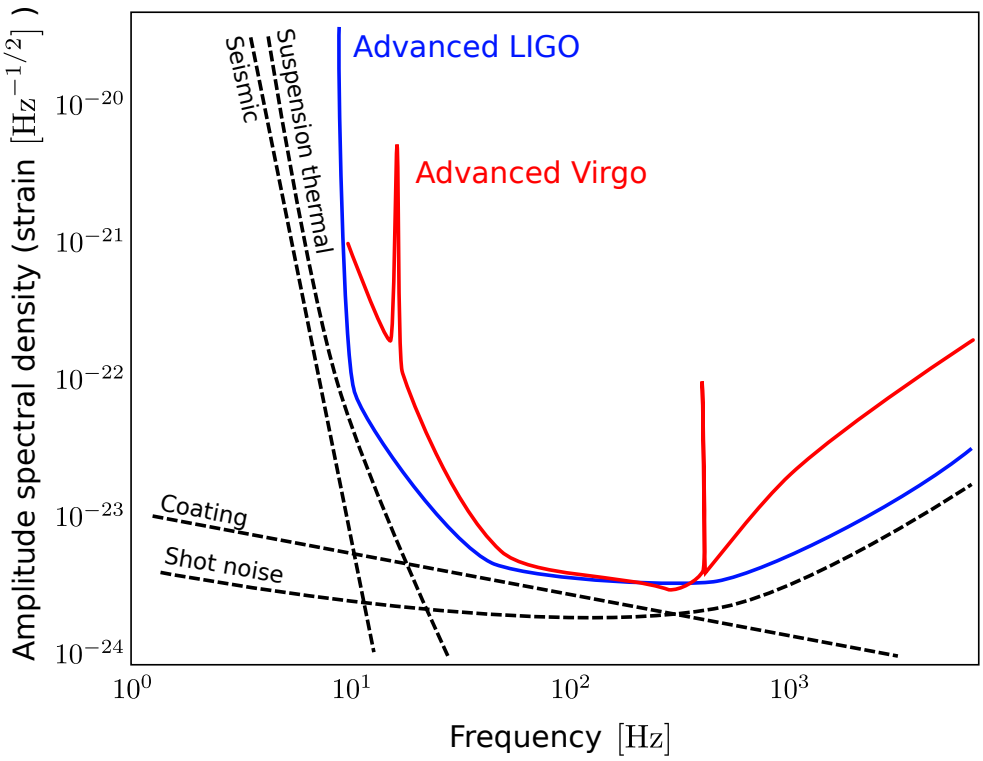

Figure 1.11: **Red and blue solid lines:** sensitivity of Advanced Virgo and Advanced LIGO as a function of the GW frequency. **Black dashed lines:** noise sources and their magnitude. Adapted from Pitkin et al., 2011

CHAPTER 2

DYNAMICS OF STELLAR SYSTEMS

An (isolated) self-gravitating system is affected by several processes driving its evolution: dynamical interactions between stars, evaporation, core collapse, dynamical friction, formation and evolution of binaries, ... Before considering how stars are affected by the presence of the other stars in a self-gravitating system, it is necessary to introduce the distinction between collisional and collisionless stellar systems.
Quoting Binney and Tremaine (2008):

> "In collisional systems individual stellar encounters gradually perturb stars away from the trajectories they would have taken if the gravitational field were perfectly smooth. Stars diffuse in the phase space away from their original orbits. After many encounters the star eventually loses its memory of the original orbit and find itself on a wholly unrelated one."

Thus, collisional systems are systems were dynamical stellar encounters play an important role in determining the orbits of the stars, while in collisionless

ones stars move under the influence of a smooth potential and encounters between two stars are rare and not important. A dynamical encounter can be defined as the gravitational perturbation of the orbit of one star by another.

The characteristic time over which dynamical encounters are able to modify the system is called two body relaxation timescale. After a relaxation time the velocity distribution has changed significantly and stars have lost memory of their previous velocity state. In collisional systems the approximation of a smooth gravitational potential is not correct over timescales exceeding the relaxation timescale.

Section 2.1 introduces the concept of relaxation timescale, Section 2.2 recalls some of the models describing collisionless systems, while Section 2.3 presents the features of collisional ones. In Section 2.4 we explore the role of binary systems in the star cluster evolution. Finally, Section 2.5 is devoted to the numerical methods adopted in simulating star clusters.

2.1 Two-body relaxation

Two-body relaxation is one of the most important dynamical processes in a self-gravitating system. Since gravity is a long range force, each star is subject to the gravitational attraction of every other star in the system. The cumulative effect of these long range interactions is to gradually change the star orbit until it loses memory of its initial trajectory and velocity. Globally, relaxation modifies the velocity distribution of the system redistributing energy throughout the whole cluster. An accurate calculation of the relaxation timescale, including diffusion coefficients, can be found in Spitzer and Hart (1971) and yields:

$$t_{\rm rlx} = 0.34 \frac{\sigma^3}{G^2 m \rho \ln \Lambda} \tag{2.1}$$

where σ is the velocity dispersion, ρ is the mass density, m is the average mass of a star, G is the gravitational constant and $\ln \Lambda$ is defined as

$$\ln\Lambda \equiv \ln\left(\frac{b_{\max}}{b_{\min}}\right) \simeq \ln\left(\frac{R}{b_{90}}\right) \tag{2.2}$$

where $[b_{\min}, b_{\max}]$ is the range of the impact parameters, R is the size of the system and $b_{90} \equiv \frac{G(m_1+m_2)}{v_0^2}$ is the impact parameter for a dynamical encounter (between two stars of mass m_1 and m_2, and relative velocity v_0) at which the deflection angle is $\theta_{\rm defl} = \frac{\pi}{2}$. The relaxation timescale can also be defined locally by taking $\langle m\rangle_{\rm local}$ and $\rho_{\rm local}$. The value of Λ can range from $0.4N$ (where N is the number of stars in the system, Spitzer, 1987) in the theoretical case of equal mass stars, homogeneous distribution and isotropic velocity distribution, to empirical $0.11N$ (Giersz and Heggie, 1994) for systems with equal mass stars to even lower values in case of a realistic mass range. N is the total number of stars in the system. If the cluster is in virial equilibrium the averages can be taken system-wide and we can substitute $\langle v^2\rangle = GM/2r_{\rm vir}$ and $\rho \sim 3M/8\pi r_{\rm vir}$ in (2.1) obtaining

$$\begin{aligned} t_{\rm rlx} &= \frac{\langle v^2\rangle^{3/2}}{15.4G^2\langle m\rangle\rho\ln\Lambda} = \frac{(GM/2r_{\rm vir})^{3/2}}{15.4G^2\langle m\rangle(3M/8\pi r_{\rm vir}^3)\ln\Lambda} \\ &= 0.14\frac{N^{1/2}r_{\rm vir}^{3/2}}{G^{1/2}\langle m\rangle^{1/2}\ln\Lambda} \\ &\sim 2\times10^8\,{\rm yr}\left(\frac{M}{10^6M_\odot}\right)^{1/2}\left(\frac{r_{\rm vir}}{1\,{\rm pc}}\right)^{3/2}\left(\frac{\langle m\rangle}{M_\odot}\right)^{-1} \end{aligned} \tag{2.3}$$

where, in the last step $\ln\Lambda \sim 10$ is adopted as appropriate for the young massive cluster. I investigate, $\langle m\rangle$ is the average stellar mass, M is the system mass and $r_{\rm vir}$ is the virial radius.

The two-body relaxation timescale is very simple to derive if we assume that the stellar system has radius R with equal-mass stars, initially moving at the same speed $v_{\rm i}$, and homogeneous density. Under such assumptions the two-body relaxation timescale is simply given by

$$t_{\rm rlx} \sim \frac{0.1N}{\ln N}t_{\rm cross} = \frac{0.1N}{\ln N}\frac{R}{v} \tag{2.4}$$

where $t_{\rm cross}$ is the time a star needs to cross the system, and v the star speed. Comparing the relaxation timescale to the lifetime of the system we can classify stellar systems as collisional and collisionless. If the relaxation timescale is shorter than the lifetime of the system, dynamical interactions are efficient and the system is collisional. In contrast, if the relaxation timescale is longer than the lifetime, stars mainly move under the influence of the average smoothed potential and the effect of single encounters is negligible.
If $t_{\rm rlx}$ is longer than the lifetime of the system, then the system is collisionless. Because the local relaxation timescale can span a wide range of values among different regions of a system, often in literature a single reference version is adopted, the half-mass relaxation timescale (Spitzer, 1987):

$$\begin{aligned} t_{\rm hmrlx} &= \frac{0.17N}{\ln\Lambda}\sqrt{\frac{r_{\rm hm}^3}{GM}} \\ &= \frac{0.78\,{\rm Gyr}}{\ln\Lambda}\frac{1\,{\rm M}_\odot}{m}\left(\frac{M}{10^5\,{\rm M}_\odot}\right)^{1/2}\left(\frac{r_{\rm hm}}{1\,{\rm pc}}\right)^{3/2} \end{aligned} \tag{2.5}$$

obtained by considering the half-mass radius $r_{\rm hm}$, i.e. the radius containing half of the total mass of the system, the mean density inside the half-mass radius $(M/2)/\left(\frac{4\pi}{3}r_{\rm h}^3\right)$ and replacing 3σ with $\langle v^2\rangle$. In this case

$$\Lambda = \frac{r_{\rm h}\langle v^2\rangle}{2Gm} = \lambda N \sim 0.1N \tag{2.6}$$

(Giersz and Heggie, 1994).
This expression holds if the velocities of the stars are isotropic.

2.2 Describing collisionless stellar systems

Modeling stellar systems can, in principle, be easily achieved by considering the potential of every single body and adding them together. Unfortunately, this approach is not convenient for evolving in time more than 10^6 particles nor feasible for more than 10^{11}. In case of collisionless systems, what people

usually do is to smooth the potential on a scale much smaller than the size of the system but larger than the mean distance among particles. Then, the orbit of a single star or a star cluster in a galaxy is well studied considering it a test particle in a smooth (analytical) potential and the evolution of the cluster is described by a distribution function. Here I will recall two dynamical models of stellar systems that are useful for this work.

2.2.1 Plummer model

The Plummer (1911) model is often used to describe star clusters, bulges of galaxies or entire galaxies because of its simple functional form. The Plummer distribution function is derived from a polytrope with index $n = p + \frac{3}{2} = 5$:

$$f = \begin{cases} const(-E)^p & \text{for } E < 0 \\ 0 & \text{for } E \geq 0 \end{cases} \tag{2.7}$$

Where E is the energy of a particle and $const$ is an arbitrary constant.
The potential is given by:

$$\phi(r) = -\frac{GM}{(r^2 + a^2)^{1/2}} \tag{2.8}$$

where a is the Plummer scale parameters, M the total mass and $r = \sqrt{x_1^2 + x_2^2 + x_3^2}$.
We can derive the density distribution from the Poisson equation:

$$\begin{aligned} \rho(r) &= \frac{\nabla^2\phi(r)}{4\pi G} = \frac{1}{4\pi G}\frac{1}{r^2}\frac{\mathrm{d}}{\mathrm{d}r}\left[r^2\frac{\mathrm{d}}{\mathrm{d}r}\phi\right] \\ &= \frac{3a^2M_1}{4\pi(r^2+a^2)^{5/2}} = \frac{3M}{4\pi a^3}\left(1+\frac{r^2}{a^2}\right)^{-\frac{5}{2}} \end{aligned} \tag{2.9}$$

Then, from the density we can obtain the cumulative mass distribution:

$$M(r) = 4\pi\int_0^r r^2\rho(r)\,\mathrm{d}r = \frac{4\pi}{4\pi G}\int_0^r r^2\frac{1}{r^2}\frac{\mathrm{d}}{\mathrm{d}r}\left[r^2\frac{\mathrm{d}\phi(r)}{\mathrm{d}r}\right] \tag{2.10}$$

$$= \frac{r^2}{G}\nabla\phi(r) = \frac{Mr^3}{\left(r^2+a^2\right)^{3/2}} \tag{2.11}$$

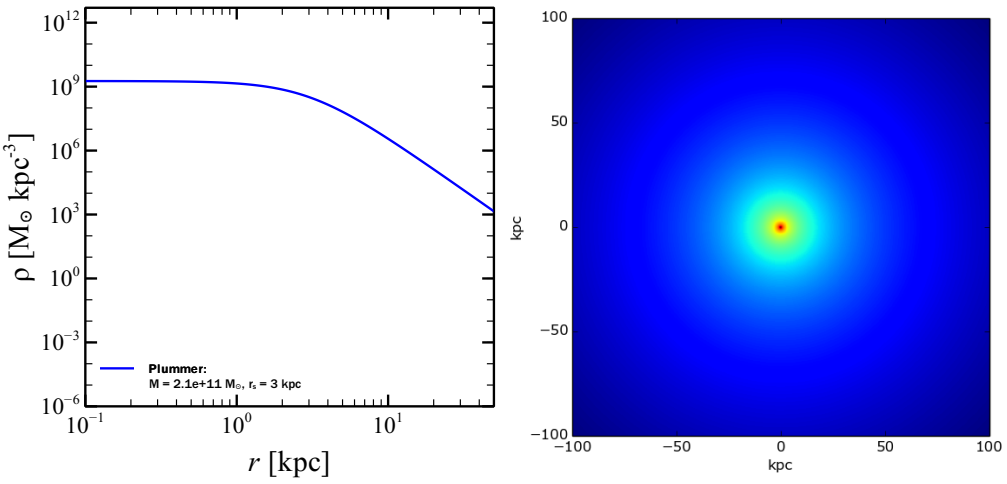

Figure 2.1: Radial density profile and colormap of a Plummer sphere. The physical parameters are total mass $M = 2.1 \times 10^{11}\,\mathrm{M}_\odot$ and scale radius $a = 3\,\mathrm{kpc}$.

It can be shown that the acceleration and the jerk (time derivative of the acceleration) are:

$$a_i(r) = -\frac{x_i GM}{(r^2 + a_i^2)^{3/2}} \tag{2.12}$$

$$j_i(r) = -\frac{GM}{(r^2 + a^2)^{3/2}} \left[v_i - \frac{3x_i(\mathbf{x}\cdot\mathbf{v})}{r^2 + a^2} \right] \tag{2.13}$$

where the subscript i refers to the single coordinate and x_i, v_i are the values of position and the velocity in that coordinate frame. It follows that $\mathbf{x} = \sum x_i \hat{e}_i$ and $\mathbf{v} = \sum v_i \hat{e}_i$, being $\hat{e}_i$ the unit vector in the i direction.

2.2.2 King model

The King model was introduced to describe globular clusters. This model is analogous to an isothermal sphere ($\rho(r) \propto r^{-2}$)at intermediate radii but has a non singular core and it is truncated at a certain distance from the center, i.e. the tidal radius r_t. Stars beyond the tidal radius are stripped from the cluster

by the galactic tidal field (Elson, Hut, and Inagaki, 1987). The King model also provides a good fit to the observations.

To obtain a King model, we need to define a steady-state gravitational potential $\Phi(\mathbf{x})$. The Hamiltonian H of the system is $\Phi(\mathbf{x}) + \frac{1}{2}v^2$. We also define a constant Φ_0 and a relative potential and a relative energy for a star in the system

$$\Psi \equiv -\Phi + \Phi_0 \tag{2.14}$$

$$\epsilon \equiv -H + \Phi_0 = -\Phi - \frac{1}{2}v^2 + \Phi_0 = \Psi - \frac{1}{2}v^2. \tag{2.15}$$

The constant Φ_0 is chosen to let the DF f positive when ϵ is positive and zero when $\epsilon \leq 0$. Moreover, we include a constant ρ_1 to normalize the integral of the DF to the unity.

Thus, the distribution function has the form

$$f = \begin{cases} \rho_1 (2\pi\sigma)^{-3/2} \left[\exp\left(\dfrac{-\Phi - \frac{1}{2}v^2 + \Phi_0}{\sigma^2} \right) - 1 \right] & \text{for } \epsilon > 0 \\ 0 & \text{for } \epsilon \leq 0 \end{cases} \tag{2.16}$$

with $\epsilon \equiv -H + \Phi_0 = -\Phi - \frac{1}{2}v^2 + \Phi_0$.

This DF describes the family of King (1966) models.

Integrating over all velocities we obtain the density as a function of the potential

$$\begin{aligned} \rho(-\Phi + \Phi_0) &= \frac{4\pi\rho_1}{(2\pi\sigma^2)^{3/2}} \int_0^{\sqrt{2(-\Phi+\Phi_0)}} \mathrm{d}v\, v^2 \left[\exp\left(\frac{-\Phi - \frac{1}{2}v^2 + \Phi_0}{\sigma^2} \right) - 1 \right] \\ &= \rho_1 \left[\exp\left(\frac{-\Phi + \Phi_0}{\sigma^2} \right) \mathrm{erf}\left(\frac{\sqrt{-\Phi + \Phi_0}}{\sigma} \right) + \right. \\ &\quad \left. - \sqrt{\frac{4(-\Phi + \Phi_0)}{\pi\sigma^2}} \left(1 + \frac{2}{3} \frac{-\Phi + \Phi_0}{\sigma^2} \right) \right] \end{aligned} \tag{2.17}$$

with $\mathrm{erf}(x) = \frac{2}{\sqrt{(\pi)}} \int_0^x e^{-t^2}\, \mathrm{d}t$.

Thus, the Poisson's equation becomes:

$$\frac{\mathrm{d}^2}{\mathrm{d}r^2}(-\Phi+\Phi_0)+\frac{2}{r}\frac{\mathrm{d}}{\mathrm{d}r}(-\Phi+\Phi_0)+ 4\pi G\rho_1\left[\exp\left(\frac{-\Phi+\Phi_0}{\sigma^2}\right)\mathrm{erf}\left(\frac{\sqrt{-\Phi+\Phi_0}}{\sigma}\right)+ -\sqrt{\frac{4(-\Phi+\Phi_0)}{\pi\sigma^2}}\left(1+\frac{2}{3}\frac{-\Phi+\Phi_0}{\sigma^2}\right)\right]=0 \tag{2.18}$$

This has to be solved numerically.
If we introduce:

- the normalized density $\tilde{\rho}\equiv\frac{\rho}{\rho_0}$ with $\rho_0=\rho(r=0)$,
- the normalized radius $\tilde{r}\equiv\frac{r}{r_0}$ with
- $r_0\equiv\sqrt{\frac{9\sigma^2}{4\pi G\rho_0}}$ being the King radius (also called core radius) and σ the velocity dispersion
- and the adimensional potential $W\equiv\frac{\Psi}{\sigma^2}$

we obtain a form of the Poisson's equation often found in literature:

$$\frac{\mathrm{d}^2W}{\mathrm{d}\tilde{r}^2}+\frac{2}{\tilde{r}}\frac{\mathrm{d}W}{\mathrm{d}\tilde{r}}+9\tilde{\rho}(W,W_0)=0 \tag{2.19}$$

with

$$\tilde{\rho}(W,W_0)=\frac{e^W\mathrm{erf}\left(\sqrt{W}\right)-\sqrt{\frac{4}{\pi}}\left(1+\frac{2}{3}W\right)}{e^{W_0}\mathrm{erf}\left(\sqrt{W_0}\right)-\sqrt{\frac{4}{\pi}}\left(1+\frac{2}{3}W_0\right)} \tag{2.20}$$

$W(\tilde{r}=0)=\frac{\Psi(r=0)}{\sigma^2}=W_0$ represents the depth of the central potential well and it is usually used to parametrize a King model together with the virial radius r_v . W_0 is also related to the concentration of a star cluster. The concentration is defined as

$$c\equiv\log_{10}\left(\frac{r_\mathrm{t}}{r_0}\right) \tag{2.21}$$

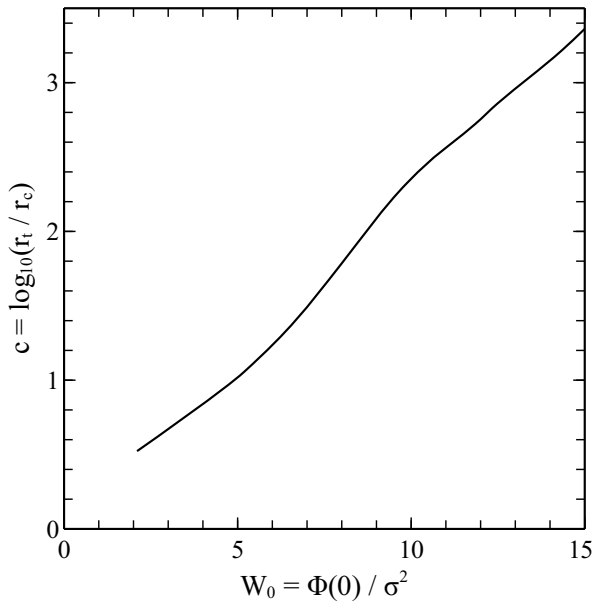

Figure 2.2: Plot of the relation between the concentration of a cluster and the value of the central adimensional potential W_0 (from Binney and Tremaine (2008)).

where r_t is the tidal radius, defined as $\rho(r_t) = 0$ and $\Psi(r_t)$.

The relation between the concentration and W_0 is shown in figure 2.2

From equation (2.14) we find

$$\Psi(r_t) = 0 = \Phi(r_t - \Phi_0) \tag{2.22}$$

thus

$$\Phi_0 = \Phi(r_t) = \frac{GM(r_t)}{r_t} \tag{2.23}$$

and

$$\Psi(r = 0) = \Phi(r_t) - \Phi(r = 0) \tag{2.24}$$

2.3 Evolution of a collisional system

In collisional clusters, dynamical encounters do matter for the system evolution. Based on the equipartition theorem, two body interactions are expected to lead to energy equipartition. Energy equipartition means $m\langle v^2\rangle \sim const$ for all the stars, where the average has to be intended as average on the time. Thus, faster stars tend to slow down while slower stars tend to speed up.
Star clusters in the universe are not composed of equal-mass star particles. If a cluster has a realistic mass function, stars with higher masses tend to slow down while lighter stars speed up to achieve energy equipartition. As a result, the cluster becomes mass segregated, i.e. the massive stars, losing kinetic energy, fall deeper into the potential well, while lighter stars move towards the outer parts of the system. The timescale for a massive star with mass $M_\star$ to sink to the center is (Spitzer, 1969):

$$t_{\rm sink}(M_\star) \propto \frac{\langle m\rangle}{M_\star} t_{\rm rlx}(\langle m\rangle) \tag{2.25}$$

where $\langle m\rangle$ is the average stellar mass in the cluster.
Let us consider a cluster with potential $\Phi(\mathbf{x})$ and two population of equal-mass stars $i = 1,2$ with masses $m_2 > m_1$. We also assume that the total mass of the lighter and of the heavier stars are M_1 and M_2, respectively, with $M_1 > M_2$. The two populations have mean energy per star given by

$$\langle E\rangle_i = m_i\langle\frac{1}{2}v^2 + \Phi(\mathbf{x})\rangle_i \tag{2.26}$$

Equipartition does not mean that, $\langle E\rangle_1 \rightarrow \langle E\rangle_2$. i.e. it does not imply that the total average energy of population 1 tends to become equal to the total average energy of population 2.
What happen is that encounters tend to establish equipartition of kinetic energy locally. This means that $m_1\langle v^2\rangle_1 \rightarrow m_2\langle v^2\rangle_2$ in a given region by transferring energy. At this point, the heavier stars are slowed down and sink to the center, where the orbital speeds are higher due to the deeper potential.

The net result is that equipartition increases the kinetic energy of the more massive stars.

2.3.1 Spitzer's instability

It is possible to demonstrate that equipartition can not always be established. For a cluster with two populations of equal-mass stars (as in the previous Section), equipartition can be reached if

$$M_2 \leq \rho_{\rm c1} r_{\rm c1}^3 \frac{1.61}{fg} \left(\frac{m_1}{m_2}\right)^{3/2} \tag{2.27}$$

where M_2 is the total mass of the population of heavier stars, $\rho_{\rm c1}$ is the density of the central core of lighter star system, at the center of which the heavier stars accumulated. $r_{\rm c1}$ is the radius of the lighter star system and $f \sim 0.45$ and $g \sim \mathcal{O}(1)$.

If the condition is not fulfilled, the heavy stars form an independent sub-system in the center of the cluster and continue to lose kinetic energy in favor of the lighter ones. This energy loss, according to the virial theorem, causes the velocity dispersion of heavy stars to increase, turning them away from equipartition. As a consequence, the process of energy loss, heating, contraction of the massive star sub-system continues indefinitely.

This phenomenon is called equipartition (or Spitzer's) instability (Spitzer, 1969; Spitzer, 1987).

In real systems, what happens is that equipartition causes a core of heavy stars to form inside the core of the cluster which evolves independently from the rest of the cluster. At a certain point the gravothermal instability becomes more important than the equipartition instability and this sub-core behaves just like the core of a equal mass cluster (see Section 2.3.3). Thus, the effect of the equipartition instability in a multi-mass system is to accelerate the core collapse from $\sim 16\, t_{\rm hmrlx,i}$ to $\sim 2-4\, t_{\rm hmrlx,i}$ where $t_{\rm hmrlx,i}$ is the initial half mass relaxation timescale.

Another consequence of the equipartition is the speed up of the evaporation of light stars (see next Section).

2.3.2 Evaporation and ejection

Two mechanisms contribute to the escape of stars from a cluster. The first one is a single close encounter that leaves one of the stars with a speed larger than the escape speed. This process is called ejection. The second is the cumulative effect of weaker interactions with distant stars that sum up until the star has a positive energy and can leave the system. This process is called evaporation.
For an idealized cluster, modeled as an isolated Plummer sphere with all the particles with the same mass, Hénon (1960) calculated the ejection rate as

$$\frac{\mathrm{d}N}{\mathrm{d}t} = -1.05 \times 10^{-3} \frac{N}{t_{\mathrm{hmrlx}} \ln(\lambda N)} \tag{2.28}$$

where t_{hmrlx} is the half-mass relaxation time and $\ln(\lambda N)$ is the Coulomb logarithm. Thus, the ejection time is

$$t_{\mathrm{ej}} = -\left(\frac{1}{N}\frac{\mathrm{d}N}{\mathrm{d}t}\right)^{-1} = 1 \times 10^{3} \ln(\lambda N)\, t_{\mathrm{hmrlx}} \tag{2.29}$$

The ejection timescale is longer than the evaporation timescale for typical values of the Coulomb logarithm. For this reason, when dealing with evaporation, usually ejection can be neglected.
Moreover, evaporation is dominated by stars with elongated orbits, extending from the dense core to the halo of the cluster.
It can be shown (Spitzer, 1987) that the time an isolated equal-mass cluster need to completely evaporate is

$$t_{\mathrm{evap}} = -N\frac{\mathrm{d}t}{\mathrm{d}N} \sim 300\, t_{\mathrm{hmrlx}} \tag{2.30}$$

The evaporation timescale is longer than the expected time for the core collapse thus only few stars escape the system before the core contracts. After the core collapse the cluster expands and the evaporation slows down. For typical

globular clusters the time needed to evaporate the entire system is larger than the lifetime of the system. In this scenario, however, tidal forces from the host galaxy can play a central role in speeding up the evaporation. The post core-collapse expansion makes the stellar loss even faster by placing stars beyond the tidal radius.

The evaporation timescale found above for an idealized system, $t_{\rm evap} \sim 300\, t_{\rm hmrlx}$, has to be considered as an upper limit. Many of the physical processes we did not account for act in speeding up the evaporation: a mass spectrum, tidal forces, physical collisions and inelastic encounters, gravitational radiation in the densest systems.

Moreover, it is possible to take into account the fact that the escapers can orbit many times the cluster before reaching the Lagrangian point and leave the system (Baumgardt, 2001; Fukushige and Heggie, 2000; Baumgardt and Makino, 2003).

A useful approximation is

$$t_{\rm dis} \sim 2{\rm Myr}\left(\frac{N}{\ln\Lambda}\right)^{3/4}\left(\frac{R_{\rm G}}{1{\rm kpc}}\right)\left(\frac{V_{\rm G}}{220{\rm kms}^{-1}}\right)^{-1}(1-e) \tag{2.31}$$

$$\propto N^{0.65}, \text{ for } M_{\rm SC} \text{ in } 10^3 - 10^6\,{\rm M}_\odot \tag{2.32}$$

where e is the eccentricity of the orbit (Lamers, Gieles, and Portegies Zwart, 2005), $M_{\rm SC}$ is the cluster mass, $R_{\rm G}$ and $v_{\rm G}$ are the apogalactic distance and the velocity at such distance (assuming circular speed) in a logarithmic potential.

2.3.3 The thermodynamics of self-gravitating systems

A self-gravitating system can be described in analogy with ideal gases. One can define its temperature T at a certain position with

$$\frac{1}{2}m\langle v^2\rangle = \frac{3}{2}k_{\rm B}T \tag{2.33}$$

where $k_{\rm B}$ is the Boltzmann's constant. Thus, the total kinetic energy of a system composed by N bodies is $K = \frac{3}{2}Nk_{\rm B}T$.

If we consider a stationary system, in virial equilibrium, we have

$$E = -\frac{3}{2} N k_{\rm B} \langle T \rangle \tag{2.34}$$

where $\langle T \rangle = \int \mathrm{d}^3\mathbf{x}\rho(\mathbf{x})T / \int \mathrm{d}^3\mathbf{x}\rho(\mathbf{x})$ is the mass-weighted mean temperature. Then, the heat capacity of the system is

$$C \equiv \frac{\mathrm{d}E}{\mathrm{d}T} = -\frac{3}{2} k_{\rm B} < 0 \tag{2.35}$$

A negative heat capacity means that the system becomes hotter when losing energy (Lynden-Bell and Wood, 1968, Lynden-Bell, 1999).

This is a general results: any (gravitationally) bound (finite) system behave like this.

Modeling stellar systems through thermodynamics has the advantage that the math is easy and allows to find interesting results without too much effort.

It is, however, worth noting, that many statistical mechanics results does not apply to stellar systems, characterized by long-range forces (Padmanabhan, 1990, Lynden-Bell, 1999, Katz, 2003). First of all, as we have seen above, heat capacity is not positive. But also energy is not extensive, which means that the total energy is not the sum of the energies of its sub-parts. The consequence is that the system lose more energy becoming even hotter in a runaway process that leads the core to contract more and more. This process is known as core collapse. The halo, on the contrary, expands.

During the core collapse the inner region should reach infinite density. However, singularities are the expression of a model breakdown. What occur is that we need to take into account some process that become important in this stage and provide a heat source for the system. The two processes we need to consider now are the binary formation and the mass loss for stellar evolution. The latter decreases the total binding energy per unit mass increasing the velocity dispersion. Binary formation and evolution will be presented in more detail in Section 2.4.

2.3.4 Inelastic encounters

In dense stellar systems it is not always possible to consider stars as point masses. Sometimes the environment is so dense that it is possible for two stars to find themselves so close that strong tidal forces arise. They can also collide. Very close interactions can produce binaries and reduce the overall kinetic energy of the system because of energy dissipation. These, and the physical collisions, can also result in the coalescence of the two stars that merges into a single one.
The characteristic timescale on which a star can collide is

$$t_{\rm coll} \sim \frac{1}{n v \Sigma} \tag{2.36}$$

where n is the star number density, v the root mean square stellar velocity and Σ the collision cross-section.
Forgetting about gravitational focusing, this estimate can be rewritten considering $n \sim N/r^3$, $\Sigma \sim \pi(2r_\star)^2$ and $t_{\rm cross} \sim r/v$:

$$t_{\rm coll} \sim \frac{r^2}{4\pi N r_\star^2} t_{\rm cross} \tag{2.37}$$

Then, by introducing the virial theorem and the escape speed from stellar surface, we have $v^2 \sim GNm/r$ and $v_\star = \sqrt{2Gm/r_\star}$, with $v_{\star,\odot} = 618\,{\rm kms}^1$.
Thus

$$t_{\rm coll} \sim 0.02N\left(\frac{v_\star}{v}\right)^4 t_{\rm cross} \sim 0.2\left(\frac{v_\star}{v}\right)^4 \ln(N)\, t_{\rm rlx} \tag{2.38}$$

When modeling the dynamics of a star cluster, stars are usually treated as point masses and this approximation works fine. There are, however, situations in which it becomes necessary to deal with the physical size of stars. In the densest regions of a cluster, for example in the core during the final stages of the collapse, stars can find themselves so close that they collide. Even if a physical collision does not occur, the distance can be short enough that tidal forces between the two stars become important.

2.4 Binaries and multiple systems

2.4.1 Binary formation

In a cluster binaries can form in three different ways. First, they can be primordial, i.e. two stars form at the same time bound to each other. Here we must recall that the relative motion of two point masses during an isolate encounter is always a hyperbola (Binney and Tremaine, 2008). For this reason it is not possible to form a binary system with two point masses only. The presence of a third body, however, allows two of them to become bound in a Keplerian orbit.

The time for a star to become part of a binary through a triple encounter is (Goodman and Hut, 1993)

$$t_3 \sim \frac{v^9}{n^2 G^5 m^5} \sim 10\, t_{\rm rlx} N^2 \ln N \tag{2.39}$$

The third formation pathway is a tidal capture: a two-body encounter might result in the formation of a binary system if the two stars pass each other within few stellar radii and the tidal dissipation allows the capture (Elson, Hut, and Inagaki, 1987; McMillan, McDermott, and Taam, 1987). Such binaries, however, are so close that they are almost irrelevant for the cluster dynamics because their impact parameter is so small that is it very difficult for them to change their orbital properties interacting with another star.

The last two binary formation paths are much more likely to occur in the central region of the cluster, especially during the core collapse, since the higher density favors these processes. Because the rate of binary formation strongly depends on the density, the core adjusts itself producing the right amount of binaries necessary to stop the core collapse. Once the core collapse has stopped, the density decreases and so does the binary formation (Hénon, 1961).

Binaries and cluster dynamics

In section 2.3.3, I anticipated that binaries have a central role in the dynamical evolution of the cluster. Binary formation and interaction between a binary and a single star may result in energy transfers that change the energy balance of the cluster.

First, it can be useful to recall that the internal energy of a binary is defined as the total energy of the binary minus the kinetic energy of the center-of-mass:

$$E_{\rm int} = \frac{1}{2}\mu v^2 - \frac{G m_1 m_2}{r} \tag{2.40}$$

where $\mu = \frac{m_1 m_2}{m_1+m_2}$ is the reduced mass of the binary and r and v the relative velocity and separation.

The binary is bound if $E_{\rm int} < 0$. In this situation, the orbit of the reduced particle is a Kepler ellipse with semi-major axis a. The binding energy is

$$E_{\rm b} = G\frac{m_1 m_2}{2a} = -E_{\rm int} \tag{2.41}$$

Let us consider now a dynamical encounter between the binary and a single star. There are three possibilities: i) the binary transfers some internal energy to its center of mass and to the center of mass of the single star in the form of kinetic energy; ii) the viceversa, i.e. the binding energy grows at the expense of the kinetic energy of the centers of mass; iii) if it is energetically convenient the single star may take the place of one of the members of the binary producing a new binary with a binding energy larger than the previous binary. An exchange is likely to occur if the mass of the single star is larger than the mass of one of the members of the binary.

In the first case the semi-major axis of the binary decreases while both the binary and the single star increase their velocity. In the second, case the single star and the binary center of mass slow down and the binary becomes less bound (at the extreme become unbound, i.e. it is ionized). The last possibility, called exchange, produces a new, more bound binary and speeds up the two centers of mass.

It is not possible to predict what would happen during a dynamical encounter exactly, however, we can outline statistical behaviors.

Binaries can be subdivided in hard and soft, whether or not their binding energy is larger than the average kinetic energy of a star in the proximity (or in the cluster, for simplicity):

$$E_{\mathrm{b}} = \frac{G m_1 m_2}{2a} \lessgtr \frac{1}{2}\langle m \rangle \sigma^2 \tag{2.42}$$

On average, hard binaries tend to become harder while soft binaries tend to become softer (Heggie, 1975).

Finally, a single star can ionize a binary if its velocity, before being perturbed by the binary, exceeds the critical velocity.

To obtain value of the critical velocity we require that the kinetic energy of the reduced particle of the 3-body system equals the binding energy of the binary:

$$\frac{1}{2}\frac{m_3(m_1+m_2)}{(m_1+m_2+m_3)} v_{\mathrm{c}}^2 = \frac{G m_1 m_2}{2a} \tag{2.43}$$

thus

$$v_{\mathrm{c}} = \sqrt{\frac{G m_1 m_2 (m_1+m_2+m_3)}{m_3(m_1+m_2)a}}. \tag{2.44}$$

To have an idea of how much binaries can impact on the cluster dynamics we can make a qualitative comparison. The binding energy of a globular cluster with mass $M \sim 10^5\,\mathrm{M}_\odot$ and $r \sim 2\,\mathrm{pc}$ is (assuming it is homogeneous, which it is not, but here we only need an approximation) $E_{\mathrm{b,cluster}} \sim \frac{3}{5}\frac{GM^2}{r} \sim 2.5 \times 10^{50}\,\mathrm{erg}$. On the other hand, a two $10\,\mathrm{M}_\odot$ star binary separated by $2\mathrm{R}_\odot$ has binding energy $E_{\mathrm{b,binary}} = \frac{G m_1 m_2}{r} \sim 4.8 \times 10^{49}$, that is 20% the binding energy of the entire cluster. It is easy to understand that few binaries can change the dynamical trend of a cluster, for example reversing the core collapse.

2.5 Simulating stellar systems

In the previous sections I presented how stellar systems can be described and which processes dominate their evolution. But how can we follow the evolution of a gravitationally self-bound ensemble of stars in detail?
In 1687 Newton expressed the problem of studying the motion of N point-like masses interacting through their mutual gravitational attraction. Then, in 1710 Bernoulli provided a complete solution only for N=2. The problem rose so much attention that in 1885 a challenge was proposed to be answered before 21st January 1889, in honor of the 60th birthday of King Oscar II of Sweden and Norway.
The problem to be solved was:

> Given a system of arbitrarily many mass points that attract each according to Newton's law, under the assumption that no two points ever collide, try to find a representation of the coordinates of each point as a series in a variable that is some known function of time and for all of whose values the series converges uniformly.

Nobody submitted a correct answer. A century later, Wang (1991) found a convergent power series solution for a generic number of bodies. However, Wang solution even if is mathematically correct, it is not of much help because of the large number of terms to be added in order to obtain a sufficiently accurate solution and the slowness of the convergence.
Thus, the only way left is to solve the problem numerically.

2.5.1 Historical perspective

The first attempt in modeling stellar systems "numerically" can be attributed to Holmberg (1941) who realized a simulation of a stellar system with light bulbs, where the light hitting photo-detectors attached to each bulb represented the gravitational field felt by the corresponding body. Then, the first numerical simulations were performed by von Hoerner, 1960 and Aarseth, 1963 with 16

and 100 particles. Since then the computational facilities and the algorithms evolved, allowing us to directly simulate up to $\sim 10^6$ particles. A larger number of particles can be simulated only using numerical techniques that approximate the contribution of distant bodies. Fig. 2.3 shows the evolution of the number of the simulated particles in the last 50 years, scaling accordingly to the Moore's law.

2.5.2 N-body methods

A N-body code is a code that follows the motion of a large number of masses under their mutual gravitational attraction (Binney and Tremaine, 2008). There are two different types of N-body calculations depending on whether the system is collisional or collisionless. I will mainly focus on collisional systems.

In direct summation N-body codes, used to evolve collisional systems, each particle in the simulation may correspond to a particle of the real physical system under study (e.g. a star in a young star cluster). Other codes integrate the equation of motion of particles representing bunches of real particles. Tree codes, for example, arrange particles in a tree and approximate distant groups of particles with their total mass and their baricenter. The size of the cell used for this approximation is determined according to an accuracy parameter. This approach drastically reduces the number of force evaluations at a cost of larger errors. This may be not a problem in simulating collisionless systems while is not convenient for collisional ones.

The common base of all the N-body codes is that given the initial positions and velocities of the particles (initial conditions), they compute the gravitational forces among them. These forces are then used to find the new positions and momenta of the particles. Then the loop starts again finding the new forces.

Given the nature of collisional systems, the gravitational forces are calculated by direct summation.

This means that the force acting on a certain particle i is calculated by summing the contribution of all the other particles:

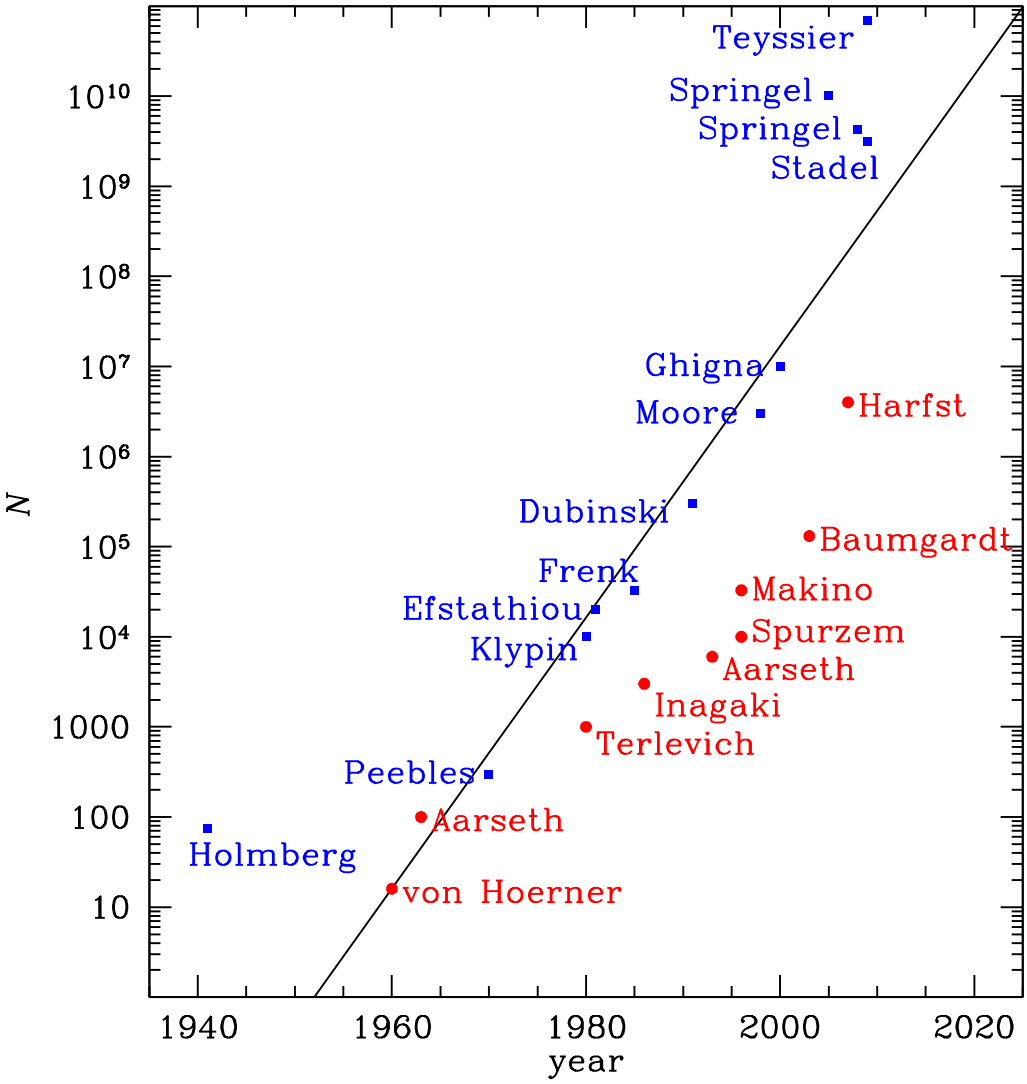

Figure 2.3: The increase in particle number over the past 50 years for selected collisional (red) and collisionless (blue) N-body simulations. The line shows the scaling $N = N_0 2^{(\text{year}-y_0)/2}$ expected from Moore's law if the costs scale $\propto N$. (Dehnen and Read, 2011)

$$\mathbf{F}_i = \sum_{j \neq i} G \frac{m_i m_j}{r_{ij}} \hat{\mathbf{e}}_{r_{ij}} \tag{2.45}$$

The Hamiltonian H and the equations of motion are

$$H = \sum_i \frac{\mathbf{p}_i^2}{2m_i} - G \sum_i \sum_{j>i} \frac{m_i m_j}{|\mathbf{x}_i - \mathbf{x}|_j} \tag{2.46}$$

$$\mathbf{a}_i = \frac{\dot{\mathbf{p}}_i}{m_i} = -\frac{1}{m_i} \frac{\partial H}{\partial \mathbf{x}_i} = -G \sum_{j \neq i} m_i \frac{\mathbf{x}_i - \mathbf{x}_j}{|\mathbf{x}_i - \mathbf{x}_j|^3} \tag{2.47}$$

where $\mathbf{p}_i = m\dot{\mathbf{x}}_i$ is the momentum, $\mathbf{x}_i$ is the position and $\mathbf{a}_i = \ddot{x}_i$ is the acceleration of the particle i.

The computational cost is proportional to $N(N-1)/2$. If the N-body code is coupled to other tools (for example a stellar evolution code) it can be even slower.

To speed up the computations different approaches were explored, even the creation of on-purpose hardware devoted to gravitational force computations, such as GRAPE (GRAvity PipE, Makino et al. (2003)).

Euler integrator

The simplest possible integrator for the N-body problem is the Euler integrator. It updates the position and the velocity of a given particle for a timestep Δt with

$$\mathbf{x}(t + \Delta t) = \mathbf{x} + \dot{\mathbf{x}} \Delta t \tag{2.48}$$

$$\dot{\mathbf{x}}(t + \Delta t) = \dot{\mathbf{x}} + \ddot{\mathbf{x}} \Delta t \tag{2.49}$$

This may seem correct but it behaves very poorly. Given that Δt cannot be infinitely small, in practice the Euler method is a first order Taylor expansion and the errors are proportional to Δt^2 (Dehnen and Read, 2011).

Leapfrog (Verlet) integrator

The leapfrog integrator is a symplectic integrator. Symplectic integrators solve exactly an (approximated) Hamiltonian

$$\tilde{H} = H + H_{\text{err}} \tag{2.50}$$

minimizing the error H_{err}.
A nice feature of symplectic integrators is being time reversible if the integration time step is fixed and constant for all the particles. Errors are stable over the time and energy is well-conserved.
Leapfrog is a second order integrator constructed by combining together two operations: kick and drift. The drift step is the simple Euler method. The kick step, on the other hand, is different because the new acceleration is calculated from the drifted position instead of the initial one. Because of its structure (a drift followed by a kick) is called modified Euler scheme.
The final equations are

$$\mathbf{x} = \mathbf{x}_0 + \dot{\mathbf{X}}_0 \Delta t + \frac{1}{2}\ddot{\mathbf{x}}_0 \Delta t^2 \tag{2.51}$$

$$\dot{\mathbf{x}}_1 = \dot{\mathbf{x}}_0 + \frac{1}{2}(\ddot{\mathbf{x}}_0 - \ddot{\mathbf{x}}_1)\Delta t \tag{2.52}$$

These equations are a second order Taylor expansion. It is, in principle, possible to combine many drift and kick steps to raise the scheme order, however problems in the integration raise making this approach not useful. Furthermore, a kick-drift-kick leapfrog scheme is also possible.

Hermite integrators

Being a second order integrator, leapfrog is not very suited for collisional systems, in which errors, even though stable in time, would make close encounter completely chaotic and the simulation meaningless. To obtain a result accurate enough, the timestep should be so short to lead to prohibitive simulation times. Thus, it is necessary a higher order class of integrators. Hermite schemes meet

this requirements. Hermite integrators are not symplectic, their errors accumulate during the integration. However they are very small thus allowing an accurate integration within a time short enough. See Fig. 2.4 for a comparison of the different algorithm errors. It can be seen that the leapfrog error is large but stable while the error for the Hermite scheme is small but accumulates in time. A fourth order Hermite scheme looks like:

$$\mathbf{x}_1 = \mathbf{x}_0 + \dot{\mathbf{x}}_0\Delta t + \frac{1}{2}\mathbf{a}_0\Delta t^2 + \frac{1}{6}\dot{\mathbf{a}}_0\Delta t^3 + \frac{1}{24}\ddot{\mathbf{a}}_0\Delta t^4 \tag{2.53}$$

$$\dot{\mathbf{x}}_1 = \dot{\mathbf{x}}_0 + \mathbf{a}_0\Delta t + \frac{1}{2}\dot{\mathbf{a}}_0\Delta t^2 + \frac{1}{6}\ddot{\mathbf{a}}_0\Delta t^3 + \frac{1}{24}\dddot{\mathbf{a}}_0\Delta t^4 \tag{2.54}$$

$$\mathbf{a}_1 = \mathbf{a}_0 + \dot{\mathbf{a}}_0\Delta t + \frac{1}{2}\ddot{\mathbf{a}}_0\Delta t^2 + \frac{1}{6}\dddot{\mathbf{a}}_0\Delta t^3 \tag{2.55}$$

$$\dot{\mathbf{a}}_1 = \dot{\mathbf{a}}_0 + \ddot{\mathbf{a}}_0\Delta t + \frac{1}{2}\dddot{\mathbf{a}}_0\Delta t^2 \tag{2.56}$$

Eliminating $\ddot{a}_0$ and $\dddot{a}_0$ leads to fourth order accurate time symmetric (but not symplectic) equations, with excellent energy conservation. Unfortunately, it results also in an implicit scheme. To overcome this issue, position and velocities are predicted, used to estimate the acceleration and the jerk and then corrected. This is a predict-evaluate-correct (PEC) scheme. Further iterations are noted as P(EC)^n where n is the number of iterations. In the limit $n \to \infty$ this method converges to the implicit one. The explicit PEC scheme is not time symmetric.

2.5.3 Timesteps

Finding the right timestep to advance the integration of the particle in a simulation is a critical point. The timestep should not be too short otherwise it would stop the simulation, but can not be too large because the errors would destroy the integration result. The timestep has to be related to the dynamical properties of the system and needs to evolve with them. Moreover, simulating a collisional system there will be particles interacting in some high density regions and close encounters, thus requiring very short timestep to provide an

accurate result. Other particles, on the contrary, would find themselves in low density-low interaction rate regions, where a longer timestep is fine and saves resources.

The early solutions used to assign an individual timestep to every particle. This is quite straightforward in direct summation codes, but not very convenient. Block timesteps work by collecting particles in sets, each with a certain timestep with duration $h \equiv \frac{h_0}{2^k}$ with $k = 1, 2, 3, \ldots, K$. h_0 is the largest timestep and h_K the smallest.

Determining the best timestep is a hard challenge. The first solutions were based on the evaluation of the potential. But the absolute value of the potential can change by a constant without changing the dynamics, thus this solution was not good.

Further criteria were adopted involving the acceleration and its derivatives, as the one proposed by Aarseth (2003):

$$\Delta t_i = \left(\eta \frac{|\mathbf{a}_i||\ddot{\mathbf{a}}_i| + |\dot{\mathbf{a}}_i|^2}{|\dot{\mathbf{a}}_i||\dddot{\mathbf{a}}_i| + |\ddot{\mathbf{a}}_i|^2} \right)^{1/2} \tag{2.57}$$

where η is an arbitrary constant accuracy parameter (values of $\eta \leq 0.02$ are commonly used).

2.5.4 Regularization

Let us consider the equation of motion of two particles attracting each other by gravity. If they are on a radial trajectory, then only radial components are non zero, the equation of motion is

$$\ddot{r} = -\frac{G(m_1 + m_2)}{r^2} \tag{2.58}$$

The equation is singular in $r = 0$, resulting in $\ddot{r} \to \infty$.

A good integrator with adaptive or block timesteps would treat this divergence by reducing this timestep until the simulation stops. Even in the case of an orbit with not completely zero but with small impact parameter, the slowdown could be drastic. The solution is to operate a change of coordinates so that the

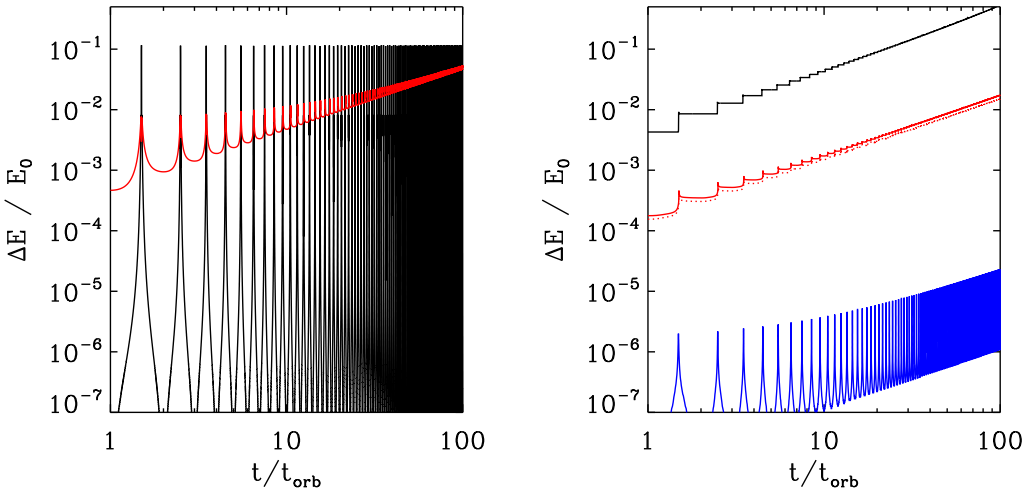

Figure 2.4: **Left:** Fractional change in energy for the Kepler problem for the leapfrog integrator with fixed timesteps (black), variable timesteps (equation (2.57) red). **Right:** Fractional change in energy for the Kepler problem for the 4th order Hermite integrator with fixed timesteps (black) variable timesteps (equation (2.57); red). The blue curve shows the energy error for the same Kepler orbit calculated using the K-S regularized equations of motion (see text for details). All calculations with variable timesteps were run at the same computational cost (~ 250 force and jerk evaluations per orbit, which is about a quarter of the cost of the fixed-timestep calculations). (Dehnen and Read, 2011)

system is no longer singular. This operation is called regularization (Mikkola, 1997, Heggie and Hut, 2003, Aarseth, 2003.

There are different ways to regularize a system, each one with its advantages and disadvantages.

Burdet-Heggie regularization

The simplest regularization is a time transformation. The equations of motion for the two body problem are

$$\ddot{\mathbf{r}} = -GM\frac{\hat{\mathbf{e}}_r}{r^2} + \mathbf{g} \tag{2.59}$$

where $\hat{\mathbf{e}}_r$ is the radial unity vector (versor) and $\mathbf{g}$ is the gravitational field from the other $N-2$ particles in the simulations. We then change the time from t to τ, defined by

$$\mathrm{d}t = r\,\mathrm{d}\tau \tag{2.60}$$

Then we find (derivative respect to τ denoted by a prime):

$$\dot{\mathbf{r}} = \frac{\mathrm{d}\tau}{\mathrm{d}t}\frac{\mathrm{d}\mathbf{r}}{\mathrm{d}\tau} = \frac{1}{r}\mathbf{r}' \tag{2.61}$$

$$\ddot{\mathbf{r}} = \frac{\mathrm{d}\tau}{\mathrm{d}t}\frac{1}{\mathrm{d}\tau}\frac{1}{r}\mathbf{r}' = \frac{1}{r^2}\mathbf{r}'' - \frac{r'}{r^3}\mathbf{r}' \tag{2.62}$$

The equation of motion than becomes

$$\mathbf{r}'' = \frac{r'}{r}\mathbf{r}' - G(m_1+m_2)\frac{\mathbf{r}}{r} + r^2\mathbf{g} \tag{2.63}$$

By the use of the eccentricity vector

$$\mathbf{e} = \mathbf{v}\times(\mathbf{r}\times\mathbf{v}) - GM\hat{e}_r \tag{2.64}$$

$$= (\mathbf{v}\cdot\mathbf{v})\mathbf{r} - (\mathbf{v}\cdot\mathbf{r})\mathbf{v} - GM\hat{e}_r \tag{2.65}$$

$$= \left|\mathbf{r}'\right|^2\frac{\mathbf{r}}{r^2} - \frac{r'}{r}\mathbf{r}' - GM\frac{\mathbf{r}}{r} \tag{2.66}$$

with $\mathbf{v} = \dot{\mathbf{r}} = \mathbf{r}'/r$.
The equation of motion simplifies to

$$\mathbf{r}'' = \left|\mathbf{r}'\right|^2\frac{\mathbf{r}}{r^2} - 2GM\frac{\mathbf{r}}{r} - \mathbf{e} + r^2\mathbf{g} \tag{2.67}$$

Given that the energy of the two-body orbit is

$$E_{2\mathrm{bd}} = \frac{1}{2}v^2 - \frac{G(m_1+m_2)}{r} = \frac{\left|\mathbf{r}'\right|^2}{2r^2} - \frac{G(m_1+m_2)}{r} \tag{2.68}$$

we obtain the regularized equation of motion

$$\mathbf{r}'' - 2E_{2\mathrm{bd}}\mathbf{r} = -e + 2r^2\mathbf{g} \tag{2.69}$$

We consider also the equations that express the change of $E_{2\mathrm{bd}}$, $\mathbf{e}$ and t as a function of τ:

$$\frac{\mathrm{d}E_{2\mathrm{bd}}}{\mathrm{d}\tau} = \mathbf{g}\cdot\frac{\mathbf{r}}{\mathrm{d}\tau} \tag{2.70}$$

$$\frac{\mathrm{d}\mathbf{e}}{\mathrm{d}\tau} = 2\mathbf{r}(\frac{\mathbf{r}}{\mathrm{d}\tau}\cdot\mathbf{g}) - \frac{\mathbf{r}}{\mathrm{d}\tau}(\mathbf{r}\cdot\mathbf{g}) - \mathbf{g}(\mathbf{r}\cdot\frac{\mathbf{r}}{\mathrm{d}\tau}) \tag{2.71}$$

$$\frac{t'}{\mathrm{d}\tau} = r \tag{2.72}$$

If $\mathbf{g} = 0$, E_{02} and $\mathbf{g}$ are constant and the equation of motion is that of a harmonic oscillator subject to the constant force $-\mathbf{e}$ (and the time τ is proportional to the eccentric anomaly).

Kustaanheimo-Stiefel (KS)

The use of spinors, quaternions and symmetries in the Kepler problem allows us to derive an alternative scheme for regularization (Stiefel, 1971, Yoshida, 1982, Heggie and Hut, 2003).
This scheme involves transforming the spatial coordinates together with the time. We define τ as before, and a four-vector $\mathbf{u} = (u_1, u_2, u_3, u_4)$ that can be obtained from the position with

$$u_1^2 = \frac{1}{2}(x+r)\cos^2\psi \tag{2.73}$$

$$u_2 = \frac{yu_1 + zU_4}{x+r} \tag{2.74}$$

$$u_3 = \frac{zu_1 - yU_4}{x+r} \tag{2.75}$$

$$u_4^2 = \frac{1}{2}(x+r)\sin^2\psi \tag{2.76}$$

$$\tag{2.77}$$

where ψ is an arbitrary parameter.
The old coordinates can be found from the new ones as

$$x = u_1^2 - u_2^2 - u_3^2 + u_4^2 \tag{2.78}$$

$$y = 2(u_1 u_2 - u_3 u_4) \tag{2.79}$$

$$z = 2(u_1 u_3 + u_2 u_4) \tag{2.80}$$

and

$$r = u_1^2 + u_2^2 + u_3^2 + u_4^2 \tag{2.81}$$

If Φ_e is the potential that generates $\mathbf{g}$ through $\mathbf{g} = -\nabla\Phi_e$, we obtain

$$\mathbf{u}'' - \frac{1}{2}E\mathbf{u} = -\frac{1}{4}\frac{\partial}{\partial \mathbf{u}}\left(|\mathbf{u}|^2 \Phi_e\right) \tag{2.82}$$

$$E = \frac{1}{2}v^2 - \frac{GM}{r} + \Phi_e = 2\frac{\left|\mathbf{u}'\right|^2}{|\mathbf{u}|^2} - \frac{GM}{|\mathbf{u}|^2} + \Phi_e \tag{2.83}$$

$$E' = |\mathbf{u}|^2 \frac{\partial \Phi_e}{\partial t} \tag{2.84}$$

$$\tag{2.85}$$

When $\mathbf{g} = 0$ the first equation corresponds to a four-dimensional harmonic oscillator.
With this scheme, the energy error is an order of magnitude smaller that that of the Burdet-Heggie regularization, with the same integrator.

The chain and the Mikkola's algorithmic regularizations

The previous regularization methods are based on a close two-body systems, thus they are not useful in situations involving more than two bodies, e.g. two close binaries interacting. The chain treatment (Mikkola and Aarseth, 1993) provides a method to regularize systems with more than two bodies.
The chain algorithm proceeds as follows:

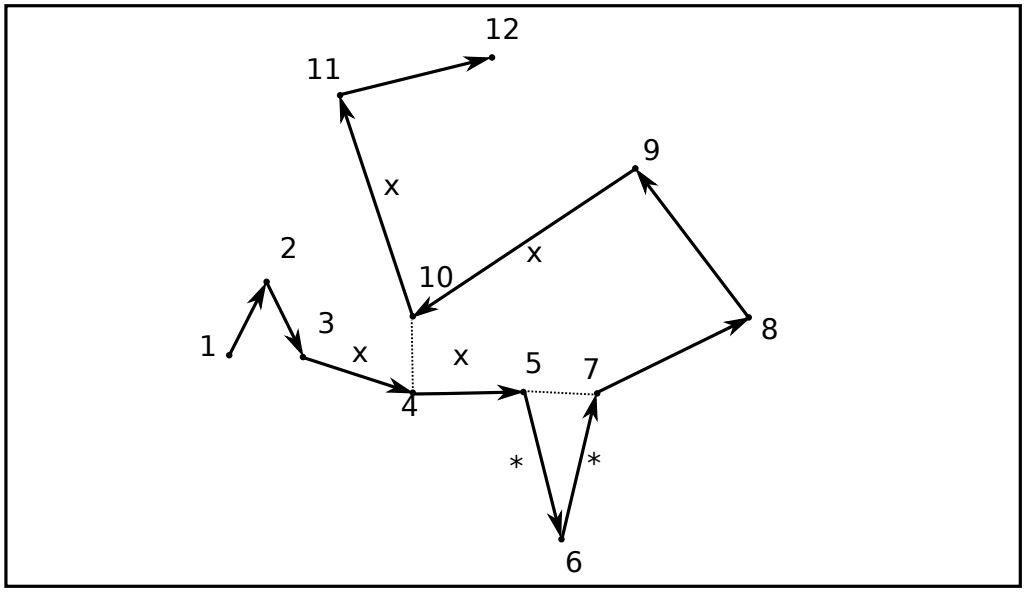

Figure 2.5: Scheme of a chain. Distances $R_{5,7}$ and $R_{4,10}$ are compared with the (longer) distances adopted in building the chain (marked by "*" and "x" respectively (Mikkola and Aarseth, 1993).

- find the shortest distance among all the particles, this is the first element of the chain (see Fig. 2.5)
- choose one end of this segment and proceed building the chain attaching the nearest particle
- once the chain is completed (i.e. all the particles are inserted), apply the KS regularization to each pair in the chain

Note that it is not guarantee that all the segments represents the shortest distance among particles. The chain regularization not only solves the problem of diverging forces among close particles, but also provide a reduction of the round-off errors keeping the numerical values of the distances smaller.
An alternative to the chain regularization is the the Mikkola's algorithmic regularization. This method is based on a time-only transformation coupled to a leapfrog algorithm. It produces exact trajectories for two-body motion and reg-

ular results when integrating strongly interacting few-body systems. However, algorithm regularization alone is not sufficiently accurate, thus the extrapolation method is used for improved precision. The extrapolation method requires a time-symmetric leapfrog, which is not possible for velocity-dependent forces. To overcome this issue, usually an implicit mid-point method is adopted. Mikkola and Merritt (2006) and Mikkola and Merritt (2008) proposed an alternative explicit algorithmic regularization algorithm that uses a generalized mid-point method to obtain the required time symmetry, eliminating the need for the implicit mid-point method and allowing the use of extrapolation.

CHAPTER 3

DYNAMICS OF STELLAR BLACK HOLES IN YOUNG STAR CLUSTERS WITH DIFFERENT METALLICITIES - II. BLACK HOLE-BLACK HOLE BINARIES

This chapter is based on Ziosi et al. (2014). In this paper, we study the formation and dynamical evolution of black hole-black hole (BH-BH) binaries in young star clusters (YSCs), by means of N-body simulations. The simulations include metallicity-dependent recipes for stellar evolution and stellar winds, and have been run for three different metallicities ($Z = 0.01, 0.1$ and $1\ Z_{\odot}$). Following recent theoretical models of wind mass-loss and core-collapse supernovae, we assume that the mass of the stellar remnants depends on the metallicity of the progenitor stars. We find that BH-BH binaries form efficiently because of dynamical exchanges: in our simulations, we find about 10 times more BH-BH binaries than double neutron star binaries. The simulated BH-BH

binaries form earlier in metal-poor YSCs, which host more massive black holes (BHs) than in metal-rich YSCs. The simulated BH-BH binaries have very large chirp masses (up to 80 $M_\odot$), because the BH mass is assumed to depend on metallicity, and because BHs can grow in mass due to the merger with stars. The simulated BH-BH binaries span a wide range of orbital periods ($10^{-3} - 10^7$ yr), and only a small fraction of them (0.3 per cent) is expected to merge within a Hubble time. We discuss the estimated merger rate from our simulations and the implications for Advanced VIRGO and LIGO.

3.1 Introduction

Most stars are expected to form in young star clusters (YSCs, Carpenter 2000; Lada and Lada 2003; Porras et al. 2003). Like globular clusters (GCs), the densest YSCs are collisional systems: their two-body relaxation timescale is shorter than their lifetime, and they undergo intense dynamical evolution. On the other hand, YSCs are considerably different from GCs: the former have generally lower mass ($< 10^5$ $M_\odot$) and smaller size (half-mass radius $r_{\rm hm} \lesssim 1$ pc) than the latter (see e.g. Portegies Zwart, McMillan, and Gieles 2010, for a recent review). This explains why the central relaxation time of YSCs is $\sim 10 - 50$ Myr, orders of magnitude shorter than that of GCs (e.g. Portegies Zwart 2004). YSCs populate the disc of late-type galaxies, while GCs are spherically distributed in the host-galaxy halo. Finally, GCs are old ($\gtrsim 12$ Gyr) and long-lived systems, whereas YSCs are young and short lived: most of them dissolve in the disc of the host galaxy in $\leq 10^8$ yr (e.g. Kruijssen et al. 2011).

Thus, the stellar content of dissolved YSCs is expected to build up a considerable fraction of the field population of the host galaxy. This must be taken into account when modelling the evolution of binary stellar systems in the galactic field: a large fraction of these binaries likely formed in YSCs, and then evolved through intense dynamical interactions, before being ejected into the field after the disruption of the parent YSC. This scenario is important for the study of stellar black hole (BH) binaries. In Mapelli et al. (2012, hereafter Paper I), we

studied the formation and the dynamical evolution of accreting BH binaries in YSCs. We found that dynamical interactions in YSCs have a significant impact on the expected population of X-ray sources powered by BHs.

In the current paper, we study the formation and the dynamical evolution of black hole-black hole (BH-BH) binaries in YSCs. For the sake of completeness, we will compare the evolution of BH-BH binaries with that of neutron star-neutron star (NS-NS) binaries and with that of binaries composed of a BH and a neutron star (NS) in YSCs. BH-BH, NS-NS and NS-BH binaries are among the most promising sources of gravitational waves (GWs) detectable by ground-based detectors (e.g. Peters 1964; Abramovici et al. 1992). Understanding the demographics of such double compact object binaries (DCOBs) is particularly important in light of the forthcoming second-generation ground-based GW detectors, Advanced LIGO and VIRGO (Harry and the LIGO Scientific Collaboration, 2010; Acernese and The Virgo Collaboration, 2009; Accadia and The Virgo Collaboration, 2012).

The dynamics of YSCs can influence the formation and evolution of BH-BH binaries in three different ways: (i) dynamical friction causes the BHs (which are more massive than most stars) to sink to the denser YSC core, where they have a higher probability to interact with other BHs (e.g. Sigurdsson and Hernquist, 1993); (ii) three-body encounters (i.e. close encounters between a binary and a single star) change the binary orbital properties: if the binary is hard (i.e. if its binding energy is higher than the average kinetic energy of a star in the cluster[1]), three-body encounters tend to shrink the binary semi-major axis (Heggie, 1975); (iii) dynamical exchanges (i.e. three-body interactions in which one of the members of the binary is replaced by the single star) enhance the

[1]A binary can be classified as hard if its binding energy is higher than the average kinetic energy of stars in the cluster, that is

$$\frac{G\,m_1\,m_2}{2\,a} \gtrsim \frac{1}{2}\langle m\rangle\sigma^2, \tag{3.1}$$

where G is the gravitational constant, m_1 and m_2 are the mass of the primary member and the mass of the secondary member of the binary, respectively, while $\langle m\rangle$ and σ are the average mass and velocity dispersion of a star in the star cluster.

formation of BH-BH binaries. In fact, the probability for a single star with mass m_3 to replace a binary member is higher if $m_3 \geq m_1$ or $m_3 \geq m_2$ (where m_1 and m_2 are the masses of the former binary members, see Hills 1989 and Hills 1992). As BHs are more massive than most stars, they efficiently acquire companions through dynamical exchanges.
Previous studies investigated the formation and evolution of DCOBs either in GCs, via Monte Carlo codes (e.g. O'Leary et al. 2006; Sadowski et al. 2008; Downing et al. 2010; Downing et al. 2011; Clausen, Sigurdsson, and Chernoff 2013), or in the field, using population synthesis simulations of isolated binaries (e.g. Belczynski, Kalogera, and Bulik 2002; Voss and Tauris 2003; Pfahl, Podsiadlowski, and Rappaport 2005; Dewi, Podsiadlowski, and Sena 2006; Belczynski et al. 2007; Belczynski et al. 2010b; Dominik et al. 2012). Our study provides a new perspective on this subject: we study the formation of BH-BH binaries in YSCs, by using direct N-body simulations coupled with up-to-date stellar and binary evolution recipes. The paper is organized as follows. In Section 3.2, we briefly describe our simulations. In Section 3.3, we present our results. Section 3.4 is devoted to discuss the results and to compare them with previous work. Our conclusions are presented in Section 3.6.

3.2 Methods and simulations

The simulations analyzed in this paper adopt the same technique as described in paper I. In particular, we used a modified version of the STARLAB public software environment (see Portegies Zwart et al. 2001). Our upgraded version of STARLAB includes (i) analytic formulae for stellar evolution as a function of mass and metallicity (Hurley, Pols, and Tout, 2000), (ii) metallicity-dependent stellar winds for main sequence (Vink, de Koter, and Lamers, 2001) and evolved stars (Vink and de Koter, 2005), and (iii) the possibility that massive BHs form by direct collapse, i.e. with a weak or no supernova (SN) explosion (e.g. Fryer 1999; Fryer and Kalogera 2001; Mapelli, Colpi, and Zampieri 2009; Belczynski et al. 2010a; Fryer et al. 2012).

Table 3.1: Summary of initial YSC properties

Parameter	Value
W_0	5
N_*	5500
r_c (pc)	0.4
$c \equiv \log_{10}(r_t/r_c)$	1.03
IMF	Kroupa (2001)
m_{min} ($M_\odot$)	0.1
m_{max} ($M_\odot$)	150
Z ($Z_\odot$)	0.01, 0.1, 1
t_{max} (Myr)	100
f_{PB}	0.1

W_0: central dimensionless potential in the King (1966) model; N_*: number of stars per YSC; r_c: initial core radius; $c \equiv \log_{10}(r_t/r_c)$: concentration ($r_t$ is the initial tidal radius); IMF: initial mass function; m_{min} and m_{max}: minimum and maximum simulated stellar mass, respectively; Z: metallicity of the YSC (in our simulations, we assume $Z_\odot = 0.019$); t_{max}: duration of each simulation (in Myr); f_{PB}: fraction of PBs, defined as the number of PBs in each YSC divided by the number of 'centers of mass' (CMs) in the YSC. In each simulated YSC, there are initially 5000 CMs, among which 500 are designated as 'binaries' and 4500 are 'single stars' (see Downing et al. 2010 for a description of this formalism). Thus, 1000 stars per YSC are initially in binaries.

According to these recipes, if the final mass of the progenitor star (i.e. the mass before the collapse), is > 40 $M_\odot$, we assume that the SN fails and that the star collapses quietly to a BH. As the final mass of a massive star is higher at low metallicity, because of the weaker stellar winds, BH masses are allowed to be higher at low metallicity. In particular, the BH mass depends on the metallicity and on the zero age main sequence (ZAMS) mass of the progenitor as described in Fig. 1 of paper I. In this scenario, BHs with mass up to ~ 80 $M_\odot$ (~ 40 $M_\odot$) can form if the metallicity of the progenitor is $Z \sim 0.01\ Z_\odot$ ($Z \sim 0.1\ Z_\odot$). The maximum BH mass at $Z \sim Z_\odot$ is 23 $M_\odot$. This is higher than assumed in previous studies (e.g. Belczynski et al. 2010a), but is still consistent with the observations, given the large uncertainties (e.g. Özel et al. 2010).

NSs and BHs that form from a SN explosion receive a natal kick in a random

direction. The natal kick of NSs is chosen randomly from the distribution $P(u) = (4/\pi)\,(1+u^2)^{-2}$, where $u = v/\tilde{v}$, v is the modulus of the velocity vector of the NS and $\tilde{v} = 600$ km s^{-1} (Hartman, 1997; Portegies Zwart et al., 2001). The natal kick of BHs is drawn from the same distribution, but is normalized by a factor $f_{\rm kick} = m_{\rm NS}/m_{\rm BH}$ (where $m_{\rm BH}$ is the BH mass and $m_{\rm NS} = 1.3\,{\rm M}_\odot$ is the typical NS mass). Instead, BHs that form from quiet collapse are assumed to receive no natal kick (see Fryer et al. 2012).

Furthermore, STARLAB includes recipes for binary evolution, such as mass transfer (via wind accretion and via Roche lobe overflow), tidal circularization, magnetic braking, and also orbital decay and circularization by GW emission (see Portegies Zwart and Verbunt 1996; Portegies Zwart et al. 2001).

We doubled the simulation sample with respect to paper I: we have 600 N-body realizations of YSCs (1/3 of them with solar metallicity, 1/3 with metallicity $Z = 0.1\,{\rm Z}_\odot$, and the remaining 1/3 with $Z = 0.01\,{\rm Z}_\odot$). Half of the simulations were already presented in paper I, whereas the remaining are new simulations.

The simulated YSCs are initially modelled with 5000 centers of mass (single stars or binaries), following a King profile with central dimensionless potential $W_0 = 5$. The core density at the beginning of the simulation is $\rho_{\rm C} \sim 2\times10^3\,{\rm M}_\odot{\rm pc}^{-3}$. We chose a primordial binary fraction of $f_{\rm PB} = 0.1$ so the total number of stars is $N_* = 5500$. The total mass of a single YSC is $M_{\rm TOT} \sim 3-4\times10^3\,{\rm M}_\odot$. The single stars and the primary stars (m_1) of the binaries follow a Kroupa initial mass function (IMF, Kroupa, 2001) with minimum and maximum mass equal to 0.1 and 150 ${\rm M}_\odot$, respectively. The masses of the secondaries (m_2) are generated according to a uniform distribution between $0.1\,m_1$ and m_1. The initial semi-major axis a of the binaries are drawn from a log-uniform distribution $f(a) \propto 1/a$ between ${\rm R}_\odot$ and $10^5\,{\rm R}_\odot$, for consistency with the observation of binaries in the Solar neighborhood (Kraicheva et al., 1978; Duquennoy and Mayor, 1991). Values of a leading to a periastron separation smaller than the sum of the radii of the two stars in the binary were discarded. We randomly select the initial eccentricity from a thermal distribution $f(e) = 2\,e$ in the range [0, 1] (Heggie, 1975).

The central relaxation timescale is (Portegies Zwart, 2004)

$$t_{\rm rlx} \sim 10\,{\rm Myr}\,(r_{\rm hm}/0.8\,{\rm pc})^{3/2}(M_{\rm TOT}/3500\,{\rm M}_{\odot})^{1/2} \tag{3.2}$$

where $r_{\rm hm}$ is the half-mass radius of the YSC ($\sim 0.8-0.9$ pc in our simulations). The core collapse timescale (Portegies Zwart and McMillan, 2002) is $t_{\rm cc} \sim 2\,{\rm Myr}(t_{\rm rlx}/10\,{\rm Myr})$.

A summary of the properties of the simulated YSCs is shown in Table 3.1. These were chosen to match the properties of the most common YSCs in our Galaxy.

Each YSC was simulated for 100 Myr: at later times the YSCs are expected to be disrupted by the galactic tidal field (e.g. Silva-Villa and Larsen 2010; Goddard, Bastian, and Kennicutt 2010; Gieles and Portegies Zwart 2011). We do not use recipes for the galactic tidal field but they will be included in future work. The structural evolution of our simulated YSCs is described in a companion paper (Mapelli and Bressan 2013). From Fig. 4 of Mapelli and Bressan 2013, it is apparent that the half-mass radius of the YSCs at 100 Myr is ~ 3 times the initial value. The average fraction of stars that are still bound to the YSC at 100 Myr is $0.85-0.9$. Thus, the simulated YSCs are expanding but most of them have not evaporated by the end of the simulation. This means that our results likely overestimate the number of dynamical exchanges and three-body encounters in the late stages of YSC life. We do not expect that this severely affects our predictions for the merger rate of BH-BH binaries, since the most intense dynamical activity of the YSCs occurs during (and immediately after) the core collapse (i.e. at $t \gtrsim 3$ Myr), because of the dramatic increase in the core density (by a factor of ≥ 10). In fact, most of the BH-BH binaries form in the first $\sim 3-40$ Myr (see the discussion in Section 3.3.1), and the BH-BH systems that are expected to merge in less than a Hubble time (and that are not disrupted before the end of the simulation, see Section 3.3.5) form at $4-7$ Myr. In a forthcoming paper, we will add different models for the galactic tidal field, and we will be able to quantify their impact on the BH-BH binary population.

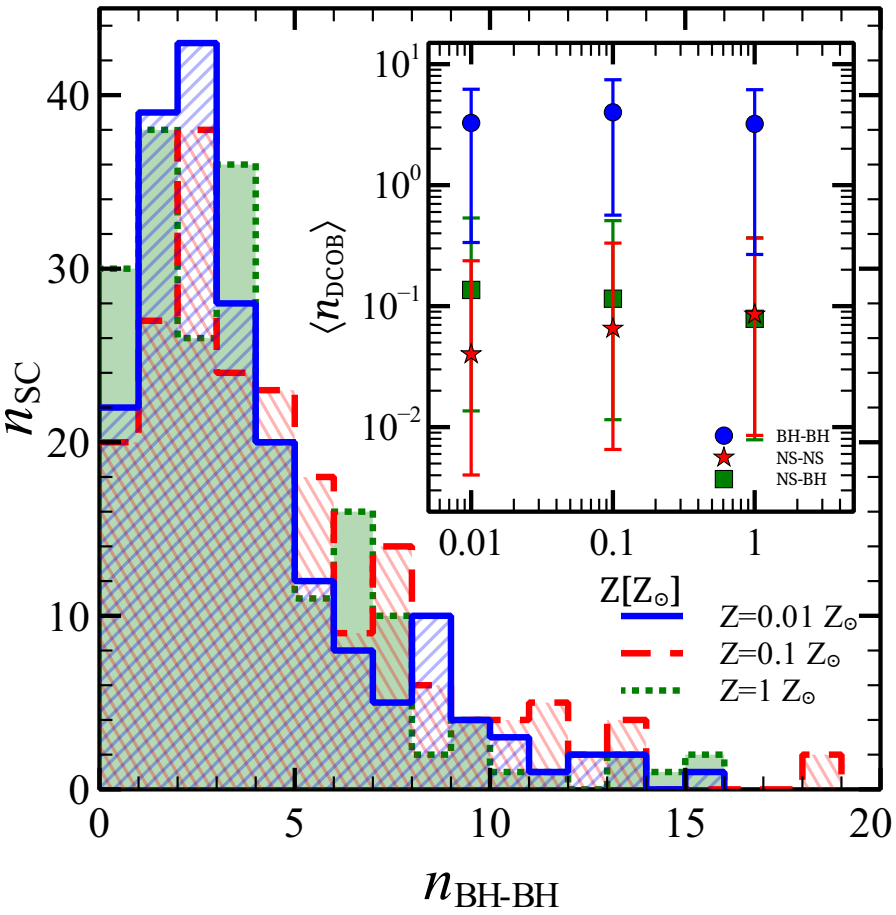

Figure 3.1: In the main panel, distribution of the number of BH-BH binaries per YSC per metallicity. The blue diagonally-hatched histogram refers to $Z = 0.01$ $Z_\odot$, the red diagonally-hatched histogram to $Z = 0.1 Z_\odot$ and the green filled histogram to $Z = Z_\odot$. In the inset, average number of BH-BH binaries (blue circles), NS-BH binaries (green squares) and NS-NS binaries (red stars) per YSC as a function of the YSC metallicity. The error bars are 1 σ deviations. All the quantities in this figure are integrated over the duration of the simulations (i.e. 100 Myr).

3.3 Results

3.3.1 DCOB population

The number of DCOBs formed in our simulations is summarized in Fig. 3.1. Here and in the following, unless otherwise specified, a binary is defined as a simulated bound pair (either existing in the initial conditions or formed during the evolution of the YSC, either hard or soft, either stable or unstable depending on the criterion adopted by STARLAB, see Portegies Zwart et al. 2001). In Appendix A, we discuss how our main results depend on this definition, by considering stable and unstable binaries separately. Furthermore, we classify a binary that forms from an exchange as a new binary with respect to the pre-exchange binary.

The inset of Fig. 3.1 shows that the simulated number of BH-BH binaries per YSC (integrated over 100 Myr) is a factor of $\sim 10-100$ higher than the simulated number of NS-NS binaries per YSC, regardless of the metallicity.

Due to the chosen IMF, our simulated YSCs host a number of NSs that is $3-4$ times higher than the number of BHs. Thus, the fact that BH-BH binaries are much more numerous than NS-NS binaries is a striking effect of dynamics. BHs are heavier and tend to sink to the center of the YSC on a timescale $t_{\rm seg} \sim t_{\rm rlx}\frac{\langle m\rangle}{M_{\rm BH}}$ (O'Leary et al., 2006). Thus, a 40 $M_\odot$ BH sinks towards the center in ~ 0.25 Myr. Once in the dense YSC center, BHs have a higher probability to interact with other BHs, forming BH-BH binaries. Furthermore, BHs are more massive than most stars in the simulation already at $t \sim 8$ Myr (when the turn-off mass is ~ 20 $M_\odot$). Thus, they are particularly efficient in acquiring companions through dynamical exchanges (Hills 1989; Hills 1992). In fact, most of our BH-BH binaries come from dynamical exchanges. Only ~ 1.7 per cent of BH-BH binaries come from primordial binaries. Moreover BHs have a weaker (if any) natal kick with respect to that of NSs. Therefore, they are more likely to remain in the denser regions of the YSC, rather than being ejected.

In contrast, a large fraction of NSs (up to 90 per cent at $t = 100$ Myr) is ejected from the parent YSC as a consequence of natal kicks or dynamical recoil. The

few NSs that remain in the YSCs are much lighter than BHs, and thus the probability that they acquire a second NS companion by dynamical exchanges is low. This is confirmed by the fact that 87 per cent of all the NS-NS binaries come from primordial binaries.

The main panel of Fig. 3.1 shows the distribution of the number of BH-BH binaries per YSC per metallicity, integrated over the simulation time ($t_{\rm max}$ = 100 Myr). It follows a Poissonian distribution and peaks between 2 and 4 BH-BH binaries per YSC, in agreement with the average values shown in the inset of the same figure. Approximately $10-15$ per cent of YSCs do not host any BH-BH binary. The simulated YSC with the largest number of BH-BH binaries hosts 18 BH-BH binaries.

We find no statistically significant differences between YSCs with different metallicity, when looking at the number of BH-BH binaries integrated over time (Fig. 3.1). In contrast, we do find differences when we look at the number of BH-BH binaries as a function of time. In particular, the lower the metallicity is, the shorter the time needed to build the distribution of BH-BH binaries (Fig. 3.2).

Furthermore, while in the inset of Fig. 3.1 the average number of BH-BH binaries per YSC (integrated over time) at $Z = 0.1$ Z$_\odot$ is slightly larger than that at $Z = 0.01$ Z$_\odot$, in Fig. 3.2 the number of BH-BH binaries as a function of time at $Z = 0.01$ Z$_\odot$ is always higher than that at $Z = 0.1$ Z$_\odot$. This result might appear puzzling: the number of BH-BH binaries per YSC integrated over time is larger at $Z = 0.1$ Z$_\odot$ than at $Z = 0.01$ Z$_\odot$, while the number of BH-BH binaries per YSC at a given time is larger at $Z = 0.01$ Z$_\odot$ than at $Z = 0.1$ Z$_\odot$. Actually, this is a consequence of the fact that BHs are more massive at low metallicity, and thus are more efficient in acquiring companions through dynamical exchanges and in producing stable binaries with longer lifetimes. This implies that the BH-BH binaries which form at $Z = 0.01$ Z$_\odot$ are less numerous than those which form at $Z = 0.1, 1$ Z$_\odot$ but they live for a much longer time (before being ionized or exchanged) than the latter (see Fig. 3.3 and the comments in next section). Thus, if we look at a YSC at a given time, we find more BH-BH binaries at

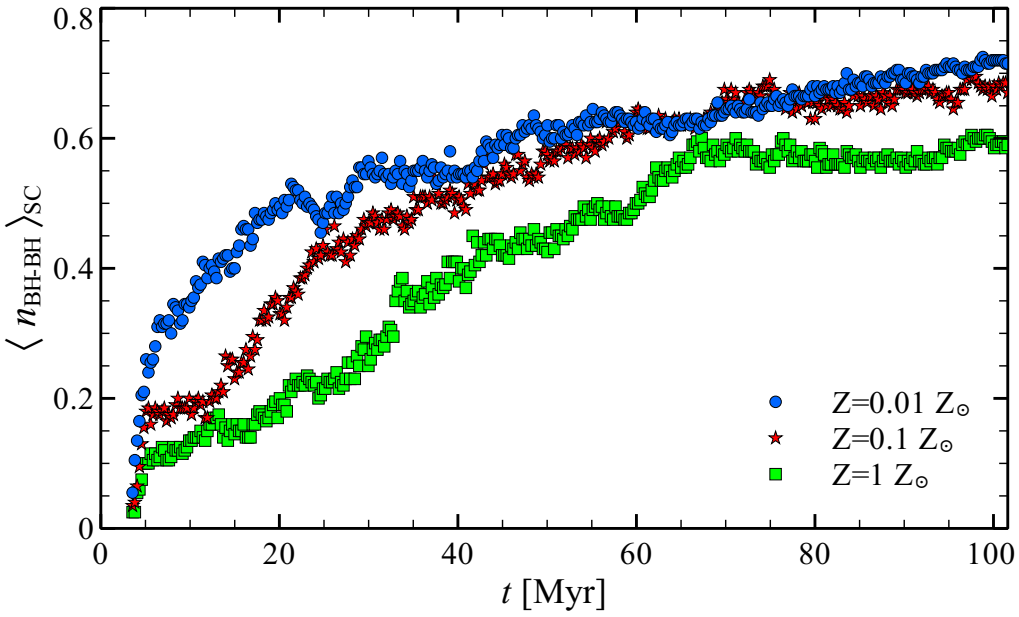

Figure 3.2: Average number of BH-BH binaries as a function of time for the three different metallicities. Blue circles: $Z = 0.01$ Z$_\odot$; red stars: $Z = 0.1$ Z$_\odot$; green squares $Z = 1$ Z$_\odot$.

$Z = 0.01$ Z$_\odot$ than at $Z = 0.1, 1$ Z$_\odot$.

Finally, we notice that the first BH-BH binaries form at $t \sim 3$ Myr, i.e. the time of core collapse, regardless of the metallicity. This is a consequence of the fact that binary hardening becomes important during the core collapse and drives the re-expansion of the core (Mapelli and Bressan, 2013).

3.3.2 Lifetimes and exchanges

In section 3.3.1, we showed that metal-poor YSCs build up their BH-BH binary population earlier than metal-rich ones. Furthermore, the BH-BH binaries that form in metal-poor YSCs ($Z = 0.01$ Z$_\odot$) are more stable, i.e. have longer lifetimes (before they break up or undergo another exchange). This is a consequence of the higher BH masses allowed in the failed SN scenario. In Fig. 3.3, we show the cumulative distribution of BH-BH binary lifetimes. At $Z = 0.1, 1$ Z$_\odot$ 90 per

cent of BH-BH binaries survive for less than 20 Myr, while at $Z = 0.01$ $Z_\odot$ 90 per cent of BH-BH binaries survive up to 40 Myr. Furthermore, about 5 per cent of BH-BH binaries survive for more than 80 Myr in the YSCs with $Z = 0.01$ $Z_\odot$, while only 1–2 per cent of BH-BH binaries survive for more than 80 Myr in the YSCs with $Z \geq 0.1\,Z_\odot$.

We have also run a Kolmogorov-Smirnov (KS) test on the distributions presented in Fig. 3.3. We find a probability $P_{\rm KS} = 4.05 \times 10^{-8}$ that BH-BH binary lifetimes at $Z = 0.01$ $Z_\odot$ and at $Z = 0.1$ $Z_\odot$ are drawn from the same distribution. Similarly, $P_{\rm KS} = 5.46 \times 10^{-2}$ when comparing BH-BH binary lifetimes at $Z = 0.01$ $Z_\odot$ and $Z = Z_\odot$, and $P_{\rm KS} = 3.14 \times 10^{-6}$ when comparing BH-BH binary lifetimes at $Z = 0.1$ $Z_\odot$ and $Z = Z_\odot$. This result confirms that the three distributions are statistically different.

We notice that the average number of exchanges is quite the same across different metallicities in Table 3.2. Thus, the difference in lifetimes must be interpreted as a higher probability of binary break up (i.e. ionization) in case of high metallicity. Also, from Table 3.2 we notice that the few survived NS-NS binaries are very stable, as they undergo a low number of exchanges.

Fig. 3.4 summarizes the possible pathways that lead to the formation of a BH-BH binary and their relative importance in our simulations. BH-BH binaries can derive from either a primordial binary or an exchange. The upper branch of the scheme shows that 36 simulated BH-BH binaries are primordial binaries, while 63 simulated BH-BH binaries form through a dynamical exchange in which a single BH replaces a star in a BH-star binary (in Fig. 3.4, these systems are called '1-exchange' BH-BH binaries).

In the subsequent evolution, BH-BH binaries born from primordial binaries can either be ionized by a three-body encounter, or undergo an exchange. If the primordial binary undergoes an exchange and if the intruder is a BH, the BH-BH binary becomes an exchanged BH-BH binary. Considering the entire set of simulations for 100 Myr, the total number of BH-BH binaries formed is 2096.

At the end of the simulations (i.e. after 100 Myr) the BH-BH binaries that still

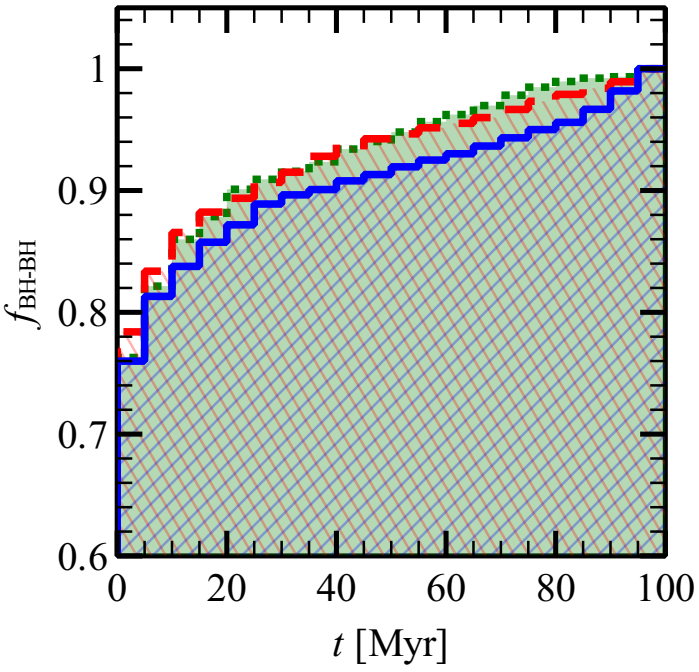

Figure 3.3: Cumulative distribution of BH-BH binary lifetimes (normalized to the total number of BH-BH binaries per each metallicity). Blue diagonally-hatched histogram: $Z = 0.01$ Z$_\odot$; red diagonally-hatched histogram: $Z = 0.1$ Z$_\odot$; green filled histogram: $Z =$ Z$_\odot$.

survive are 31 primordial binaries and 364 exchanged binaries, for a total of 395 BH-BH binaries (0.66 BH-BH binaries per YSC, on average).

Thus, in summary, 1.7 per cent of all BH-BH binaries in our simulations are primordial binaries, while the remaining 97.3 per cent are exchanged binaries.

3.3.3 Orbital properties

In Fig. 3.5, the distributions of the orbital properties of the BH-BH, NS-NS and NS-BH binaries are shown. These are measured at the time in which the semi-major axis a is minimum for each binary. The metallicity does not significantly affect the distribution of semi-major axes and eccentricities of BH-BH binaries.

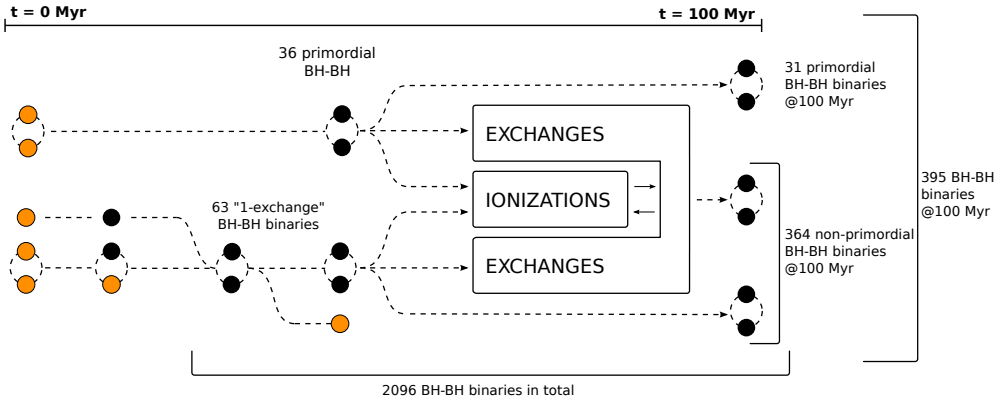

Figure 3.4: Schematic representation of the main formation and evolution pathways of BH-BH binaries in our simulations. Yellow circles: stars; black circles: black holes. In the top row, from left to right: primordial binaries can evolve into BH-BH binaries by stellar evolution. Then, primordial BH-BH binaries can be ionized or undergo an exchange and become exchanged BH-BH binaries. In the bottom row, from left to right: we call '1-exchange' binaries those BH-BH binaries that form after the exchange of a BH into a BH-star binary. In the following, '1-exchange' binaries can either be ionized or undergo more exchanges. For the sake of simplicity, we call ionizations also the exchanges that transform a BH-BH binary into a BH-star binary. The members of a ionized BH-BH binary can enter a BH-BH binary again via three-body exchange.

Table 3.2: Average number of exchanges per metallicity per DCOB type. Values outside (within parenthesis) refer to all DCOBs (only DCOBs that are considered 'stable' according to the criterion defined in STARLAB, see Portegies Zwart et al. 2001 and our Appendix A).

Type	0.01 $Z_\odot$	0.1 $Z_\odot$	$Z_\odot$
BH-BH	9.92 (0.41)	9.91 (0.48)	10.14 (0.58)
NS-NS	0.00 (0.00)	0.50 (0.15)	0.26 (0.09)
NS-BH	6.33 (0.49)	3.72 (0.48)	3.48 (0.43)

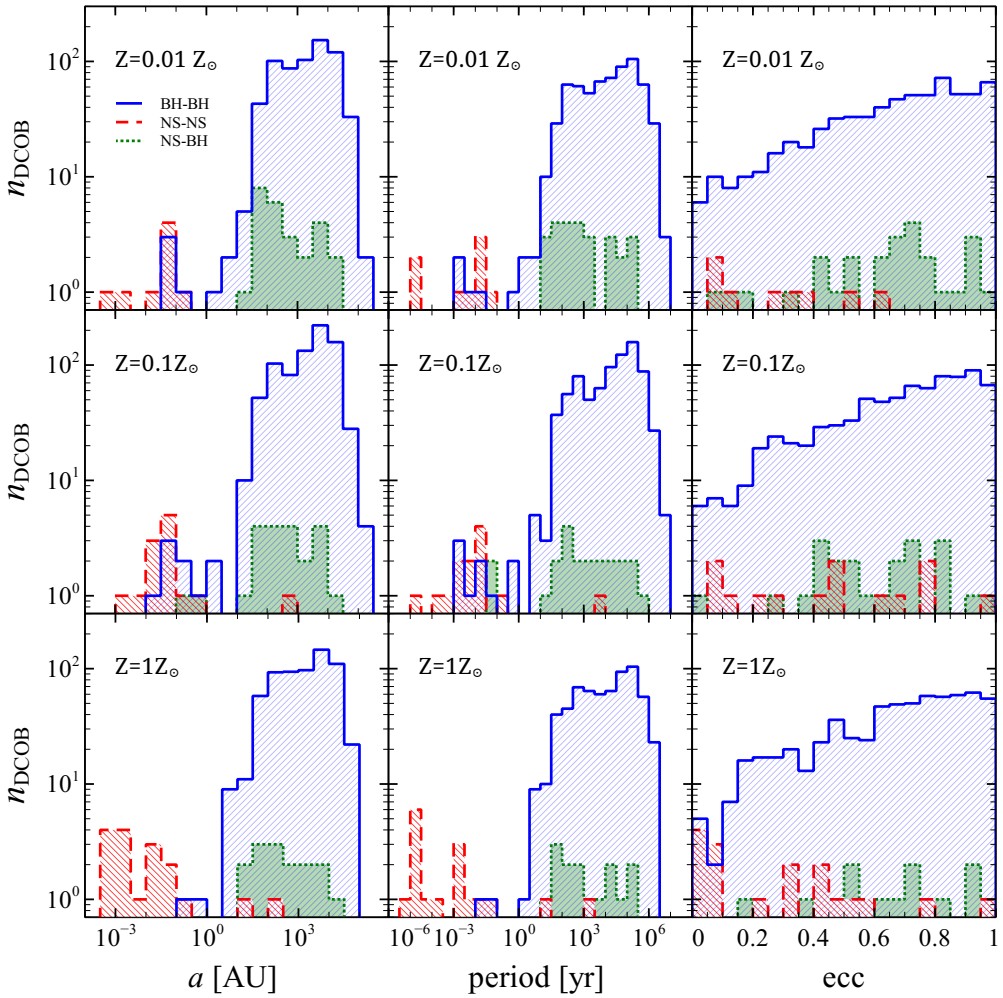

Figure 3.5: Histograms of the orbital properties of DCOBs measured, for each binary, when the semi-major axis a is minimum. Columns from left to right refer to semi-major axis a, period and eccentricity of the binary. Rows from top to bottom refer to three different metallicities: $Z = 0.01$, 0.1 and $1\,Z_\odot$. The blue, red and green histograms refer to BH-BH, NS-NS and NS-BH binaries, respectively.

The eccentricity distribution of BH-BH binaries follows the initial equilibrium distribution $f(e) \propto 2e$, but with an excess of low-eccentricity systems coming from the circularization by tidal forces (which influenced some systems before both components collapsed) and by GW emission.
BH-BH binaries span a wide range in both semi-major axes and orbital periods ($10^{-2} - 10^{6}$ AU and $10^{-3} - 10^{7}$ yr, respectively).
We notice a strong break in the distribution of semi-major axes of BH-BH binaries at ~ 1 AU. This is consistent with the fact that the most massive primordial binaries with separation $a \lesssim 1$ AU merged before the formation of BHs, emptying the region of BH-BH binaries with that semi-major axis. Only dynamical effects can populate this region, but they do it slowly, because the hardening time (i.e. the timescale for hardening a binary by three-body encounters) scales as a^{-2} (see e.g. Quinlan 1996).
We notice that the softest binaries in Fig. 3.5 have semi-major axis as large as ~ 5 pc, close to the initial tidal radius of the YSC. These extremely loose bound pairs are highly unstable (see the discussion in the appendix) and very short-lived: it is reasonable to expect that they would completely disappear, if a galactic tidal field would be included in our simulations.
NS-NS binaries are much less numerous than BH-BH binaries (as we showed in Figure 3.1), but the distribution of their orbital parameters indicates that NS-NS binaries have generally smaller semi-major axes than BH-BH binaries. This may be due to a selection effect: as NS-NS binary progenitors are often ionized either by natal kicks or by exchanges involving more massive stellar objects (e.g. BHs), only the hardest NS-NS binaries survive in our simulations.
Finally, NS-BH binaries are about 10 times less numerous than BH-BH binaries, but follow approximately the same distribution of orbital parameters.

3.3.4 Mass distribution

The mass of the BHs affects both the frequency and the amplitude of the GW signal (e.g. Maggiore 2008). Thus, it is important to look at the distribution of the masses of the simulated BH-BH binaries.

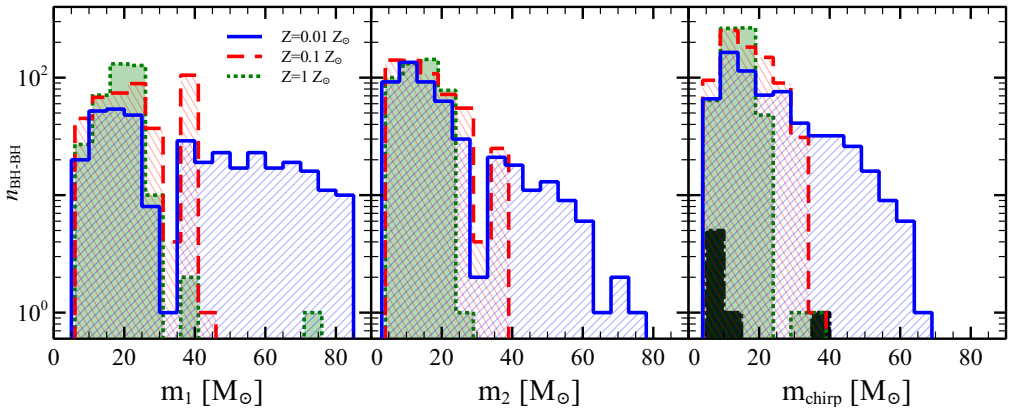

Figure 3.6: From top to bottom: distribution of the primary component, of the secondary component and of the chirp mass of BH-BH binaries, respectively. In each panel, the blue, red and green histograms correspond to $Z = 0.01, 0.1, 1\,Z_\odot$, respectively. In the bottom panel, the black histograms show the distribution of chirp masses of the 7 BH-BH binaries that are expected to merge within a Hubble time (see Section 3.3.5).

Fig. 3.6 shows the distribution of m_1, m_2 and of the chirp mass $m_{\rm chirp}$. The chirp mass is defined as $m_{\rm chirp} = (m_1\,m_2)^{3/5}/(m_1+m_2)^{1/5}$. The chirp mass is named so because it is this combination of m_1 and m_2 that determines how fast the binary sweeps, or chirps, through a frequency band. In fact, it can be shown that the amplitude and the frequency of GWs scale as $m_{\rm chirp}^{5/3}$ and $m_{\rm chirp}^{-5/8}$, respectively (Maggiore 2008).

The mass of the primary (secondary) can be as high as $85\,M_\odot$ ($78\,M_\odot$) in case of $Z = 0.01\,Z_\odot$. Such large values correspond to BHs that formed from direct collapse (see Section 3.2 and paper I).

We also found a $73\,M_\odot$ BH at $Z = Z_\odot$, i.e. a much higher mass than expected from stellar evolution of isolated stars with solar metallicity. This BH is the result of a dynamically induced merger between a smaller BH ($14.9\,M_\odot$) and a star ($59.3\,M_\odot$).

Chirp masses are very high, too. The black histogram in Fig. 3.6 shows the chirp mass distribution of our best BH-BH merger candidates (i.e. of those systems that are expected to merge within a Hubble time, see next section for

t_{GW} (Gyr)	a (AU)	P (yr)	ecc	Z ($Z_\odot$)	Merger
0.09	7.77	2.27788	0.997	0.01	N
0.20	0.03	0.00107	0.019	0.1	N
0.67	0.04	0.00196	0.019	0.1	N
1.34	0.05	0.00267	0.019	0.01	N
1.49	0.05	0.00276	0.014	0.1	N
1.76	0.05	0.00296	0.028	0.01	N
2.06	0.07	0.00387	0.016	0.01	N

Table 3.3: List of the BH-BH binaries with coalescence timescale < 13 Gyr, in ascending order of coalescence timescale. Column 1: coalescence timescale in Gyr; column 2: semi-major axis in AU; column 3: period in years; column 4: eccentricity; column 5: metallicity; column 6: whether or not (Y/N) the binary merges during the simulation.

details): we notice that one of these systems has a significantly high chirp mass ($m_{\rm chirp} \simeq 40\,{\rm M}_\odot$).

The GW searches for BH-BH binaries performed by LIGO and VIRGO (Abadie et al., 2012b; Aasi et al., 2013) cover the mass range found by the present simulation. The signal corresponding to our higher chirp masses can be detected by the Intermediate Mass Binary Black Holes search (Abadie et al., 2012a).

In the adopted model, the chirp mass strongly depends on the metallicity of the progenitor stars. Since the amplitude and the frequency of GWs scale as $m_{\rm chirp}^{5/3}$ and $m_{\rm chirp}^{-5/8}$, respectively, it will be possible to link the observed GW signal to the chirp mass of the source. Observing large chirp masses would be clear evidence for the scenario of BH birth and evolution in the low metallicity environments.

3.3.5 Coalescence timescale

The timescale for coalescence (Peters, 1964) is defined as

$$t_{\rm GW} = \frac{5}{256}\frac{c^5\, a^4\, (1-e^2)^{7/2}}{G^3\, m_1\, m_2\, (m_1+m_2)}, \tag{3.3}$$

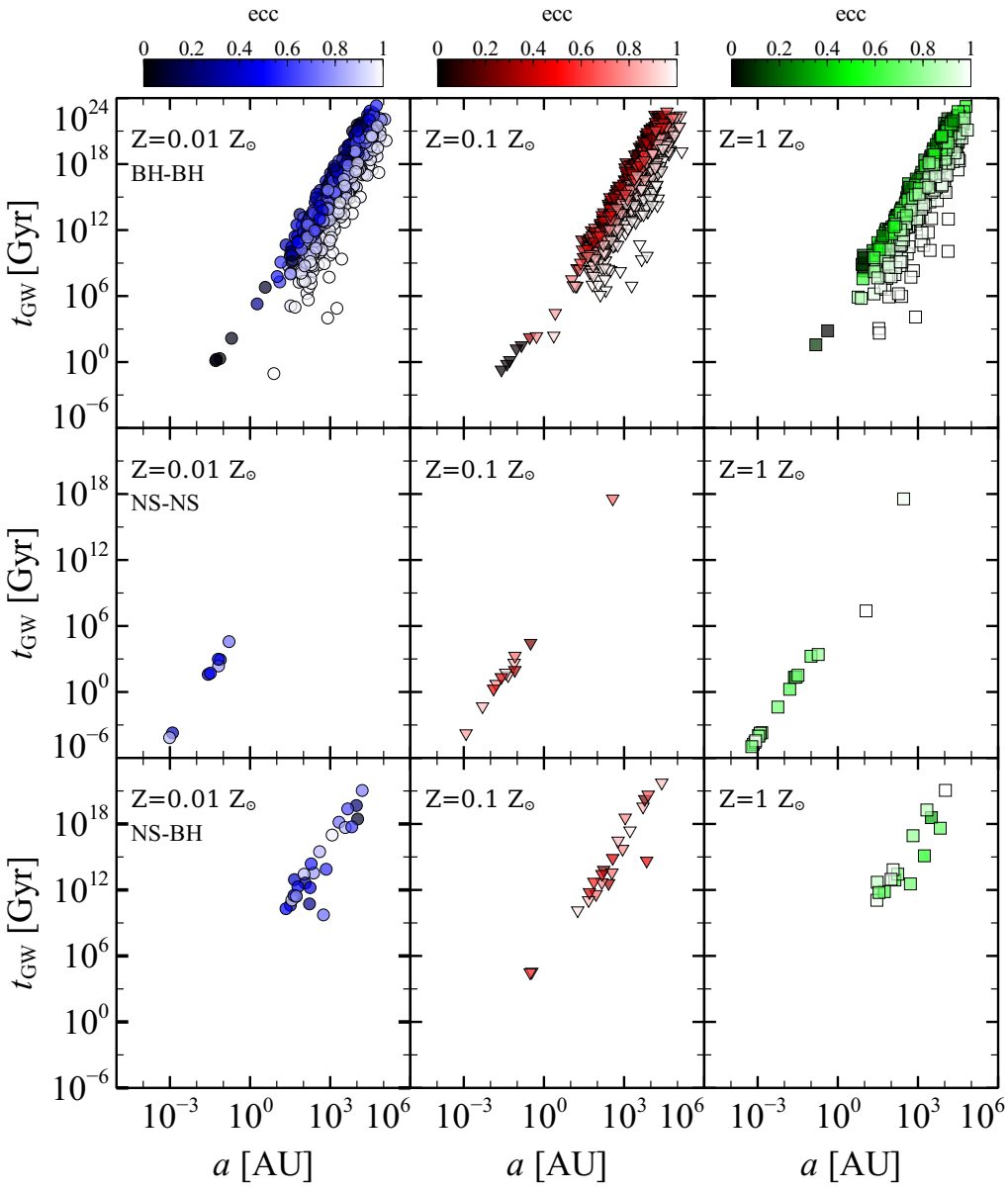

Figure 3.7: Coalescence timescale as a function of the semi-major axis for BH-BH binaries, NS-NS binaries and NS-BH from top to bottom. From left to right: metallicity $Z = 0.01\ Z_\odot$ (blue circles), $0.1\ Z_\odot$ (red triangles) and $1\ Z_\odot$ (green squares). The color-coded map refers to eccentricity.

t_{GW} (Myr)	a (10^{-3} AU)	P (10^{-5} yr)	ecc	Z ($Z_\odot$)	Merger
0.01	0.60	0.9	0.005	1	Y
0.02	0.69	1.1	0.01	1	Y
0.03	0.79	1.4	0.05	1	Y
0.04	0.84	1.5	0.05	1	Y
0.07	0.97	1.9	0.08	0.01	Y
0.1	1.09	2.2	0.06	1	Y
0.1	1.1	2.4	0.03	1	Y
0.2	1.2	2.7	0.09	0.1	Y
0.2	1.2	2.7	0.08	1	Y
0.2	1.3	2.8	0.06	0.01	Y
0.2	1.4	3.3	0.31	1	Y
40	5.7	26.9	0.42	1	N
50	5.0	22.3	0.09	0.1	N
1760	20	12.5	0.51	1	N
1960	10	93.4	0.21	0.1	N
5330	20	13.0	0.11	0.1	N

Table 3.4: List of NS-NS binaries with coalescence time < 13 Gyr, in ascending order of coalescence timescale. Column 1: coalescence timescale in Myr; column 2: semi-major axis in units of 10^{-3} AU; column 3: period in units of 10^{-5} yr; column 4: eccentricity; column 5: metallicity; column 6: whether or not (Y/N) the binary merges during the simulation. The minimum, mean and maximum difference between the real merger and the coalescence times are 0.02, 0.24 and 0.12 Myr, respectively.

where c is the speed of light and G the gravitational constant. t_{GW} is the timescale for a binary to merge by GW emission. It scales as a^4, and it is shorter for high eccentricity. GW emission affects the coalescence timescale by shrinking the semi-major axis and circularizing the binary orbit. Fig. 3.7 shows t_{GW} as a function of semi-major axis, eccentricity and metallicity of the simulated systems.

Most of the systems with $t_{GW} \leq t_H$ (where t_H = 13 Gyr is the Hubble time) have eccentricity close to zero, as a consequence of circularization by GW emission. However, we found an outlier (with eccentricity $e = 0.997$, see Table 3.3) produced by dynamical exchange. This is interesting not only because its

coalescence timescale is short, due to the high value of the eccentricity, but also because it suggests that the use of templates which include eccentric effects in the LIGO and VIRGO searches could be important (Brown and Zimmerman, 2010). Unfortunately, this binary is destroyed by a new dynamical exchange before it merges. On the other hand, we expect to find other systems like this with a larger simulation sample, and we cannot exclude that some of them can evolve (without being destroyed by further exchanges) till they merge. Such systems would be very important for GW detection (Brown and Zimmerman, 2010; Samsing, MacLeod, and Ramirez-Ruiz, 2014).

All BH-BH binaries with $t_{\rm GW} \leq t_{\rm H}$ are at low metallicity ($Z = 0.01$ $Z_{\odot}$ and $Z = 0.1$ $Z_{\odot}$), while we find none at solar metallicity. The bottom panels in Fig. 3.7 show the coalescence timescale for NS-NS binaries. The total number of NS-NS binaries is much smaller than that of BH-BH binaries but they are much harder. As a consequence, their coalescence timescales are generally shorter. The minimum coalescence timescale for BH-BH binaries in our simulations is $t_{\rm GW} \sim 0.1$ Gyr, while that for NS-NS binaries is $t_{\rm GW} \sim 10^{-5}$ Gyr. We also found that 11 NS-NS binaries actually merged before 100 Myr.

In the bottom panel of Fig. 3.7, we also show the coalescence timescale for NS-BH binaries. No NS-BH mergers are expected in less than a Hubble time, because NS-BH binaries are much less numerous than BH-BH binaries and they are not favored by dynamical encounters.

Tables 3.3 and 3.4 list the shortest coalescence timescales for BH-BH binaries and NS-NS binaries, respectively.

It has been debated (e.g. Clausen, Sigurdsson, and Chernoff 2013) whether $t_{\rm GW}$ is a reliable indicator of the merger timescale in star clusters. In fact, dynamical interactions in star clusters may affect the evolution of a DCOB and delay or anticipate the merger with respect to the expected $t_{\rm GW}$. In our simulations there is good agreement between the coalescence timescales and the actual mergers, thus, we can conclude that in most cases dynamics does not affect the actual merger timescale of the simulated NS-NS binaries.

3.4 Discussion

3.4.1 Estimate of the merger rate

Since most stars form in YSCs, the mass density of YSCs in the Universe is expected to scale as the star formation rate (SFR) density (Mapelli et al. 2010a). Thus, from the results discussed in Section 3.3.5 and using a Drake-like equation, the merger rate of BH-BH binaries can be estimated as

$$\begin{aligned} R_{\rm BH-BH} &= N_{\rm mrgr,BH-BH} \quad \rho_{\rm SF} \quad t_{\rm life} \quad f_{\rm SF} \\ &= 3.5\times10^{-3}\,{\rm Mpc^{-3}\,Myr^{-1}} \\ &\left[\frac{N_{\rm mrgr,BH-BH}}{3\times10^{-15}\,{\rm M_\odot}^{-1}\,{\rm yr^{-1}}}\right]\left(\frac{\rho_{\rm SF}}{1.5\times10^{-2}\,{\rm M_\odot\,yr^{-1}\,Mpc^{-3}}}\right) \\ &\left(\frac{t_{\rm life}}{10^8{\rm yr}}\right)\left(\frac{f_{\rm SF}}{0.8}\right), \end{aligned} \tag{3.4}$$

where $\rho_{\rm SF}$ is the cosmological density of SFR at redshift zero ($\rho_{\rm SF} = 1.5\times10^{-2}\,{\rm M_\odot\,yr^{-1}\,Mpc^{-3}}$ from Hopkins and Beacom 2006), $t_{\rm life}$ is the average lifetime of a YSC, $f_{\rm SF}$ is the fraction of star formation (SF) that occurs in YSCs (we take $f_{\rm SF} = 0.8$ from Lada and Lada 2003), and $N_{\rm mrgr,BH-BH}$ is the number of BH-BH binary mergers per solar mass per year, as estimated from our simulations (see Table 3.3). In equation 3.4, we assume that $R_{\rm BH-BH}$ does not change significantly with time. This approximation is reasonable for the distance range of Advanced LIGO and VIRGO (see the short discussion at the end of this section).

Equation 3.4 has been derived following the same approach as explained in Mapelli et al. (2010a, see also Mapelli et al. 2012). The main differences between equation 3.4 of this paper and equations 2 and 3 of Mapelli et al., 2010a are the following: (i) in equation 3.4 we just estimate the merger rate, while Mapelli et al., 2010a estimate the detection rate for different interferometers; (ii) in equation 3.4 we derive $N_{\rm mrgr,BH-BH}$ directly from our simulations, while in Mapelli et al., 2010a we used the results of a toy model for intermediate-mass BHs.

In particular, we estimate $N_{\rm mrgr,BH-BH}$ as

$$N_{\rm mrgr,BH-BH} = 3\times10^{-15}{\rm M_\odot}^{-1}\,{\rm yr}^{-1}\left(\frac{N_{\rm exp,BH-BH}}{3}\right)\left(\frac{200}{N_{\rm YSC}}\right)\left(\frac{3500\,{\rm M_\odot}}{\langle M_{\rm TOT}\rangle}\right)\left(\frac{1.5\,{\rm Gyr}}{t_{\rm GW,max}}\right), \quad (3.5)$$

where $N_{\rm YSC}$ is the number of simulated YSCs, $\langle M_{\rm TOT}\rangle$ is the average mass of a single YSC[2], and $N_{\rm exp,BH-BH}$ is the number of BH-BH binaries that are expected to merge within a time $t_{\rm GW,max}$. For example, at $Z = 0.1$ Z$_\odot$, we find that 3 BH-BH binaries are expected to merge within $t_{\rm GW,max} = 1.5$ Gyr (see Table 3.3). At $Z = 0.01$ Z$_\odot$, we find 4 BH-BH binaries are expected to merge within $t_{\rm GW,max} = 2.1$ Gyr, while at $Z = 1$ Z$_\odot$ we do not find any BH-BH binaries that merge within $t_{\rm GW,max} = t_{\rm H}$. Thus, we find that $0 \le N_{\rm mrgr,BH-BH} \le 3\times10^{-15}{\rm M_\odot}^{-1}\,{\rm yr}^{-1}$ depending on the metallicity. The resulting values of the merger rate are $R_{\rm BH-BH} = 0$, 3.3, and $3.5\times10^{-3}\,{\rm Mpc}^{-3}\,{\rm Myr}^{-1}$, if we assume that all YSCs in the local Universe have metallicity 1, 0.1 and 0.01 Z$_\odot$, respectively.

Thus, the merger rate of BH-BH binaries is $R_{\rm BH-BH} \sim 3.5\times10^{-3}\,{\rm Mpc}^{-3}\,{\rm Myr}^{-1}$ if we assume that all YSCs in the local Universe formed at low metallicity ($Z \le 0.1\,{\rm Z_\odot}$), and is $R_{\rm BH-BH} \sim 0$ if we assume that all YSCs in the local Universe formed at high metallicity ($Z = {\rm Z_\odot}$), since in our simulations we did not find any BH-BH binary at $Z = {\rm Z_\odot}$ with coalescence timescale shorter than the Hubble time. Even if the statistics is low, this result is important, as we can conclude that BH-BH binaries are enhanced at low metallicity, where more massive BHs can form.

As a first-order approximation, we can assume that the merger rate of BH-BH binaries in the local Universe is included in this range of values, i.e. $0 \le R_{\rm BH-BH} \le 3.5\times10^{-3}\,{\rm Mpc}^{-3}\,{\rm Myr}^{-1}$. For a more realistic assumption about the metallicity of YSCs in the local Universe, see the discussion at the end of this Section.

[2]Since we simulated only YSCs with $M_{\rm TOT} \sim 3500$ M$_\odot$, equation 3.5 suffers from the approximation that we do not consider a mass spectrum for the simulated YSCs. On the other hand, YSCs with $M_{\rm TOT} \sim 3500$ M$_\odot$ are among the most diffuse YSCs in the local Universe (Lada and Lada 2003). In a forthcoming paper, we will consider a mass spectrum for the YSCs.

Similarly, the merger rate of NS-NS binaries can be estimated as

$$R_{\rm NS-NS} = N_{\rm mrgr,NS-NS} \quad \rho_{\rm SF} \quad t_{\rm life} \quad f_{\rm SF}$$
$$= 0.15\,{\rm Mpc^{-3}\,Myr^{-1}}$$
$$\left[\frac{N_{\rm mrgr,NS-NS}}{1.3\times10^{-13}\,{\rm M_\odot}^{-1}\,{\rm yr^{-1}}}\right]\left(\frac{\rho_{\rm SF}}{1.5\times10^{-2}\,{\rm M_\odot\,yr^{-1}\,Mpc^{-3}}}\right)$$
$$\left(\frac{t_{\rm life}}{10^8{\rm yr}}\right)\left(\frac{f_{\rm SF}}{0.8}\right), \tag{3.6}$$

where $N_{\rm mrgr,NS-NS}$ is the number of NS-NS binary mergers per solar mass per year and can be derived as

$$N_{\rm mrgr,NS-NS} = 1.3\times10^{-13}{\rm M_\odot}^{-1}\,{\rm yr^{-1}}\left(\frac{N_{\rm exp,NS-NS}}{9}\right)$$
$$\left(\frac{200}{N_{\rm YSC}}\right)\left(\frac{3500\,{\rm M_\odot}}{\langle M_{\rm TOT}\rangle}\right)\left(\frac{100\,{\rm Myr}}{t_{\rm life}}\right), \tag{3.7}$$

where $N_{\rm exp,NS-NS}$ is the number of NS-NS binaries that actually merged during our simulations and $t_{\rm life} = 100$ Myr is the assumed YSC life (and the duration of the simulation). In the case of NS-NS binaries we use the number of merged binaries (rather than the number of expected mergers, as in the case of BH-BH binaries), because we have sufficient statistics to do so. At $Z = 1$, 0.1 and 0.01 $\rm Z_\odot$ $N_{\rm exp,NS-NS} = 9$, 2, 2, respectively.

Thus, the merger rate of NS-NS binaries is $R_{\rm NS-NS} \sim 0.15\,{\rm Mpc^{-3}\,Myr^{-1}}$ if we assume that all YSCs in the local Universe formed at high metallicity ($Z = \rm Z_\odot$, see Table 3.4), and is $R_{\rm NS-NS} \sim 0.03\,{\rm Mpc^{-3}\,Myr^{-1}}$ if we assume that all YSCs in the local Universe formed low metallicity ($Z = 0.01, 0.1\,\rm Z_\odot$). This is another important results of our simulations, as it implies that NS-NS mergers are suppressed at low metallicity.

As a first-order approximation, we can assume that the merger rate of NS-NS binaries in the local Universe is included in this range of values, i.e.
$0.03\,{\rm Mpc^{-3}\,Myr^{-1}} \leq R_{\rm NS-NS} \leq 0.15\,{\rm Mpc^{-3}\,Myr^{-1}}$. In equation 3.6, we assume that $R_{\rm NS-NS}$ does not change significantly with time. This approximation is reasonable for the distance range of Advanced LIGO and VIRGO (see the short discussion at the end of this Section).

Finally, the merger rate of NS-BH binaries is $R_{\rm NS-BH} < 10^{-4}\,{\rm Mpc}^{-3}\,{\rm Myr}^{-1}$ for all considered metallicities, as we found no simulated systems with coalescence timescale shorter than the Hubble time. In our simulations, NS-BH systems are much less common than BH-BH binaries, since the latter are favored by dynamical exchanges with respect to the former.

Our estimates of the merger rate show that there is a possible trend with metallicity: the mergers of NS-NS binaries are favored at high metallicity ($\sim {\rm Z}_\odot$), while the mergers of BH-BH binaries are more frequent at low metallicity ($\sim 0.01-0.1\,{\rm Z}_\odot$). We recall that $Z = 0.01\,{\rm Z}_\odot$ is the typical metallicity of GCs in the Milky Way (e.g. Harris 1996), $Z = 0.1\,{\rm Z}_\odot$ is the metallicity of many irregular galaxies and dwarf galaxies in the local Universe (e.g. Mapelli et al. 2010b), while a metallicity close to solar is normally found in the bulges of giant spiral galaxies and elliptical galaxies (e.g. Pilyugin, Vílchez, and Contini 2004). Furthermore, a metallicity gradient (with Z decreasing at larger distance from the center) has been found in most local late-type galaxies (Pilyugin, Vílchez, and Contini 2004). Thus, the metallicity of the local Universe is quite patchy, with a preference for higher metallicity at the center of the most massive galaxies and for lower metallicity in the outskirts of massive galaxies as well as in dwarf and irregular galaxies.

Furthermore, the Sloan Digital Sky Survey shows that the SF in the last Gyr has a bimodal distribution: about half of it occurs at solar metallicity, while the remaining half takes place at $Z \sim 0.1\,{\rm Z}_\odot$ (Panter et al. 2008). Therefore, we expect that about half of the YSCs that formed in the last Gyr have $Z \sim {\rm Z}_\odot$, while the remaining half have $Z \sim 0.1\,{\rm Z}_\odot$. In contrast, a negligible fraction of YSCs formed at $Z = 0.01\,{\rm Z}_\odot$ in the last Gyr.

If we assume (as suggested by Panter et al. 2008) that half of the YSCs that formed in the last Gyr have $Z \sim {\rm Z}_\odot$, while the remaining half have $Z \sim 0.1\,{\rm Z}_\odot$, the rate of mergers we expect today from our simulated YSCs (using equations 3.6 and 3.4) is $R_{\rm NS-NS} \sim 0.10\,{\rm Mpc}^{-3}\,{\rm Myr}^{-1}$ and $R_{\rm BH-BH} \sim 1.7 \times 10^{-3}\,{\rm Mpc}^{-3}\,{\rm Myr}^{-1}$, for NS-NS and BH-BH binaries, respectively.

The aforementioned values of $R_{\rm NS-NS}$ and $R_{\rm BH-BH}$ have been derived from the

typical properties of YSCs in the local Universe and assuming a metallicity mixture valid for the last Gyr (i.e. up to redshift $z \sim 0.1$). Are they valid over the entire distance range of Advanced LIGO and VIRGO? According to Abadie et al., 2010, the distance range of Advanced LIGO and VIRGO will be ~ 200 Mpc ($z \sim 0.05$) and 1 Gpc ($z \sim 0.2$) for NS-NS and BH-BH mergers, respectively. Thus, we can conclude that our estimated merger rates are fairly uniform (within the uncertainties) across the range of Advanced LIGO and VIRGO, especially in the case of NS-NS mergers.

We recall that the DCOBs that form in YSCs will be ejected to the field as a consequence of evaporation, natal kicks and three-body encounters, and because of the disruption of the parent YSCs by the tidal field of the host galaxy. Thus, the merger rate we estimate in this Section represents the expected merger rate for the field. This is very important, as previous studies estimated the merger rate either for for long-lived GCs (e.g. O'Leary et al. 2006; Downing et al. 2010; Downing et al. 2011) or for the field (e.g. Belczynski et al. 2010b; Dominik et al. 2012; Dominik et al. 2013). In previous work, the effect of dynamics has been included only in the estimate of the merger rate within GCs, while field binaries have been assumed to form and evolve in isolation (through population synthesis codes). On the other hand, it is well known that most stars form in YSCs and evolve dynamically via three-body encounters, before being ejected into the field. Our results show that the estimate of the merger rate in the field should account for dynamical evolution.

3.4.2 Comparison with previous work

Fig. 3.8 compares our predictions of the merger rates with some of the most representative estimates available in the literature. From this Figure, it is apparent that our prediction of $R_{\rm NS-NS}$ is fairly consistent with the estimate derived from short gamma-ray bursts (Coward et al. 2012; Siellez, Boër, and Gendre 2014).

Furthermore, our results for $R_{\rm NS-NS}$ and $R_{\rm BH-BH}$ are consistent with the estimates provided in Abadie et al. (2010). In contrast, our results for $R_{\rm NS-BH}$

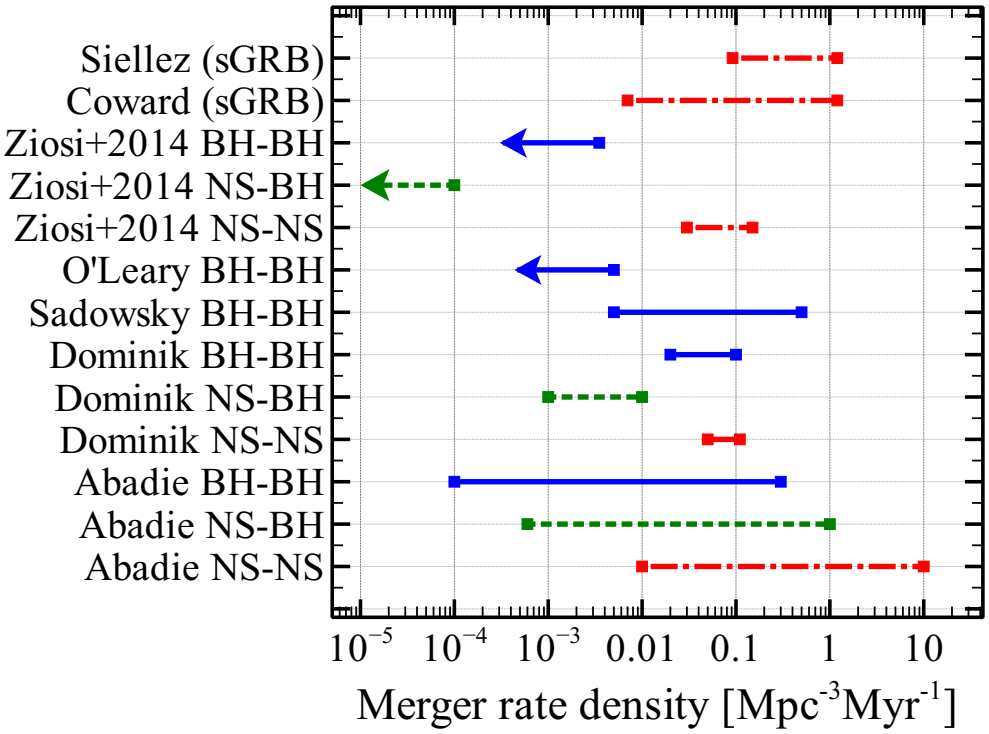

Figure 3.8: Comparison of our predictions for the merger rates of NS-NS, NS-BH and BH-BH binaries with some of the most representative estimates available in the literature. From top to bottom: Siellez, Boër, and Gendre, 2014; Coward et al., 2012; our paper; O'Leary et al., 2006; Sadowski et al., 2008; Dominik et al., 2013; Abadie et al., 2010. The predicted merger rates for Dominik et al., 2013 span from their "Standard" to their "Optimistic CE" model (see Fig. 1 in Dominik et al., 2013).

are significantly lower than predicted by Abadie et al. (2010). We recall that the value of $\mathcal{R}_{\rm NS-NS}$ reported by Abadie et al. (2010) is derived from the observed rate of NS-NS binaries in the Milky Way (Kalogera et al. 2004), while the values of $\mathcal{R}_{\rm NS-BH}$ and $\mathcal{R}_{\rm BH-BH}$ are obtained from population synthesis codes (O'Shaughnessy et al. 2008 and Kalogera et al. 2007, respectively) and are only indirectly constrained by the SN rate.

The main differences between the approach presented in Abadie et al. (2010) and ours are the following. (i) The estimates presented in Abadie et al. (2010) are based on population synthesis simulations of isolated binaries and do not account for the fact that most stars form in YSCs; (ii) the mass spectrum of BHs is significantly different; (iii) Abadie et al. (2010) assume that most galaxies in the local Universe are Milky Way analogues, while in this paper we adopt the cosmic SFR by Hopkins and Beacom (2006). The fact that we account for the dynamical evolution of YSCs and include more massive BHs than Abadie et al. (2010) affects the results significantly, as the formation of BH-BH binaries is enhanced with respect to that of NS-BH systems. In general, our simulated DCOBs cannot evolve in isolation but frequently undergo three-body encounters that perturb their orbits, while the results of Abadie et al. (2010) are obtained assuming that all binaries evolve in isolation.

Recent studies by Belczynski et al. (2010b), Dominik et al. (2012) and Dominik et al. (2013) adopt a BH mass spectrum much more similar to ours and investigate the dependence of the merger rate on metallicity, even if they do not include three-body encounters. As a consequence, the distribution of BH-BH binary chirp masses in the three aforementioned papers is very similar to our distribution. The main difference is the absence of massive BHs that come from a merger in the papers by Belczynski et al. (2010b), Dominik et al. (2012) and Dominik et al. (2013), because they do not allow merged binaries to acquire a new companion dynamically.

In their standard model, Dominik et al. (2013) find an estimate of $\mathcal{R}_{\rm NS-NS}$ that is fairly consistent with ours, while their prediction for $\mathcal{R}_{\rm NS-BH}$ and $\mathcal{R}_{\rm BH-BH}$ are about a factor of ten higher. In addiction, Belczynski et al. (2010b), Dominik

et al. (2012) and Dominik et al. (2013) present an alternative model in which common envelope (CE) phases on the Hertzsprung gap are allowed (i.e. the binary is not assumed to merge when one of the two members reaches the Hertzsprung gap). The merger rates obtained with this assumption are a factor of ≥ 100 higher than our results. This discrepancy is consistent with our expectations, as our simulations adopt the same recipes for the CE phase as in the standard model of Dominik et al. (2013)[3].

Sadowski et al. (2008) study the merger rate of DCOBs in GCs and in the field by means of Monte Carlo simulations and population synthesis models, respectively. They find that NS-NS binaries and NS-BH binaries should dominate the DCOB population in the field, whereas BH-BH binaries are the main merger candidates in GCs. We confirm their result, in the sense that the formation of BH-BH binaries is enhanced by dynamics in star clusters. Our results agree with those of Sadowski et al. (2008) also for the importance of dynamical exchanges: Sadowski et al. (2008) find that 6 per cent (94 per cent) of BH-BH binary merger candidates come from primordial binaries (dynamical exchanges), while we find that 1.7 per cent of our BH-BH binaries come from primordial binaries.

On the other hand, Sadowski et al. (2008) neglect the fact that many of the merger candidates in the field have been ejected from YSCs (by dynamical ejection, natal kick or YSC disruption). Accounting for field DCOBs that were ejected from YSCs increases the relative importance of BH-BH binaries in the field, especially at low metallicity. Furthermore, Sadowski et al. (2008) find a merger rate $R_{\rm BH-BH} \sim 0.005 - 0.5$ Mpc^{-3} Myr^{-1} in dense star clusters, substantially higher than our result ($R_{\rm BH-BH} \leq 0.0035$ Mpc^{-3} Myr^{-1}), because they assume that the BHs remain in dynamical equilibrium with the rest of the cluster. This suppresses the dynamical ejection of BHs.

Other recent papers (O'Leary et al. 2006; Downing et al. 2010; Downing et al. 2011; Clausen, Sigurdsson, and Chernoff 2013) focus on DCOB merger in dense stellar systems and GCs. In particular, O'Leary et al. (2006) perform

[3] As discussed in paper I, we adopt $\alpha_{\rm CE}\,\lambda = 0.5$ to model the CE phase (see Davis, Kolb, and Knigge 2012 for a definition), and we assume that all binaries that enter a CE phase when at least one of the two members is in the Hertzsprung gap merge.

Monte Carlo simulations of GCs in which they assume that the BH population is concentrated in the core and dynamically decoupled from the rest of the cluster, because of the Spitzer instability (Spitzer 1969). O'Leary et al. (2006) find that most BH-BH binaries are ejected from the parent star cluster and that the resulting merger rate is $R_{\rm BH-BH} \leq 0.005$ Mpc^{-3} Myr $^{-1}$, much lower than in Sadowski et al. (2008), because of the assumed Spitzer instability. The merger rate estimated by O'Leary et al. (2006) is very similar to our result.

Downing et al. (2010) and Downing et al. (2011) perform Monte Carlo simulations of GCs. They (i) include a treatment of metallicity that is close to ours (even if their maximum BH mass is generally lower than ours, as they use the same distribution as in Belczynski et al. 2006), (ii) assume neither Spitzer instability nor rigid equilibrium between the BHs and the rest of the cluster *a priori*. Downing et al. (2010) find that the BHs strongly mass segregate and evolve similarly to what assumed by O'Leary et al. (2006). Downing et al. (2010) find an even lower merger rate than the one derived by O'Leary et al. (2006) and by our paper, but they admit that this may be due to their approximate treatment of three-body encounters. On the other hand, the distribution of orbital periods in the simulations by Downing et al. (2010) is similar to ours (see Fig. 3.5). Furthermore, both this paper and Downing et al. (2010) find that most BH-BH binaries form dynamically, through exchanges. Finally, Downing et al. (2010) find that BH-BH binaries form earlier and are more stable at low metallicity, because BHs are more massive, in agreement with our results (see Figures 3.2 and 3.3).

In conclusion, our results confirm that most BH-BH binaries in star clusters come from dynamical exchanges, in agreement with the findings of Monte Carlo simulations of dense star clusters (O'Leary et al. 2006; Downing et al. 2010; Downing et al. 2011). On the other hand, our simulated star clusters are a factor of $10-1000$ less massive and a factor of ≥ 5 smaller than those studied in previous work (e.g. Downing et al. 2010). Thus, they are expected to be much more numerous in the local Universe than those considered by previous work (since the mass function of YSCs scales as $M_{\rm TOT}^{-2}$, Lada and Lada

2003). Furthermore, the dynamical evolution timescale of our simulated YSCs is much shorter, as $t_{\rm rlx} \sim 10\,{\rm Myr}\,(r_{\rm hm}/0.8\,{\rm pc})^{3/2}\,(M_{\rm TOT}/3500\,{\rm M}_{\odot})^{1/2}$. Thus, most DCOBs that form in our simulated YSCs will be ejected to the field (by YSC evaporation, three-body encounters or tidal fields), over a timescale much shorter than found in previous work. Therefore, our YSCs can be considered the building blocks of the galaxy disc, and the merger rate we have estimated represents the expected merger rate of the field population.

3.5 Stable versus unstable DCOBs

As we mentioned in Section 3.3.1, in our paper a binary system is defined as a bound pair, i.e. the most general possible definition. On the other hand, it is reasonable to expect that a portion of these binaries are extremely loose systems, which remain bound only for one (or few) time-steps (see the discussion in Section 3.3.3). In this Appendix, we discuss how our results are influenced by our definition of binary systems. In particular, we will compare the main properties of stable and unstable DCOBs.

STARLAB defines as stable binaries those bound pairs with periastron distance $r_{\rm p} \leq 2.5\,R_{\rm close}$ (see Portegies Zwart et al. 2001), where $R_{\rm close}$ is defined as

$$R_{\rm close} = r_{\rm vir}\frac{m_1+m_2}{2\,M_{\rm tot}}. \tag{3.8}$$

Then, unstable binaries are binaries with periastron $r_{\rm p} > 2.5\,R_{\rm close}$. In the following, we consider stable and unstable binaries separately.

3.5.1 DCOB population

Fig. 3.9 is the same as Fig. 3.1, but it has been derived considering stable and unstable binaries separately (in the top and bottom panel, respectively). The inset of Fig. 3.9

shows the average number of BH-BH, NS-NS and NS-BH per YSC as a function of the metallicity. It is remarkable that BH-BH binaries are at least ten times

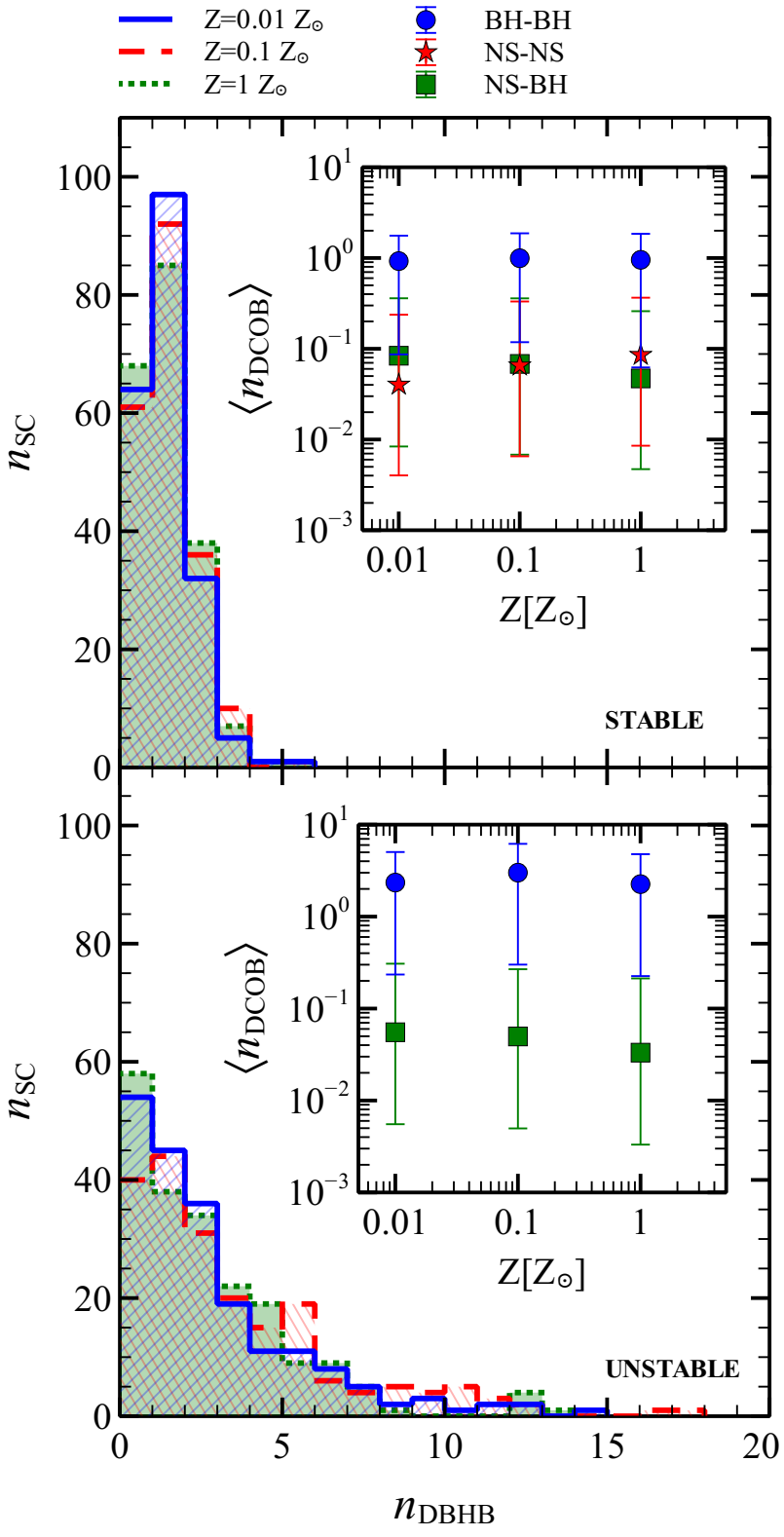

Figure 3.9: The same as Fig. 3.1, but we distinguish between stable (top) and unstable (bottom) binaries.

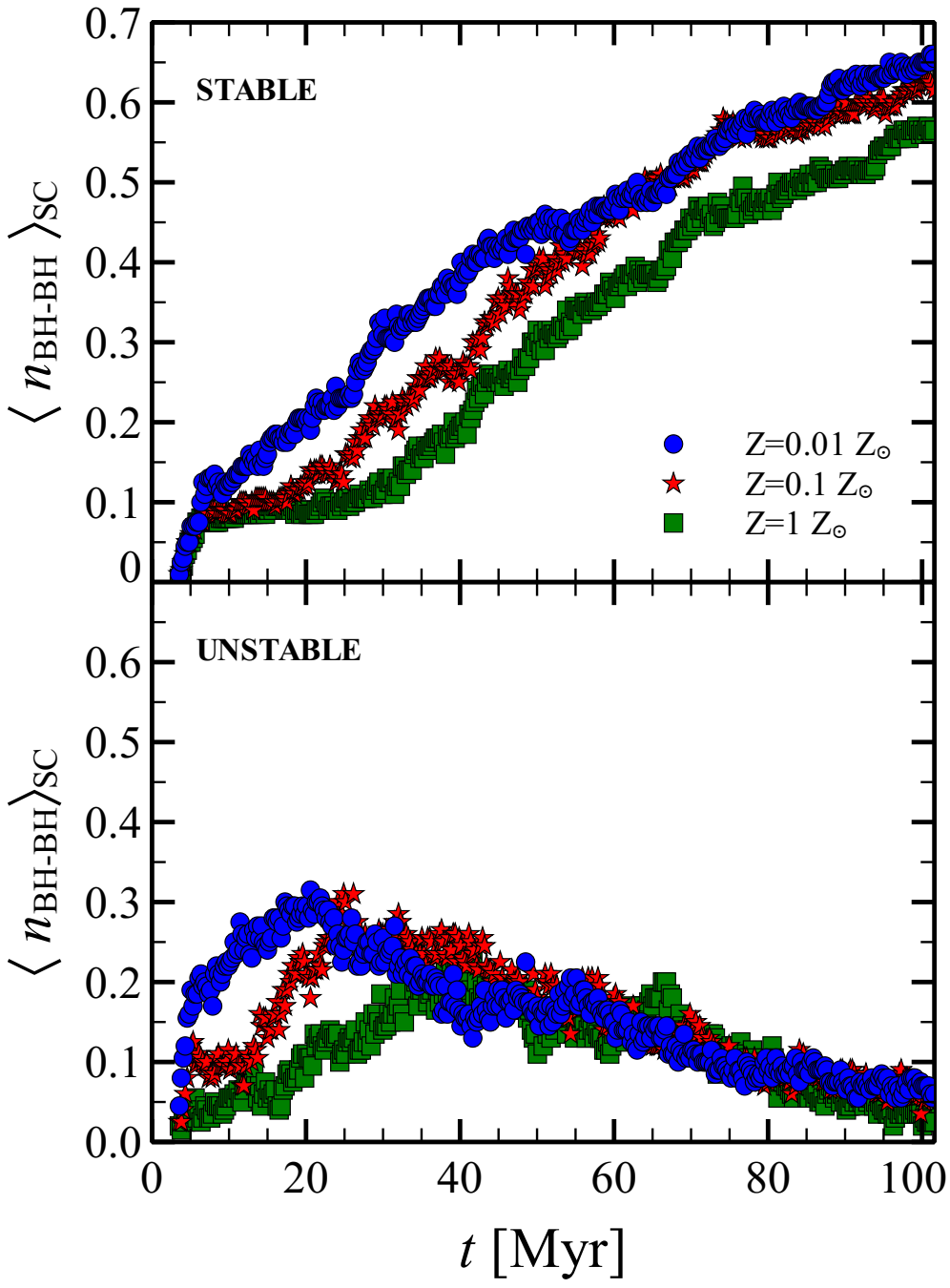

Figure 3.10: The same as Fig. 3.2, but we distinguish between stable (top) and unstable (bottom) binaries.

more numerous than NS-NS and NS-BH binaries, when considering both the stable binary sample and the unstable binary sample. This shows that dynamics has a strong impact on the population of DCOBs, regardless of the distinction between stable and unstable binaries. It is also worth noting that we have found no unstable NS-NS binaries. This confirms that only hard (stable) NS-NS binaries can survive (without being disrupted) the two SN explosions of the two progenitors and the dynamical evolution of the binary.
The main panel of Fig. 3.9 shows the distribution of BH-BH binaries per YSC (integrated over the simulation time). Here, the difference between stable and unstable binaries is quite marked: a single YSC can host up to ~ 18 unstable binaries, but only up to ~ 6 stable binaries.
Fig. 3.10 compares the average number of BH-BH binaries per YSC as a function of time for stable (top) and unstable (bottom) binaries. It is worth noting that unstable binaries peak at $10\,\mathrm{Myr} < t < 40\,\mathrm{Myr}$, i.e. immediately after the core collapse: it is reasonable to expect that the formation of loose binaries is triggered by the increase of the central density due to the core collapse phase (see Mapelli and Bressan 2013). In contrast, the number of stable binaries steadily increases with time (because they tend to survive for a longer time, after their formation). The differences among metallicities that we discussed in Section 3.3.1 still hold, when considering stable and unstable binaries separately.

3.5.2 Orbital properties and coalescence timescale

Fig. 3.11 shows the distribution of semi-major axes of BH-BH, NS-NS and NS-BH binaries at $Z = 0.1\,\mathrm{Z}_\odot$, distinguishing between stable (top) and unstable (bottom) binaries. As it is reasonable to expect, most unstable (stable) binaries have semi-major axes $> 10^3$ AU ($< 10^3$ AU). However, there are also some unstable binaries with a smaller than that of stable binaries. The reason is that the stability criterion depends not only on the separation of the two objects, but also on their mass (in this sense, it is a hardness criterion) and eccentricity. In the bottom panel of Fig. 3.11, the most loose unstable binaries have semi-

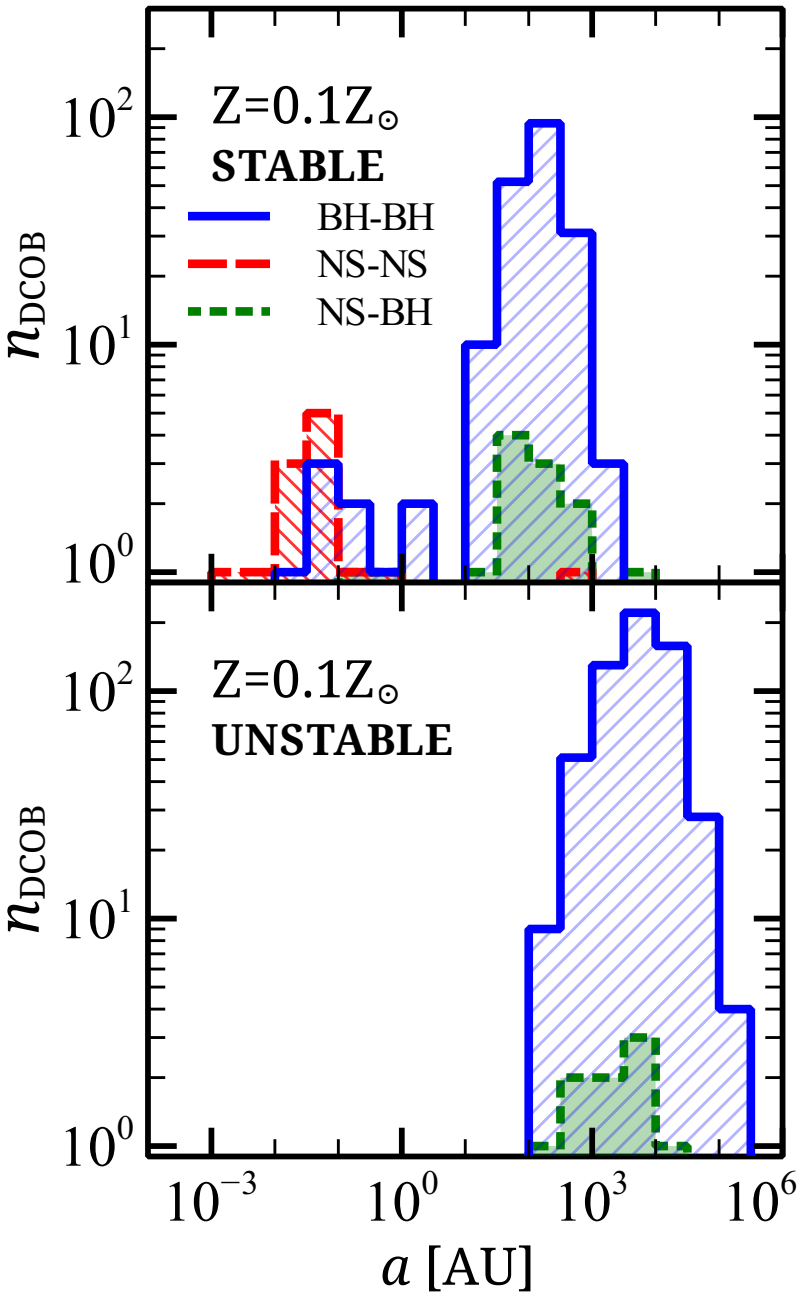

Figure 3.11: Distribution of semi-major axes a for the stable (top) and unstable (bottom) DCOBs at $Z = 0.1\ Z_\odot$. Lines and colours are the same as in Fig. 3.5.

major axes as large as 10^6 AU, that is ~ 5 pc (similar to the initial YSC tidal radius), with periods comparable to the initial central two-body relaxation time (~ 10 Myr, see also Fig. 3.5). These extremely loose bound pairs are very short-lived: it is reasonable to expect that they would completely disappear, if a galactic tidal field would be included in our simulations. On the other hand, these highly unstable systems are completely negligible from the point of view of GW sources.

Fig. 3.12 confirms that unstable DCOBs are completely negligible from the point of view of GW emission: their coalescence timescale is by orders of magnitude longer than the Hubble time. Thus, it is sufficient to consider stable binaries alone, when we are interested in possible GW sources.

Finally, in this Section we have considered only YSCs with $Z = 0.1$ $Z_\odot$ as an example. The same conclusions can be drawn for the other metallicities.

3.6 Conclusions

We studied the impact of metallicity and dynamics on the formation and evolution of DCOBs. To this purpose, we have run 600 N-body realizations of YSCs chosen to match the properties of the most common YSCs in our Galaxy. We simulated YSCs, because most stars form in YSCs. Thus, we cannot study the formation and evolution of DCOBs without accounting for the fact that most of them originate in YSCs.

For our simulations, we used an upgraded version of the public code STARLAB, which includes recipes for metallicity-dependent stellar evolution and winds, and which allows stars with final mass larger than $40\,M_\odot$ to directly collapse to a BH. Direct collapse leads to the formation of massive stellar BHs ($\geq 25\,M_\odot$) at low metallicity.

We found that, while the number of NSs is about four times larger than the number of BHs, the number of BH-BH binaries is about ten times higher than the number of NS-NS binaries. The reason is that dynamical interactions enhance the formation of BH-BH binaries with respect to NS-NS binaries.

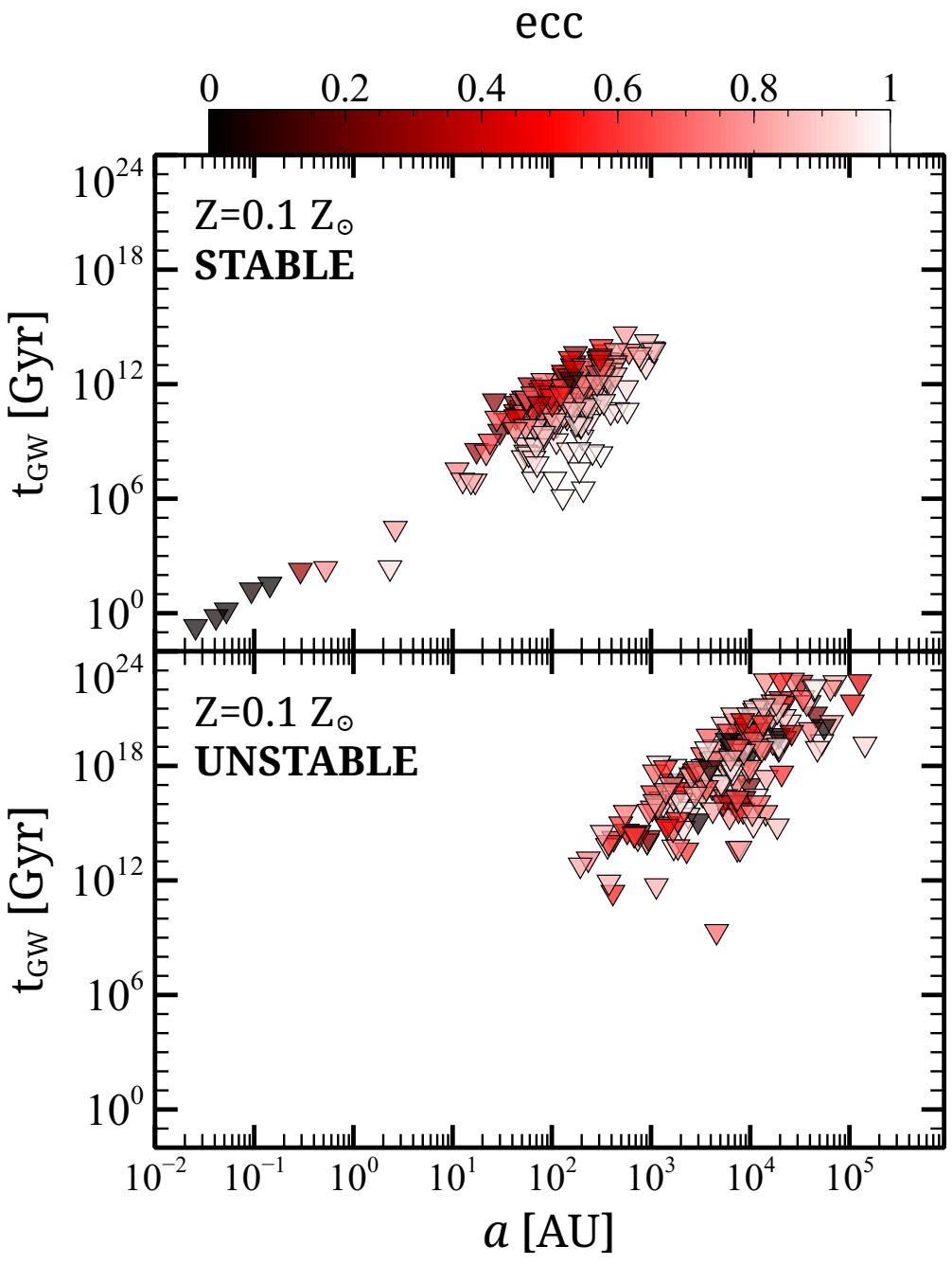

Figure 3.12: Coalescence timescale as a function of the semi-major axis for stable (top) and unstable (bottom) BH-BH binaries at $Z = 0.1\ Z_\odot$. Symbols and colors are the same as in Fig. 3.7.

Heavier BHs sink to the center of the YSC, where they are more likely to interact with other BHs: BHs can acquire companions through three-body exchanges. Since the probability of a dynamical exchange is higher when the single star is more massive than one of the members of the binary and since BHs are among the most massive objects in a YSC, exchanges Cavour the formation of BH-BH binaries.

BH-BH binaries form earlier at low metallicity, because BHs are more massive in metal-poor YSCs. Furthermore, BH-BH binaries formed at low metallicity are more stable: they live longer than BH-BH binaries in metal-rich YSCs.

The simulated BH-BH binaries have very large chirp masses ($5-70\,M_{\odot}$), because of the direct collapse at low metallicity and because mergers between stars and BHs are allowed.

BH-BH binaries span a wide range in periods ($10^{-3}-10^{7}$ yr). In contrast, most NS-NS binaries have periods <1 yr. As a consequence, the coalescence timescale is generally longer for BH-BH binaries than for NS-NS binaries. The minimum coalescence timescale for BH-BH binaries and NS-NS binaries is $t_{\rm GW}\sim 0.1$ Gyr and $t_{\rm GW}\sim 10^{-5}$ Gyr, respectively. Only 7 BH-BH binaries are expected to merge within a Hubble time. Moreover, no BH-BH binaries merge during our simulations, while 11 NS-NS binaries do.

From our simulations, we can estimate the merger rate of DCOBs in the local Universe. We find a merger rate $R_{\rm BH-BH}\leq 3.5\times 10^{-3}\,{\rm Mpc^{-3}\,Myr^{-1}}$, $R_{\rm NS-BH}<10^{-4}\,{\rm Mpc^{-3}\,Myr^{-1}}$ and $R_{\rm NS-NS}\sim 0.03-0.15\,{\rm Mpc^{-3}\,Myr^{-1}}$ for BH-BH, NS-BH and NS-NS binaries, respectively. The merger rate of NS-NS binaries is fairly consistent with the estimates based on both the observed Galactic NS-NS binaries (Kalogera et al. 2004) and the observed rate of short gamma-ray bursts (Coward et al. 2012; Siellez, Boër, and Gendre 2014). The merger rate of BH-BH binaries is consistent with recent Monte Carlo simulations of dense star clusters (e.g. O'Leary et al. 2006; Downing et al. 2010). The merger rate of NS-BH binaries is quite low with respect to previous estimates based on population synthesis codes (e.g. O'Shaughnessy et al. 2008). This can be explained with the fact that the formation of NS-BH binaries is less favored by dynamical

exchanges than the formation of BH-BH binaries.
Our merger rates are still affected by a number of assumptions that will be improved in forthcoming studies. First, in our study we assume that the lifetime of the simulated YSCs is 100 Myr, but we do not take into account the presence of a realistic galactic tidal field. Second, we explore only a limited portion of the parameter space. In forthcoming studies, we will consider YSCs with different concentration, half-mass radius, total mass and binary fraction.
Our simulated YSCs are expected to dissolve in the galactic disc in ~ 100 Myr, that is much shorter than the coalescence timescale of all BH-BH binaries and of some NS-NS binaries. The DCOBs that form within the simulated YSCs are ejected in the field (due to three-body interactions or because of the disruption of the parent YSC). Once in the field, the DCOBs will not undergo more dynamical interactions and will continue their evolution in isolation, until they merge. Thus, the mergers of (most) our simulated DCOBs are expected to take place in the field. Accounting for the fact that most DCOBs form in YSCs and evolve through dynamical interactions is a crucial step towards obtaining a realistic description of the demographics of DCOBs, in light of the forthcoming Advanced LIGO and VIRGO scientific runs.

CHAPTER 4

IMPACT OF YSC STRUCTURAL PARAMETERS ON DCOBS

The results provided in Section 3 are based on random realizations of a single model of SC at three different metallicities, $Z = 0.01, 0.1, 1 Z_{\odot}$. How does this assumption affect the results? Are some properties more important than others in shaping the DCOB population? This chapter will try to answer these questions.

Section 4.1 presents the grid of parameters and their values adopted in this part of the project. Section 4.2 is devoted to describe i) how the simulations were prepared and run, ii) how the analysis was carried out and iii) the tools I wrote to handle the previous two points. Section 4.3 presents the results I obtained.

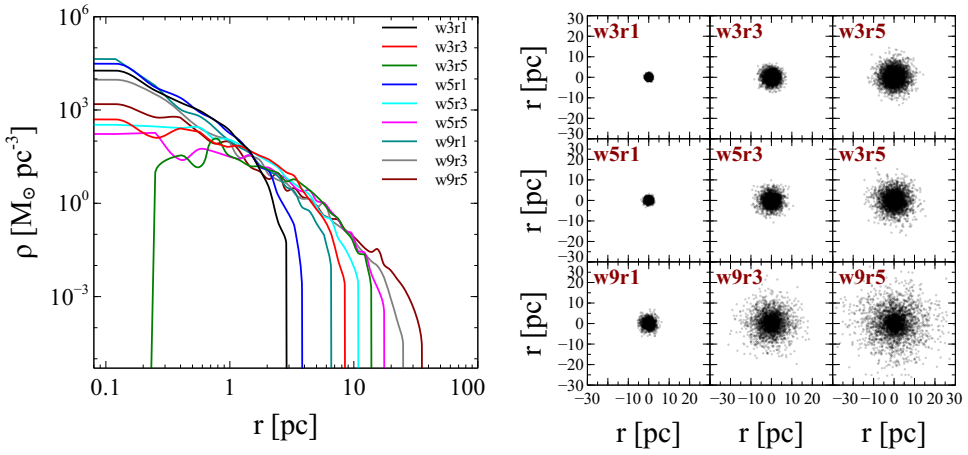

Figure 4.1: Density profiles of clusters (left) and initial positions of stars (right) in clusters spanning different initial virial radius r_v and central adimensional potential W_0. The profiles are sampled from 9 initial conditions generated with STARLAB.

4.1 Simulation grid

I created a grid of simulations encompassing a wide selection of parameters and combinations of them.

Table 4.1 shows the parameters I investigated. Table 4.2 shows the number of runs that I completed for each combination of the parameters. More runs are in preparation.

Fig. 4.1 shows clusters with different virial radius r_V and central adimensional potential W_0. A smaller value of the virial radius produces a more dense cluster model, while a higher value of the central adimensional potential results in a higher concentration one (see Section 2.2.2).

Comb.	#rand. real.	r_v	Z [$Z_\odot$]	NCM	W_0	f_{PB}	TF
1	200	1	0.01	5×10^3	5	0.1	no
2	200	1	0.1	5×10^3	5	0.1	no
3	200	1	1	5×10^3	5	0.1	no

Comb.	#rand. real.	r_v	Z [$Z_\odot$]	NCM	W_0	f_{PB}	TF
4	49	1	0.1	1×10^4	5	0.05	no
5	19	1	0.1	1×10^4	5	0.1	no
6	50	1	0.1	1×10^4	9	0.05	no
7	10	1	0.1	1×10^4	9	0.1	no
8	10	1	1	1×10^4	5	0,05	no
9	9	1	1	1×10^4	5	0.1	no
10	9	1	1	1×10^4	5	0.2	no
11	10	1	1	1×10^4	9	0,05	no
12	10	1	1	1×10^4	9	0.1	no
13	10	3	0.1	1×10^4	5	0.05	no
14	10	3	0.1	1×10^4	5	0.1	no
15	10	3	0.1	1×10^4	5	0.2	no
16	50	3	0.1	1×10^4	9	0.05	no
17	9	3	0.1	1×10^4	9	0.1	no
18	10	3	0.1	1×10^4	9	0.2	no
19	10	5	1	1×10^4	5	0.05	no
20	50	5	1	1×10^4	5	0.1	no
21	10	5	1	1×10^4	5	0.2	no
22	10	5	1	1×10^4	9	0.05	no
23	10	5	1	1×10^4	9	0.1	no
24	10	5	1	1×10^4	9	0.2	no
25	10	1	0.1	1×10^4	3	0.05	no
26	10	1	0.1	1×10^4	3	0.1	no
27	10	1	0.1	1×10^4	3	0.2	no
28	7	3	0.1	1×10^4	3	0.05	no
29	10	3	0.1	1×10^4	3	0.1	no
30	9	3	0.1	1×10^4	3	0.2	no
31	10	1	1	1×10^4	3	0.05	no
32	8	1	1	1×10^4	3	0.1	no
33	10	5	1	1×10^4	3	0.05	no

Comb.	#rand. real.	r_v	Z [$Z_\odot$]	NCM	W_0	f_{PB}	TF
34	10	5	1	1×10^4	3	0.1	no
35	10	5	1	1×10^4	3	0.2	no
36	50	5	0.1	1×10^4	3	0.05	no
37	36	3	1	1×10^4	5	0.1	no

Table 4.2: Grid of completed simulations. Column 1: number that identifies the parameter combination; column 2: number of random realization of a certain model; column 3: virial radius r_v; column 4: metallicity (Z) in units of the solar metallicity; column 5: number of center of masses in the model; column 6: central adimensional potential (W_0); column 7: the fraction of primordial binaries (f_{PB}); column 8: flags that indicates whether or not the run includes the tidal field of the host galaxy (see chapter 5). The first 3 rows in this tables refer to the simulations in Ziosi et al. (2014).

4.2 Methods

4.2.1 Simulations

The methods I adopted for this part of the project are based on what I already described in Section 3.2. However, given the number of simulations with different properties I had to manage I developed several tools called SLTOOLS (Ziosi, 2015). These tools, bundled in a single, portable (statically compiled) binary file, provide everything needed to run simulations with STARLAB.
The tools available are:

`slrecompile` safely recompiles STARLAB, it make sure that libraries and binaries are properly cleaned and updated (while `make clean && make` does not)

`createICs` creates the scripts (and optionally run them) to generate all the initial conditions for a parameter set specified in a configuration file

Parameter	Values
W_0	3, 5, 9
N_*	5×10^3, 1×10^4
r_v (pc)	1, 3, 5
Z ($Z_\odot$)	0.1, 1
f_{PB}	0.05, 0.1, 0.2

Table 4.1: Summary of the initial properties of the simulated SCs: central adimensional potential (W_0), number of centers of mass (N_*), virial radius (r_v), metallicity (Z), primordial binary fraction (f_{PB}).

`css` generates the scripts needed to submit a bunch of simulations to a batch queue manager on a Linux cluster

`kiraWrap` wraps the proper `kira` (STARLAB) binary with the related flags to run a simulation; during the simulation it tries to ensure the simulation writes in the right output files. It also checks the output files and the system environment to stop the simulation if either the code is stalling or the systems exhausted memory or disk space. Moreover, it add useful information to the output files and to the batch manager log files

`checkEnd`, `checkStatus`, `checkSnapshot` check the status of the output files (simulation progress and file sanity)

`relaunch`, `continue`, `cac`, `pbsLaunch`, `out2ics`, `restartFromHere`, `simClean` check the simulations progress, the files sanity and manage to clean the folder and if it is the case to restart the simulations generate the batch manager files and submit the jobs. If the simulations are finished, clean the folder and warn that the simulations are completed.

`cutsim`, `simsplit` cut the simulations outputs at a certain timestep or split the outputs in its snapshots

`out2ics` generates new initial conditions from the last output file (to restart the simulation)

stitchOutput stitches together (checking for file sanity) the outputs related to the same simulations for all the simulation in the folder

comorbit, **clusterPrint**, **profiles** print the center of mass, particles and binaries positions along the whole simulation

autosim, **simman** check the simulation status on a remote cluster and manage to restart the simulations when needed (this tools are still experimental)

dockerBuild automatically builds a docker image with all the STARLAB variants targeting a certain system (this is necessary since the CUDA driver inside the image need to match those installed in the host system)

fish2smtg collects the data extracted (by my Python analysis scripts) from all the simulation in a single file computing quantities such as the chirp mass and the coalescence timescale

slbase loads all the simulation data to a database for fast access and management

biseek Python tools (not embedded in the single binary) used to extract the binaries data from the simulation output

SLTOOLS requires few starting assumptions:

- all the binary files are store in `$HOME/bin`
- the main STARLAB binary file (integrator + stellar evolution) is called `kira`, with the allowed variants: `kira-noGPU` for the non GPU version, `kiraTF` containing the original tidal field provided with the public version of STARLAB and `kiraAS` with the implementation of the Allen-Santillan (Allen and Santillan, 1991) tidal fields (see Appendix A.1.2)
- some tools require the `STDIN`, `STDOUT` and `STDERR` to be in the form `ics-comb<1>-TF<2>-Rv<3>-NCM<4>-fPB<5>-W<6>-Z<7>-run<8>-rnd<9>.txt`, `err-comb<1>-TF<2>-Rv<3>-NCM<4>-fPB<5>-W<6>-Z<7>-run<8>-rnd<9>.txt`, `out-comb<1>-TF<2>-Rv<3>-NCM<4>-fPB<5>-W<6>-Z<7>-run<8>-rnd<9>.txt`

where

1. is a progressive number identifying the simulation (like a database primary key)
2. the presence or not and the type of the host galaxy tidal field
3. the virial radius
4. the number of center of masses
5. the primordial binary fraction
6. the initial central adimensional potential value
7. the metallicity
8. the number of random realizations
9. the number of a given piece of simulation in case it has to be restarted

For more information about how to use SLTOOLS, see appendix A.1.1.

4.2.2 Analysis

The results presented in Sections 3.3 and 4.3 were obtained by analyzing the output of the simulations described in Sections 3.2 and 4.1. First, I describe in detail how I selected the DCOBs, because the results I present stand on the interpretation of these selections.
First, all binaries and all compact object are retrieved from the simulation outputs. Then, correlating the two lists, all and only the binaries containing, at least once in their life, a star that is, or will become, a compact object, are retained. The other binaries are discarded to save space and speed up the analysis. Some of the binaries included in the data, at this point, may be non compact, e.g. may be a binary containing a star, that will become a BH when part of another binary. However, this choice allows me to trace the history of

the BHs and NSs from their first time in binary. I am able to know how many exchanges a BH experienced, how many binaries it belonged to and so on.
When dealing with the properties of the BH-BH binaries, it is necessary to choose when to pick up a binary during their life. Two choices are possible: (i) I can pick up the binary when its coalescence time is minimum, or (ii) when its semi-major axis is minimum. I found that choice (i) is a rather poor one, because the coalescence timescale $t_{\rm GW}$ depends on both the semi-major axis and the eccentricity, and both change during the binary evolution. Sometimes the eccentricity of a binary is very close to $e = 1$ when the binary forms, resulting in a short $t_{\rm GW}$. Then the binary evolves, circularizes and the coalescence timescale grows, to decrease again as the result of the semi-major axis shrinking by GW emission. Because of this trend, I choose to pick binaries at the moment of the minimum semi-major axis (choice ii). As a result, the coalescence timescale $t_{\rm GW}$ I obtain has a stronger physical meaning, representing a much more realistic time expected for the binary to merge.
In most of the results I distinguish between hard and soft binaries. The distinction is based on STARLAB criterion to classify a binary as stable or unstable presented in Sec. 3.5.
For this reason I may use hard and stable or soft and unstable as synonyms.

4.3 Results

4.3.1 Average number of BH-BH binaries per SC

Fig. 4.3 shows the average number of BH-BH binaries per SC. The top rows refers to all binaries, while the central and bottom one refer to the hard and soft binaries, respectively. Here, and in all the next plots, the separation between hard (stable) and soft (unstable) binaries always refers to the STARLAB criterion described in Chapter 3. The first thing we notice is that the global averages are mostly influenced by the soft binaries. The reason is that soft binaries undergo a lot of exchanges (see 4.3.6), thus the integrated number of soft binaries is

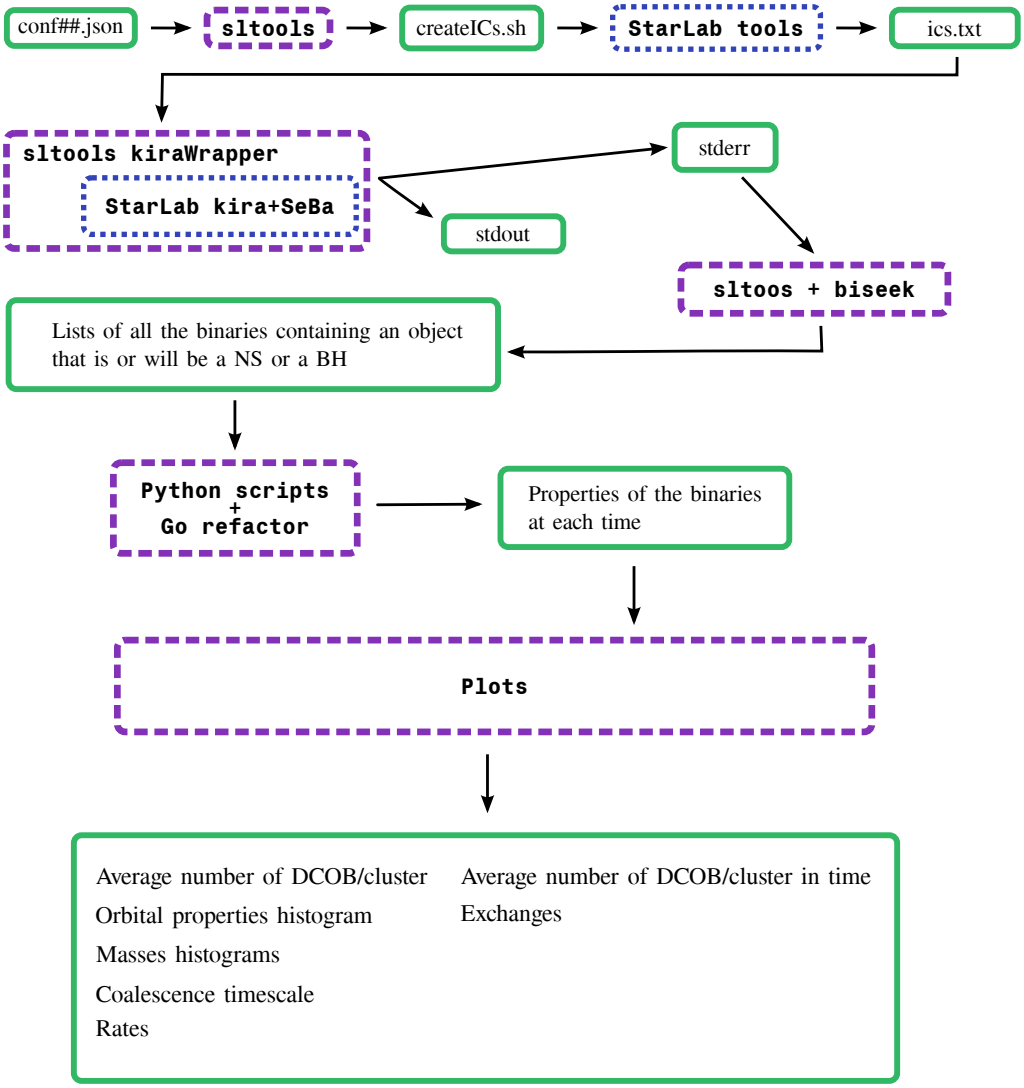

Figure 4.2: Scheme of the simulations and analysis pipeline showing the files (green solid rectangles), the codes I developed (violet dashed rectangles) and the codes already available I used (blue dotted rectangles). (From top to bottom) From the configuration file, stools produce the initial conditions scripts that are used as input by STARLAB tools to produce the initial conditions. These are read by kira (which I ran inside a wrapper in order to avoid bugged simulations). The simulation `stderr` are then checked and prepared with SLTOOL and parsed by `biseek` to generate lists of all the binaries containing an object that is or will be compact. These lists are joined and refactored to be read by the plotting scripts to produce the final plots.

higher (about three times) than the number of hard, stable, binaries.
We are more interested in the hard binaries, because soft binaries are (by definition) not good candidates for the emission of GW observable by Virgo/LIGO.
The uncertainties are derived propagating the (Poissonian) uncertainties on $n_{\rm DCOB}$ and $n_{\rm SC}$ and result

$$\frac{1}{n_{\rm SC,i}}\sqrt{n_{\rm i}(1+\langle n_{\rm i}\rangle)} \tag{4.1}$$

where i is the quantity over which I am marginalizing. This choice was made in order to take into account the uncertainty that comes from having simulated a certain number of YSCs instead of another.
From Fig. 4.3 we can see that the average number of hard BH-BH does not depend on the metallicity, while the average number of soft BH-BH is higher at $Z = 0.1\,{\rm Z}_\odot$ than at $Z = 1\,{\rm Z}_\odot$. The average number of soft BH-BH at $Z = 0.01\,{\rm Z}_\odot$ is consistent with the case $Z = 1\,{\rm Z}_\odot$.
A primordial binary fraction of 0.05 and 0.1 do not influence on the average number of BH-BH, while a noteworthy decrease can be seen for $f_{\rm PB} = 0.2$.
Finally, cluster models with very low concentration ($W_0 = 3$) have a number of hard BH-BH binaries smaller than the $W_0 = 5,9$ cases. Soft BH-BH binaries have a significant increase for $W_0 = 5$.
Fig. 4.4 shows the same quantities as in Fig. 4.3 but for the NS-NS binaries. The third column of Fig. shows that $\langle n_{\rm NS-NS}\rangle_{\rm SC}$ increases with the fraction of primordial binaries, unlike in the case of BH-BH binaries. The reason is that most of the BH-BH binaries come from dynamical interactions, thus a larger number of primordial binaries does not result in a larger average number of BH-BH binaries. On the contrary, most NS-NS binaries come from primordial ones because dynamical interactions are dominated by BHs. For this reason, the average number of NS-NS binaries reflects the primordial binary fraction.
Another interesting result is the lack of soft NS-NS binaries. This is due to the fact that NS-NS progenitors cannot survive the natal kick if they are too soft. Such binaries, if present, would be destroyed by the presence of BHs in dynamical encounters.

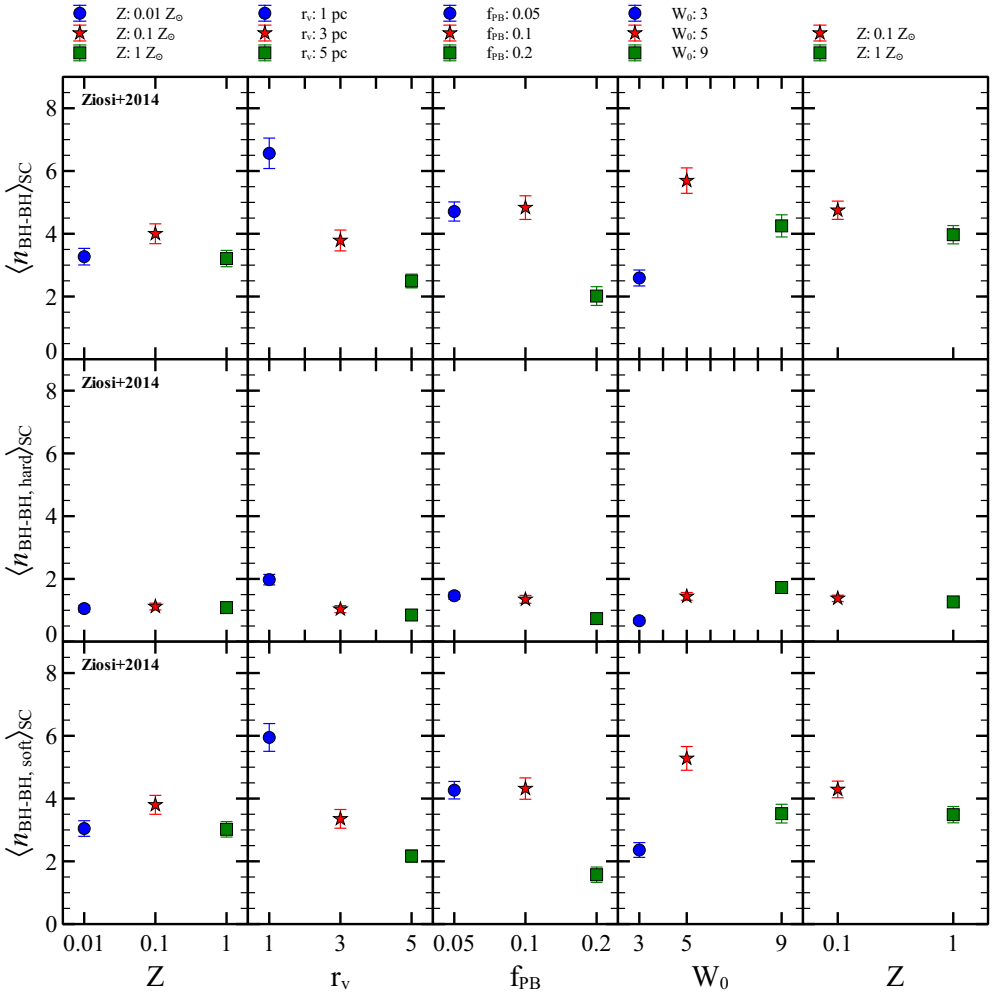

Figure 4.3: Average number of BH-BH binaries per SC. The top row shows the mean of all the BH-BH binaries, the central row shows only the hard binaries and the bottom panels show only the soft ones. The left most column shows the average of the simulations in Ziosi et al., 2014. From the second column to the last one on the right the averages of all the simulations of the second round of simulations are displayed, marginalized over the virial radius r_v, the fraction of primordial binaries f_{PB}, the central adimensional potential W_0 and the metallicity Z.

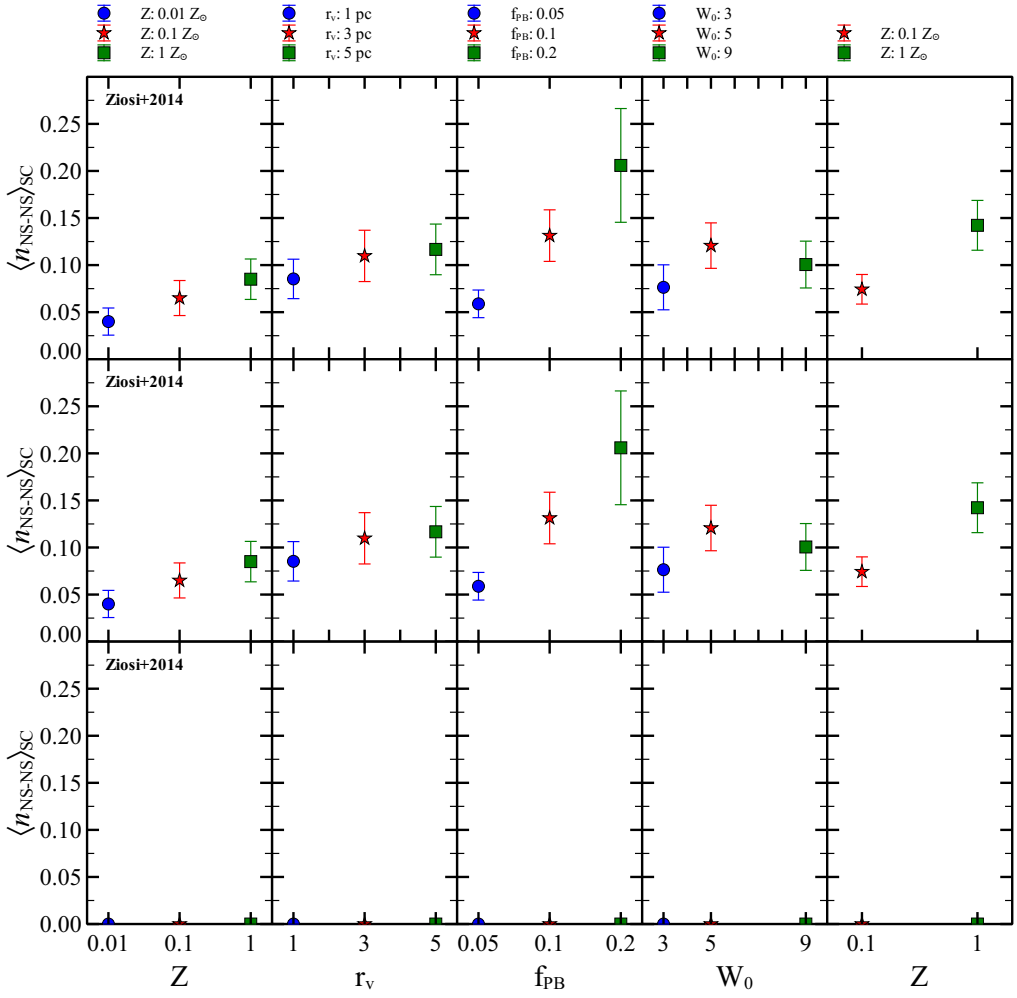

Figure 4.4: Same of Fig. 4.3 but for NS-NS binaries.

Moreover, from the last column in Fig. 4.4 we note that $\langle n_{\rm NS-NS}\rangle_{\rm SC}$ is larger at $Z = 0.1\,{\rm Z}_{\odot}$ than at $Z = 1\,{\rm Z}_{\odot}$.

The different values of $\langle n_{\rm NS-NS}\rangle_{\rm SC}$ for different initial virial radii and central adimensional potential are consistent within the uncertainties.

Finally, Fig. 4.5 shows the average number of BH-NS binaries. From this distribution, we see that BH-NS binaries follow approximately the same trends as NS-NS binaries, indicating that most of them come from primordial binaries

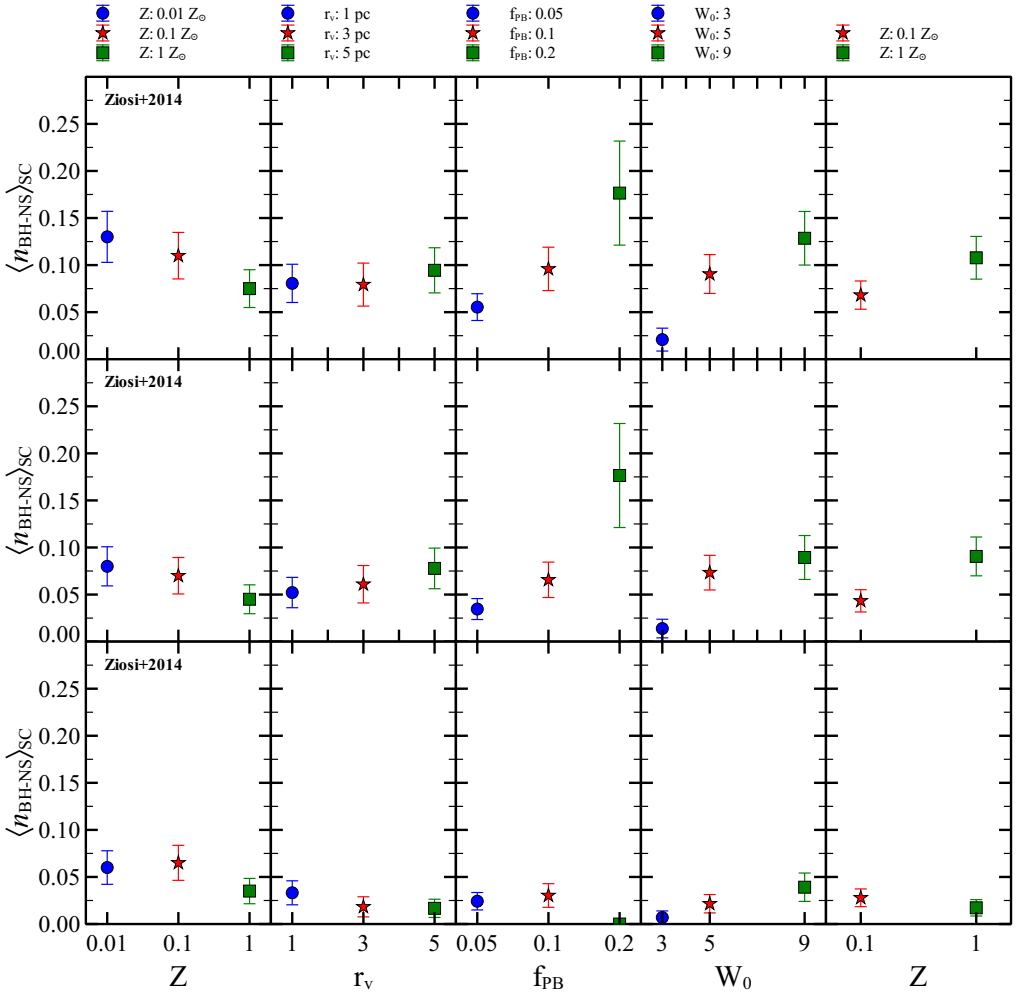

Figure 4.5: Same of Fig. 4.3 but for BH-NS binaries.

and are not much influenced by dynamics.

Fig. 4.6 shows the distribution of the number of hard BH-BH binaries per SCs, together with the average number and the KS test to compare the distribution coming from different values of the same parameter. Values of the KS test $p_{\rm KS} \ll 0.05$ mean that the two distribution are not drawn from the same underlying distribution.

My results show that the BH-BH binaries distributions for different metallicities

are very similar in the case of the simulations from Ziosi et al. (2014) ($p_{\rm KS} \sim 1$) and barely different in the case of the new ones ($p_{\rm KS} \sim 3 \times 10^{-2}$).

The virial radius (and thus the density) of the cluster appears to be a crucial parameter, given the very low probability (< 0.01) that the distribution with $r_{\rm v} = 1, 3$ and 5 are consistent with each other.

Almost the same result is found for the KS tests in the case of different W_0, where the distribution that is more different is the one for $W_0 = 3$.

YSCs with different primordial binary fractions result with BH-BH binaries distributions similar ($p_{\rm KS} \sim 1$) for $f_{\rm PB} = 0.05$ and 0.1 while the case $f_{\rm PB} = 0.2$ has a different shape ($p_{\rm KS} < 10^{-2}$).

4.3.2 Time evolution of the average number of BH-BH binaries per SC

Fig. 4.7 shows the evolution in time of the average number of BH-BH binaries per cluster. While the number of hard binaries steadily increases, the number of the soft ones has a peak after the core collapse and then decreases. This is a consequence of the fact that soft binaries are loose and unstable, easy to break. They increase after the core collapse as a consequence of the higher density. However, these binaries are soon destroyed by dynamical encounters. Hard binaries, on the other hand, once formed, tend to survive and accumulate. In Fig. 4.7 the left panel in the first row show the same plot of Fig. 3.2 but only for hard binaries. It can be seen that at $Z = 0.01\,{\rm Z}_\odot$ hard BH-BH binaries are formed earlier, followed by the simulations at $Z = 0.1\,{\rm Z}_\odot$ and finally $Z = 1\,{\rm Z}_\odot$. The right panel of the same row shows the three separated peaks in the BH-BH soft binaries, at 20, 25 and 30 Myr, followed by a decline. The bottom row shows the same results for the new simulations, and we can see that there is small difference between the $Z = 0.1\,{\rm Z}_\odot$ case (which end up with $\langle n \rangle_{SC}(t) \sim 0.3$) and the $Z = 0.1\,{\rm Z}_\odot$ one (which end up with $\langle n \rangle_{SC}(t) \sim 0.2$). The second row refers to $\langle n \rangle_{SC}(t)$ for hard (left-handed plot) and soft (right-handed plot) BH-BH binaries given the initial virial radius of the host YSC. The value of $\langle n_{\rm BH-BH} \rangle_{\rm SC}$

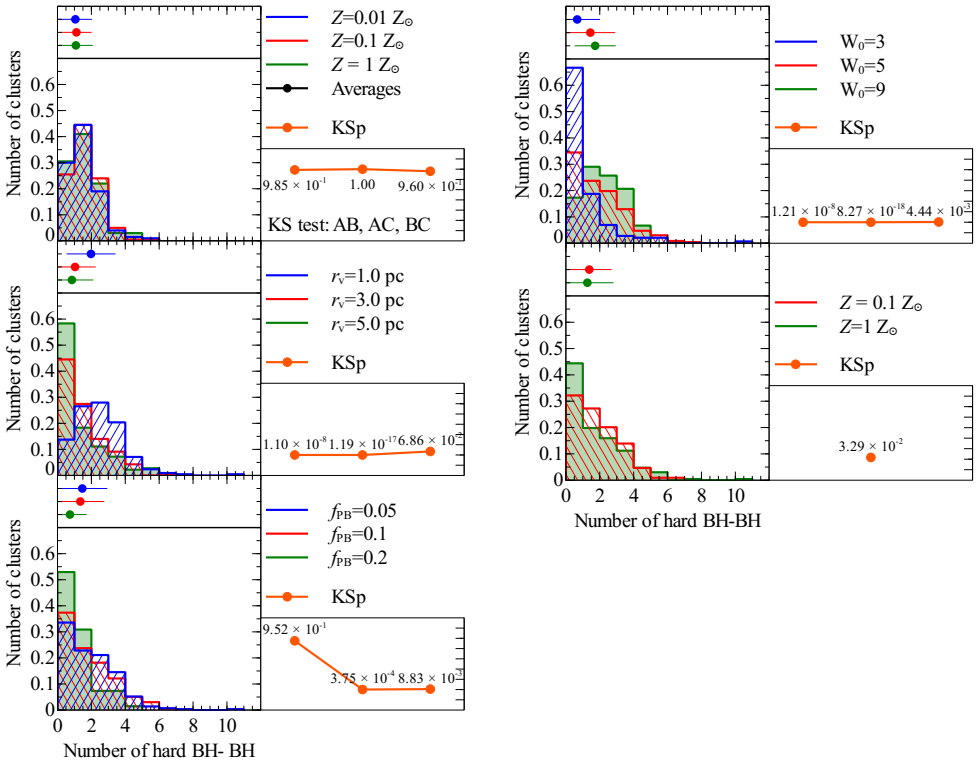

Figure 4.6: **Main panels:** distribution of the number of hard BH-BH binaries in clusters. **Top marginal panels:** average number of hard BH-BH binaries per cluster. **Right marginal panels:** KS test to compare the different distributions resulting from marginalizing on different values of the same parameter. The three values of the KS associated to the plots with three distributions refer to the result of the KS test comparing (i) the first and the second distributions (AB), (ii) the first and the third ones (AC) and the second with the third ones (BC).

at $r_v = 1\,pc$ is significantly above the other two cases, indicating that high density ($\sim 3 \times 10^3\,M_\odot pc^{-3}$) boosts the formation of (hard) BH-BH binaries. The final (at $t = 100\,Myr$) average number of hard BH-BH in the case at $r_v = 1\,pc$ is more than twice that of the cases at $r_v = 3,5\,pc$. Large differences can be seen also in the plot showing the soft BH-BH binaries. The other interesting result is for different values of W_0 (fourth row, left plot), where the evolution of the three cases is distinct and follows the concentration of the host YSC. $\langle n_{BH-BH}\rangle_{SC}(t)$ of hard BH-BH binaries for the case at $W_0 = 9$ is almost twice that of the case at $W_0 = 5$ and four times that of the case at $W_0 = 3$. This indicates that also a high concentration favors the formation of BH-BH binaries. The trends for the three f_{PB} show some differences, but they are consistent within the errors.

Fig. 4.8 shows the average number of hard NS-NS (left column) and hard BH-NS (right column) binaries as a function of time for comparison. It is worth noting the high value of $\langle n_{BH-NS}\rangle_{SC}(t)$ for hard BH-NS binaries at $f_{PB} = 0.2$. For both hard NS-NS and hard BH-NS binaries the average number of binaries at $Z = 1\,Z_\odot$ is almost always above the value for $Z = 0.1\,Z_\odot$. This is the opposite trend respect to BH-BH binaries.

4.3.3 Masses and orbital parameters

Fig. 4.9 shows the mass spectrum of the binaries, marginalized over the different parameters as in the previous sections.

From the second to the last rows, we notice the absence of high masses allowed at $Z = 0.01\,Z_\odot$, since this metallicity was not included in the new simulations. However, some BHs have masses up to $125\,M_\odot$ sun. This is due to the mergers with a stellar companion. However, it can be seen, in the last row, that because of the stellar evolution recipes, BHs at higher metallicities tend to have smaller masses.

Fig. 4.10 shows the chirp mass for the entire population of simulated BH-BH binaries. These are consistent with those obtained in Ziosi et al. (2014) for $Z = 0.1, 1 Z_\odot$.

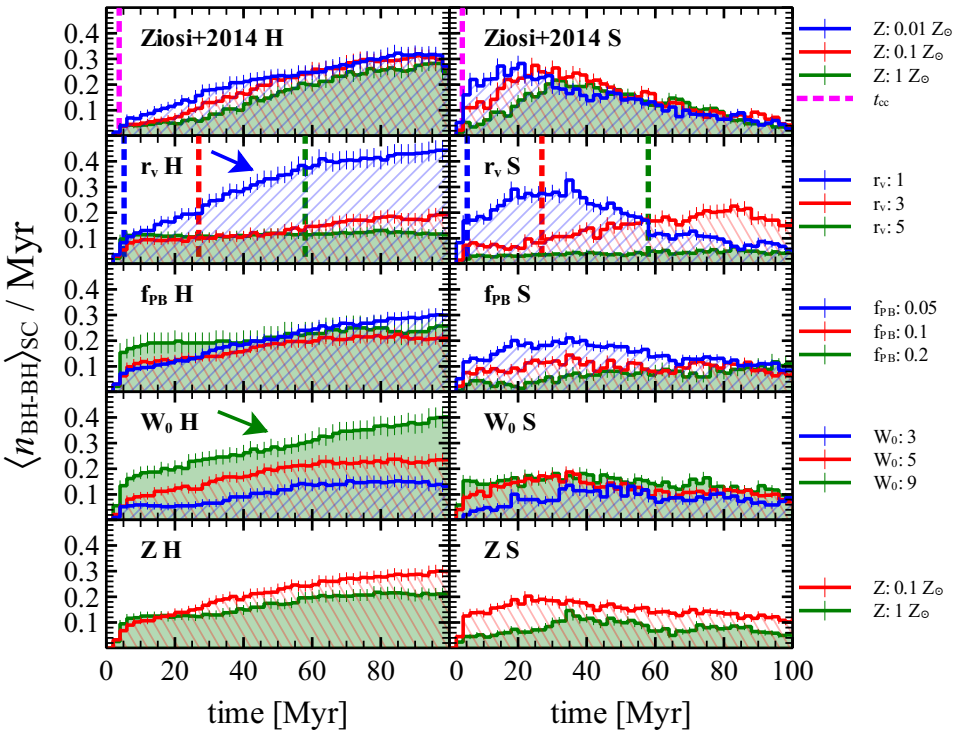

Figure 4.7: Time evolution of the average number of BH-BH binaries per SC. The first row refers to the simulations in Ziosi et al. (2014). The second to the last rows show the evolution marginalized over the virial radius $r_{\rm v}$, the fraction of primordial binaries $f_{\rm PB}$, the central adimensional potential W_0 and the metallicity Z respectively. The left column refers to the hard binaries (marked by a **H**), the right column to the soft ones (**S**). In all the plots the data were binned in $\Delta t = 2$ Myr. The vertical lines in the second topmost row show the time of the core collapse for different models (2.77, 14.38, 30.94 Myr, respectively). Error bars are computed according to those in Fig. 4.3.

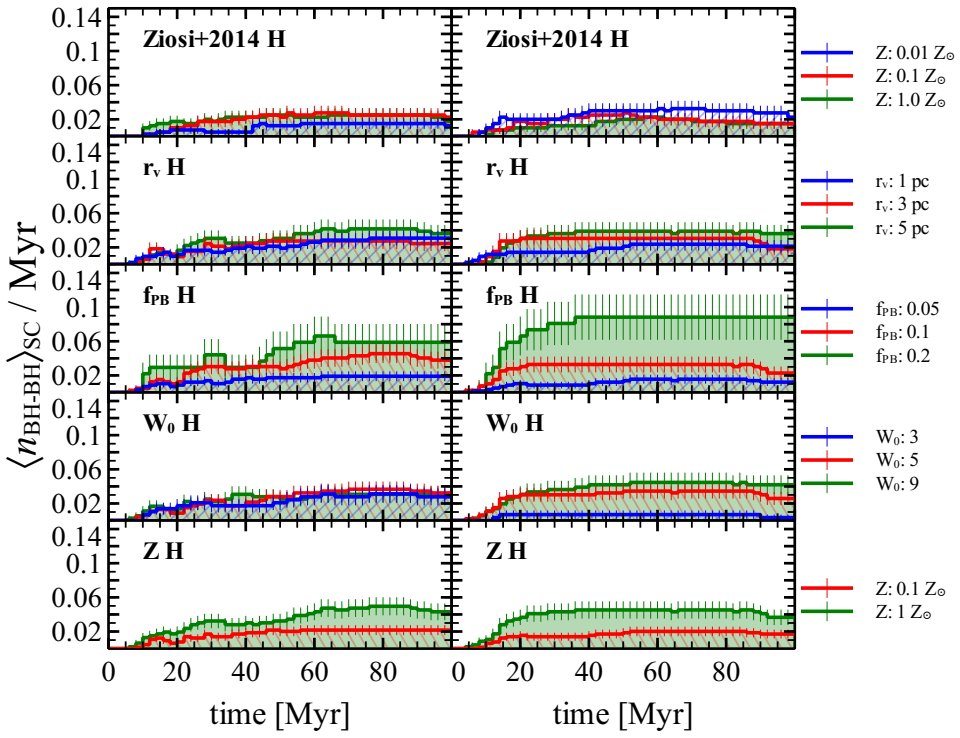

Figure 4.8: Time evolution of the average number of hard NS-NS binaries (left column) and hard BH-NS binaries (right column) marginalized over the virial radius r_V, the fraction of primordial binaries f_{PB}, the central adimensional potential W_0 and the metallicity Z respectively.

The left-hand column in Fig. 4.10 shows the chirp mass of the best merger candidates, i.e. the systems expected to merge within an Hubble time (see next Section).

Finally, the semi-major axis distributions are consistent with those already obtained in Ziosi et al., 2014 and discussed in Section 3.3.3.

4.3.4 Coalescence timescale

Fig. 4.12 shows the expected coalescence timescale, that is the time a binary needs to merge due to gravitational wave emission, for the BH-BH binaries.

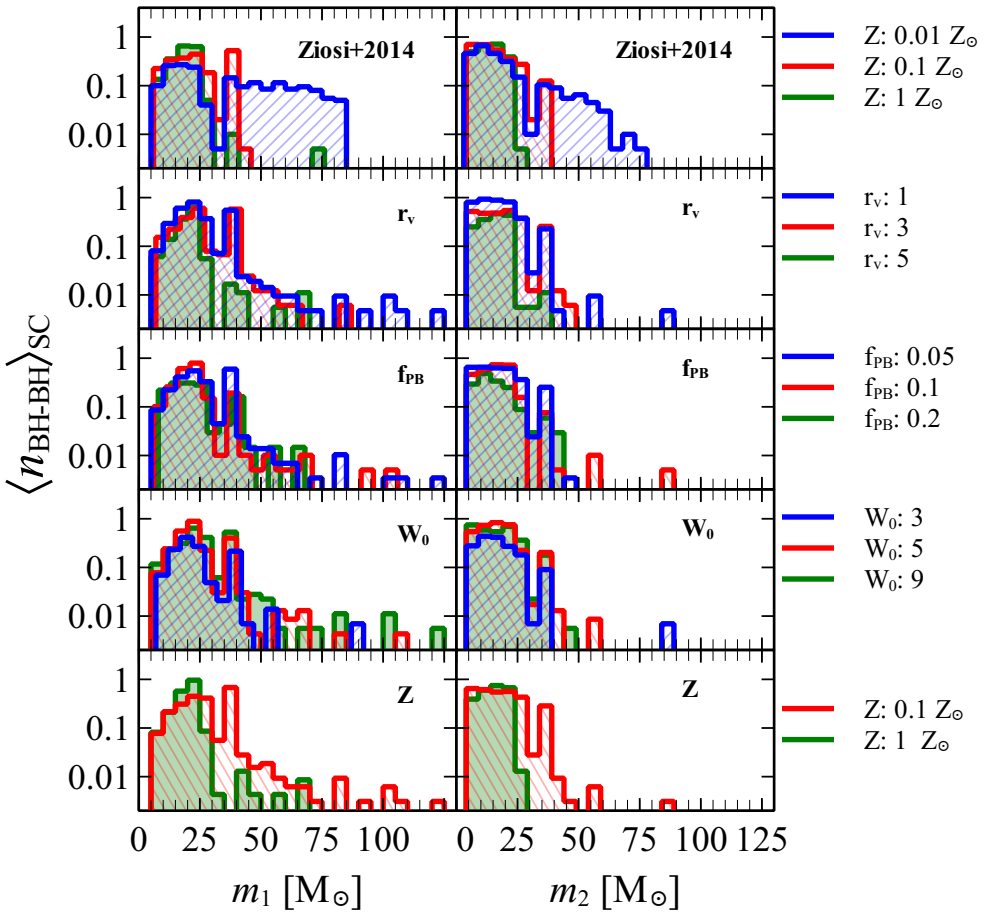

Figure 4.9: Mass distributions of the primary (m_1) and secondary ($m_2 < m_1$) components of the BH-BH binaries. The different plots show the binaries marginalized over the virial radius r_v, the fraction of primordial binaries f_{PB}, the central adimensional potential W_0, and the metallicity Z.

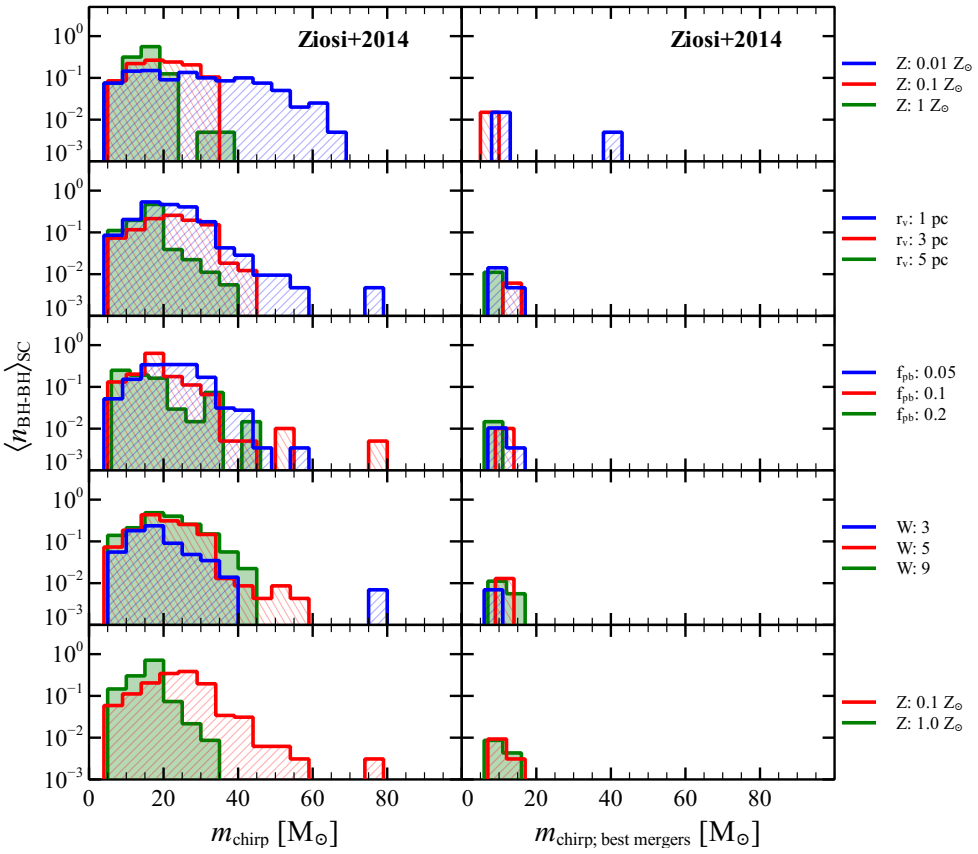

Figure 4.10: **Left column:** chirp masses of the simulated systems marginalized over the virial radius r_v, the fraction of primordial binaries f_{PB}, the central adimensional potential W_0 and the metallicity Z. **Right column:** chirp masses of the best merger candidates, marginalized in the same way.

It is worth noting that, except for the first panel, reporting the result already presented in Ziosi et al., 2014, all the panels show the same binaries: in each panel the same binaries are characterized by the marker shape and the color related to the host YSC model to make easier to understand to which model the BMCs belong and which model produces more of them.

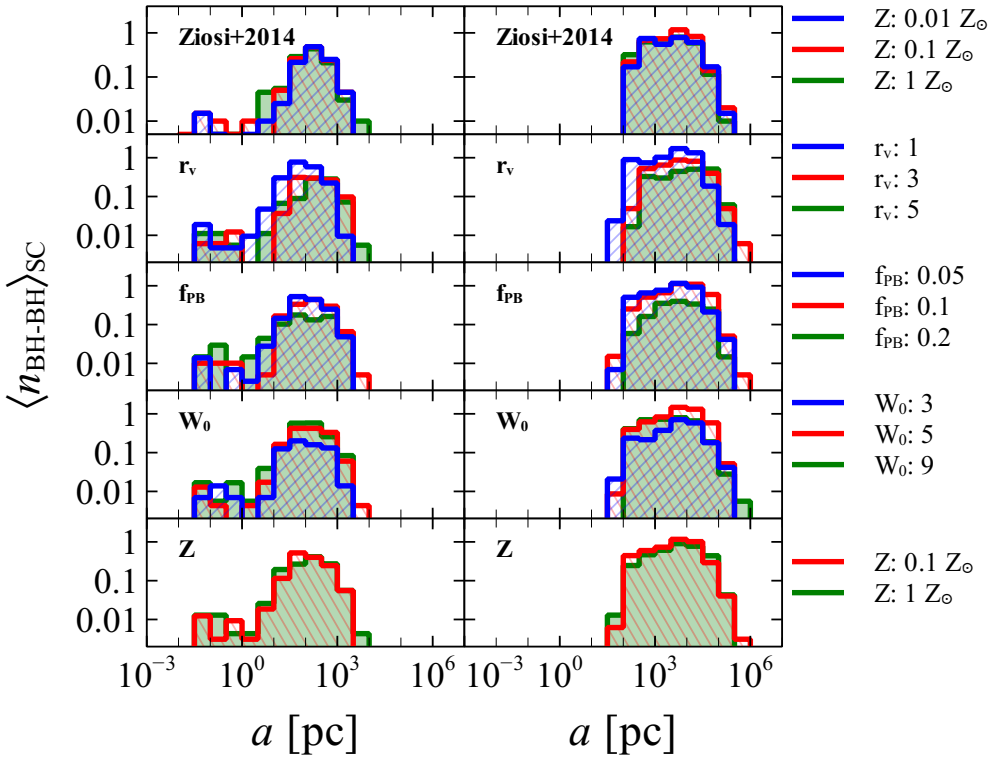

Figure 4.11: Semi-major axis of the stable and unstable binaries, marginalized over the virial radius r_v, the fraction of primordial binaries f_{PB}, the central adimensional potential W_0 and the metallicity Z.

4.3.5 Merger and detection rates

To obtain the merger rates, I updated the recipes adopted in Ziosi et al. (2014) with a formula similar to the one used in Esposito et al. (2015):

$$R_{merger} = \frac{t_{life}\rho_{SF}f_{SFSC}}{n_{SC}\langle M_{SC}\rangle}\sum\frac{1}{t_{obs}+t_{GW}} \tag{4.2}$$

where:

- $t_{life} = 100\,\mathrm{Myr}$ is the life of the simulated SCs
- $\rho_{SF} = 1.5\times10^{-2}\mathrm{M_\odot yr^{-1}Mpc^{-3}}$ is the cosmological density of SFR at redshift zero from Hopkins and Beacom (2006);

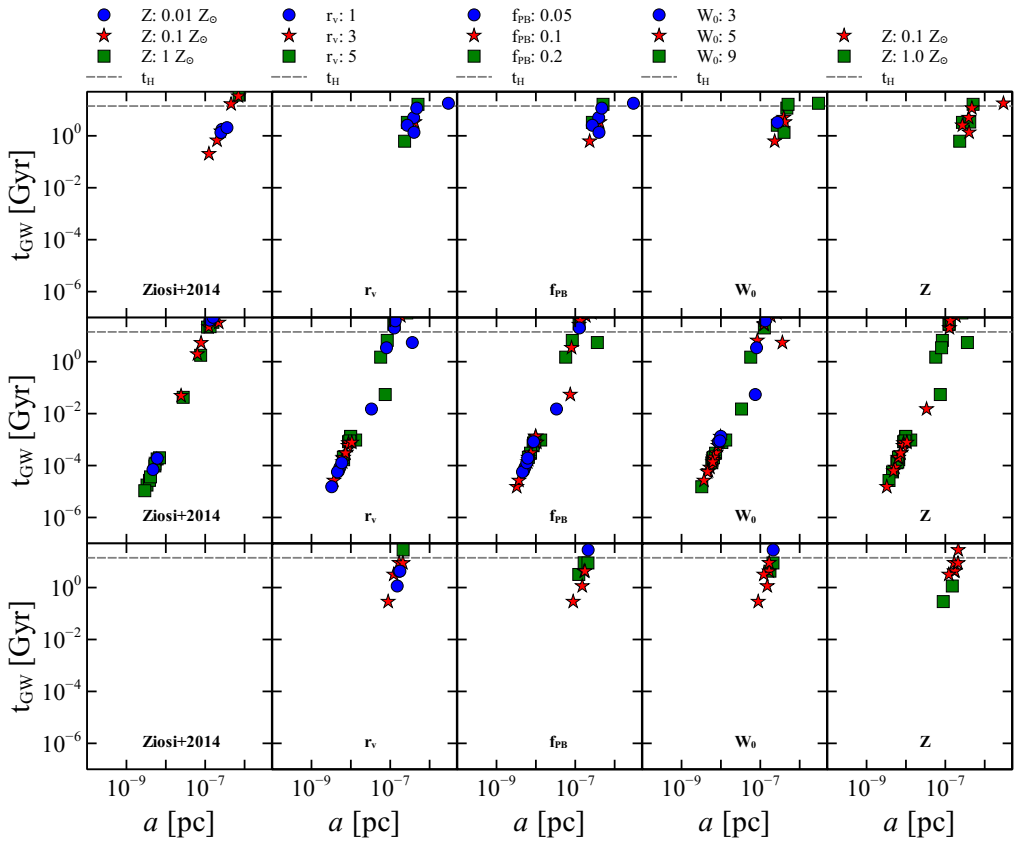

Figure 4.12: **First row:** coalescence timescale $t_{\rm GW}$ of the BH-BH binaries as a function of the semi-major axis. The first panel on the left shows the result published in Ziosi et al., 2014. From the second to the last panel, the binaries from the new simulations are shown, marginalized over the virial radius $r_{\rm v}$, the fraction of primordial binaries $f_{\rm PB}$, the central adimensional potential W_0 and the metallicity Z.. All the plots are cut above 14 Gyr to give a more clear view of the interesting candidates. Here all the binaries are represented, regardless they survive or not until the end of the simulation. **Second and third rows:** the same for NS-NS and BH-NS binaries.

- $f_{\rm SFSC} = 0.8$ is the fraction of star formation (SF) that occurs in YSCs form Lada and Lada (2003);
- $n_{\rm SC}$ is the number of simulated SCs for each model (see table 4.2;
- $M_{\rm SC}$ is the average mass of the SCs: 3500 $M_\odot$ for the simulations in Ziosi et al. (2014), 6700 $M_\odot$ for the new ones;
- $t_{\rm obs}$ is the time at which $t_{\rm GW}$ is calculated, here chosen to be the time at which the semi-major axis a is minimum, as explained in 4.2.2;
- t_{GW} is the coalescence timescale Peters (1964).

This new formula allows to better take into account the coalescence timescale of each binary. To obtain the detection rate $R_{\rm detection}$, I multiply the merger rate by the volume determined by the maximum distance at which mergers produce an observable GW signal. This distance depends on the chirp mass of each binary. Thus, the final formula, inspired by Belczynski et al. (2013), is:

$$R_{\rm detection} = V_{\rm horizon} R_{\rm merger} = \frac{4\pi}{3} \frac{t_{\rm life} \rho_{\rm SF} f_{\rm SFSC}}{n_{\rm SC} \langle M_{\rm SC} \rangle} \left(\frac{d_{\rm H,NS-NS}}{f} \right)^3 \frac{1}{m_{\rm c,NS-NS}^{15/6}} \sum \frac{m_{\rm c}^{15/6}}{t_{\rm obs} + t_{\rm GW}} \tag{4.3}$$

where $f = 2.26$ is a correction factor that takes into account the non-uniform pattern of detector sensitivity and random sky location and orientation of sources (Finn, 1996; Belczynski et al., 2013), $d_{\rm H,NS-NS}$ is the instrumental horizon for NS-NS merger observation, $m_{\rm c,NS-NS}$ is the assumed NS-NS chirp mass, m_c is the chirp mass of each single system.
The systems considered as best candidates, i.e. those with $t_{\rm GW} < 14$Gyr, are selected as those with $\frac{1}{t_{\rm obs}+t_{\rm GW}} > 0.0709 {\rm Gyr}^{-1}$.
Fig. 4.13 shows the final merger rates obtained. The merger rates for BH-BH binaries show almost no dependence on any of the properties of the YSC. NS-NS binaries, on the other hand, have a higher merger rate for $r_{\rm v} = 3\,$pc and $W_0 = 5$. The NS-NS merger rates also increase with the primordial binary

fraction (even though the uncertainty on $f_{\rm PB} = 0.2$ are quite large). Moreover, the merger rate for NS-NS binaries is higher at $Z = 1\,{\rm Z}_{\odot}$.

Merger rates for BH-NS binaries are higher at $r_{\rm v} = 3\,{\rm pc}$, $f_{\rm PB} = 0.1$, $W_0 = 5$ and $Z = 1\,{\rm Z}_{\odot}$.

Detection rates for BH-BH binaries are slightly higher at higher densities ($r_{\rm v} = 1\,{\rm pc}$), higher concentrations ($W_0 = 9$) and smaller primordial binary fractions ($f_{\rm PB} = 0.05$). They are also higher for intermediate metallicities ($Z = 0.1\,{\rm Z}_{\odot}$) respect to higher ones ($Z = 1\,{\rm Z}_{\odot}$), while they are lower for higher primordial binary fractions ($f_{\rm PB} = 0.2$). Uncertainties are quite large. Detection rates for NS-NS and BH-NS resemble the trends of merger rates.

The merger and detection rates for the old and the new simulations are listed with their errors (see next Section) in Tabs. 4.3 and 4.4, respectively.

Set	$R_{\rm merger}$ [Mpc^{-3} Myr^{-1}]	Error [Mpc^{-3} Myr^{-1}]
	BH-BH	
Ziosi et al. (2014)	0.004	0.002
Ziosi et al. 2015 (in prep.)	0.001	0.002
Global	0.0019	0.0007
	NS-NS	
Ziosi et al. (2014)	0.24	0.07
Ziosi et al. 2015 (in prep.)	0.267	0.008
Global	0.258	0.005
	BH-NS	
Ziosi et al. (2014)	0	1
Ziosi et al. 2015 (in prep.)	0.0014	0.0004
Global	0.0009	0.0002

Table 4.3: Merger rates for all the simulations considered in this work, calculated with the new formulas described in Section 4.3.5.

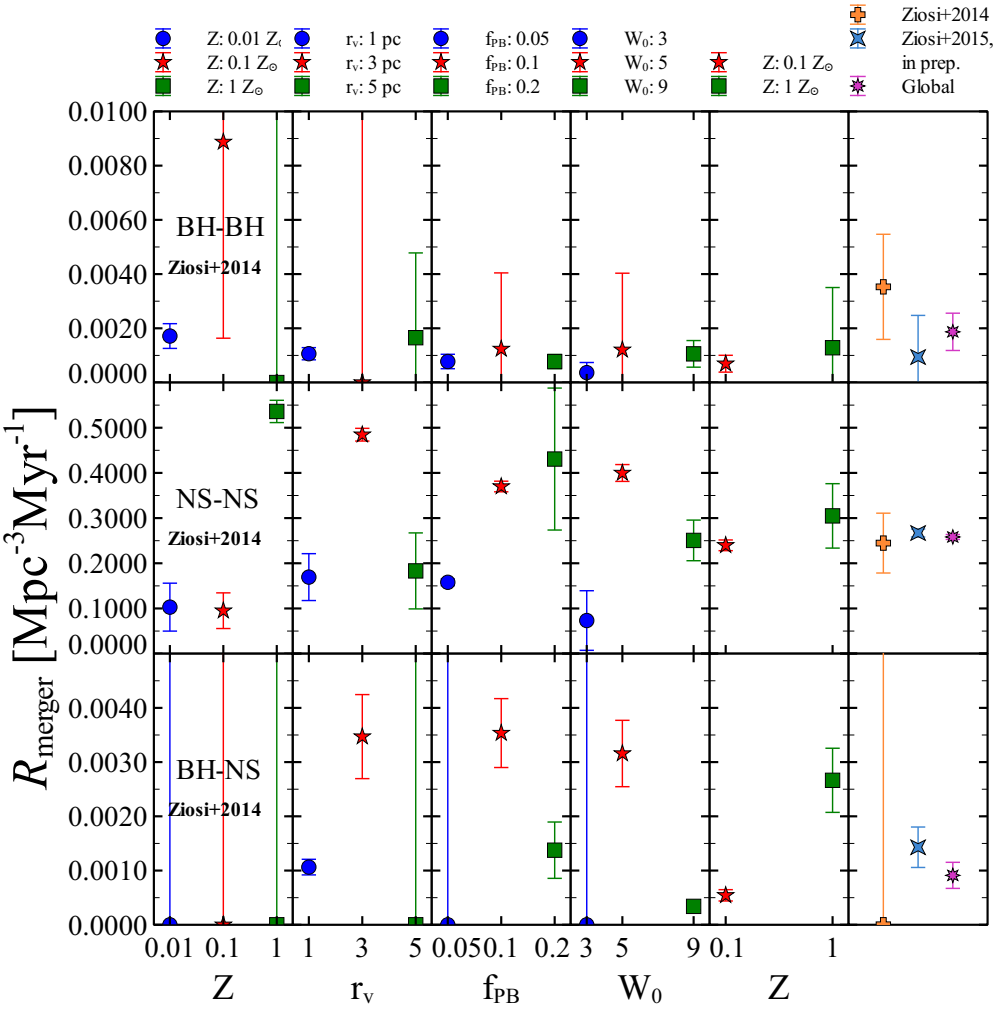

Figure 4.13: Merger rates for BH-BH binaries, NS-NS binaries and BH-NS binaries (from top to bottom) marginalized over the virial radius r_v, the fraction of primordial binaries f_{PB}, the central adimensional potential W_0 and the metallicity Z, respectively. The last column on the right shows the global rate for the two sets of simulations.

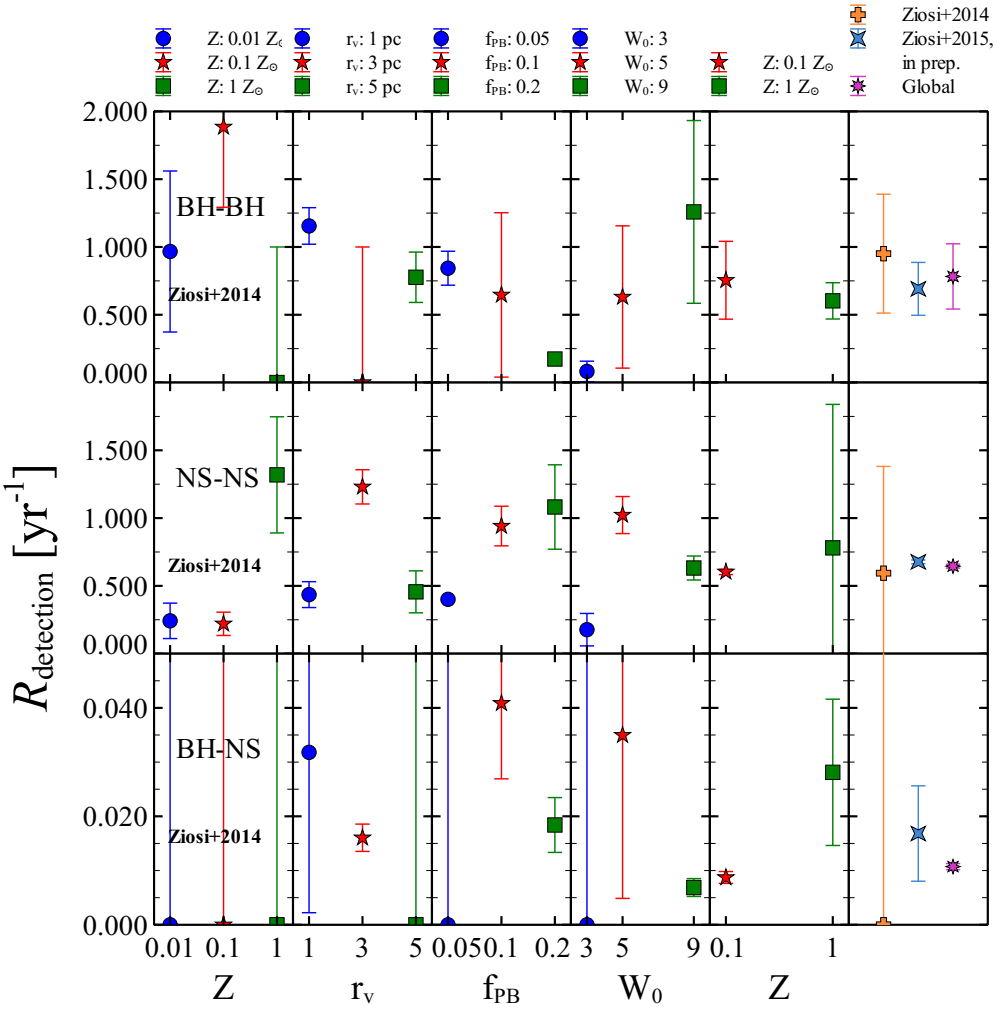

Figure 4.14: Detection rates for BH-BH binaries, NS-NS binaries and BH-NS binaries (from top to bottom) marginalized over the virial radius $r_{\rm v}$, the fraction of primordial binaries $f_{\rm PB}$, the central adimensional potential W_0 and the metallicity Z, respectively. The last column on the right shows the global rate for the two sets of simulations.

Set	$R_{\rm detection}$ [yr^{-1}]	Error [yr^{-1}]
	BH-BH	
Ziosi et al. (2014)	1.0	0.4
Ziosi et al. 2015 (in prep.)	0.7	0.2
Global	0.8	0.2
	NS-NS	
Ziosi et al. (2014)	0.6	0.8
Ziosi et al. 2015 (in prep.)	0.68	0.01
Global	0.65	0.01
	BH-NS	
Ziosi et al. (2014)	0	1
Ziosi et al. 2015 (in prep.)	0.017	0.008
Global	0.0107	0.0006

Table 4.4: Detection rates for all the simulations considered in this work, calculated with the new formulas described in Section 4.3.5.

Error estimation

Also the error estimation has been updated and is evaluated through a Monte Carlo approach. In particular, I adopt the following flowchart:

1. Compute the factors $\frac{1}{t_{\rm obs}+t_{\rm GW}}$ and $\frac{m_{\rm c}}{t_{\rm obs}+t_{\rm GW}}$ in the rates formulas;
2. Select those with $\frac{1}{t_{\rm obs}+t_{\rm GW}} > \frac{1}{0.1+14} = 0.0709{\rm Gyr}^{-1}$;
3. Compute the rates;
4. Evaluate the distribution of the factors $\frac{1}{t_{\rm obs}+t_{\rm GW}}$ and $\frac{m_{\rm c}}{t_{\rm obs}+t_{\rm GW}}$;
5. Fit the distribution with a two-Gaussian function;
6. Sample the fit 100 times for each distribution;
7. For each sampling the rates are computed from the factor over the threshold;

8. Evaluate the distribution of the "sampled" rates and take the standard deviation as error for the original rates.

In case a set is found with zero merger candidates, this can not be sampled. I decided to assign a error value of one, to be consistent with the rate evaluation adopted in Ziosi et al. (2014).
Fig. 4.15 shows a scheme of the error evaluation, while Figs. 4.16 and 4.17 show the results of the fitting, sampling and error estimation in detail for the global merger and detection rates of the simulated systems in Ziosi et al. (2014) and in the new simulations.

4.3.6 Exchanges

Figs. from 4.18 to **??** show some relevant quantities related to the dynamical exchanges involving BHs.
The BHs included in the sample are those that are found in a BH-BH binary at least once. They are traced since the first time they are found in a binary, regardless their type or the type of the binary.
For each of these BHs, I recorded:

1. the time they spent in binary, regardless its type or hardness
2. the time spent in hard BH-BH binaries
3. the time spent in soft BH-BH binaries
4. the total number of exchanges each BH (including the exchanges experienced by the BH progenitor) undergoes in its life
5. the number of exchanges to a hard binary, regardless of its type
6. the number of exchanges to a soft binary, regardless of its type

It is worth noting that the total time in binary does not correspond to the sum of the time in hard BH-BH binaries and the time spent in soft BH-BH binaries, because also the time in any non BH-BH binary is accounted.

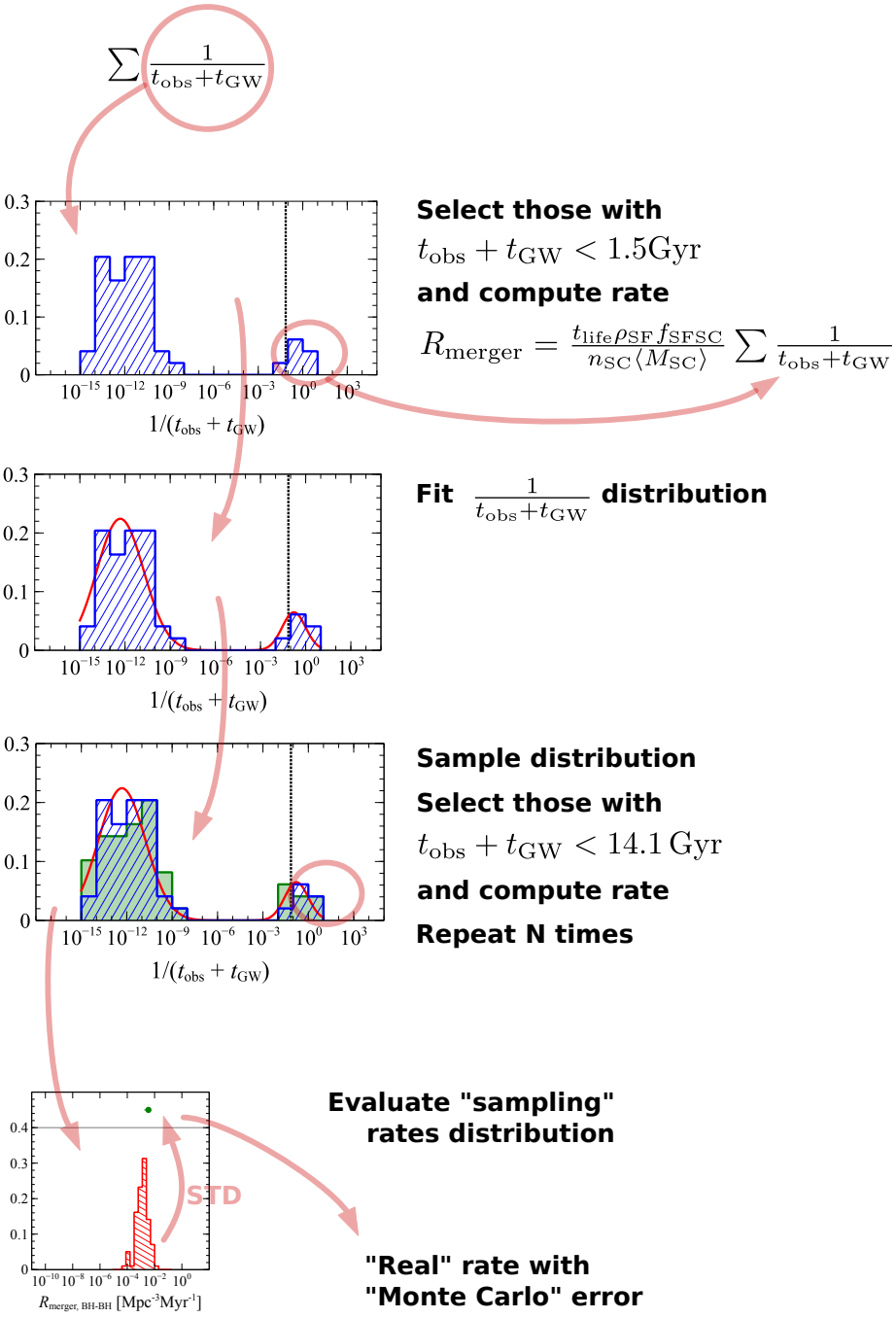

Figure 4.15: Scheme of the error evaluation for the merger rates. From top to bottom: distribution of the $\frac{1}{t_{obs}+t_{GW}}$ from simulations (blue histogram); analytical fit with a two-Gaussian function (red line); example of the synthetic data (green histogram) obtained fitting the distribution superimposed to the original distribution and to the fit; distribution of the merger rates obtained from the synthetic data (red histogram) compared to the merger rate obtained from the simulations (green dot).

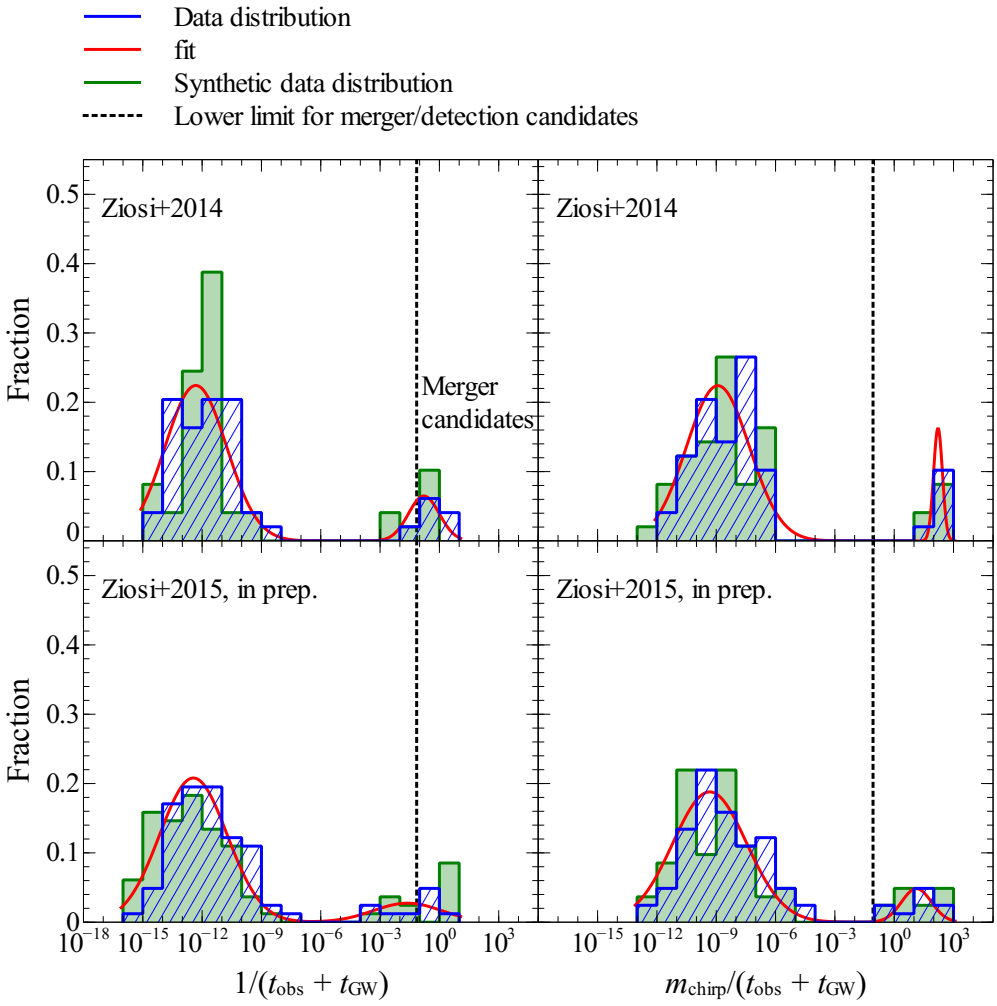

Figure 4.16: Distribution of the factors $\frac{1}{t_{obs}+t_{GW}}$ and $\frac{m_c}{t_{obs}+t_{GW}}$ obtained from the simulations, analytical fit with a two-Gaussian function and one of the N distributions of the sampling data. The first row refers to the data from Ziosi et al. (2014), the second row refers to the new simulations. The left column refers to the merger rate, the column on the right to the detection rate. Data is not marginalized.

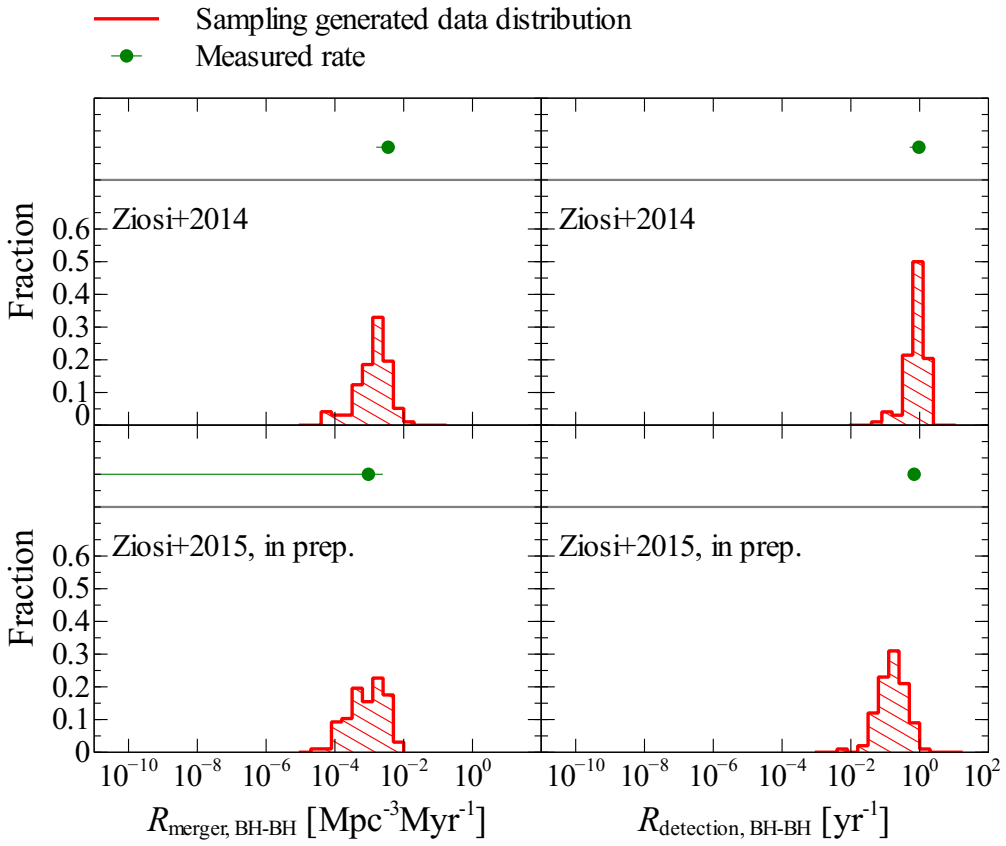

Figure 4.17: The red histograms are the distribution of the merger (left-handed panels) and detection (right-handed panels) rates from the synthetic data. The green dots are the merger and detection rates coming from the simulated clusters. The error bars on the green dots are the standard deviations of the blue histograms. As in Fig. 4.16 the first row refers to Ziosi et al. (2014) while the second row refers to the new simulations. Data is not marginalized.

This choice was made in order to estimate the time spent in a certain type of binary, but also to estimate the number of exchanges a certain object experienced in its whole life, that is, how dynamically active it has been.
Note that if a binary is disrupted, (at least) one of the two components forms a new binary and then a binary with the same object as the first binary is created, this is considered a new binary. In other words, a single binary is not only determined by its components but also by the fact that it has not been ionized ionized.
Figs. 4.18 and 4.19 investigate the different properties of DCOB exchanges.
Fig. 4.18 shows the average time a BH spent in binaries versus the total time it spent in binaries. The average time is calculated as the total time the BH spent in binaries divided by the number of binaries it was member of. Data points tend to arrange in lines. The first line (the one with inclination of 45°) corresponds to BHs that spent their entire life in binaries (zero exchanges): their average time in binary is exactly the same as the total time. A BH which has been member of two binaries will be found in the second line (with inclination of 22.5°) because its average time in binary is half the total time in binary, and so on. Hard binaries tend to lack smaller ratios between the average time in binary and the total time in binary.
Fig. 4.19 shows the total number of exchanges versus the total time in binary. Hard binaries have very low values of the total number of exchanges while they have a wide range of values for the total time in binary. Soft binaries tend to have more exchanges together with shorter total times in binary.

4.3.7 Comparison with the observations of NS-NS binaries

Fig. 4.20 shows period, eccentricity and coalescence timescale of the observed NS-NS binaries (Lorimer, 2008). These binaries have been observed thanks to the fact that at least one of the members of the binary is a pulsar. The analysis of the time of arrival (TOA) of the pulsar signal enables to derive the presence of a second object and the orbital properties (and masses). The data from these binaries is in good agreement with the NS-NS data from our simulated clusters,

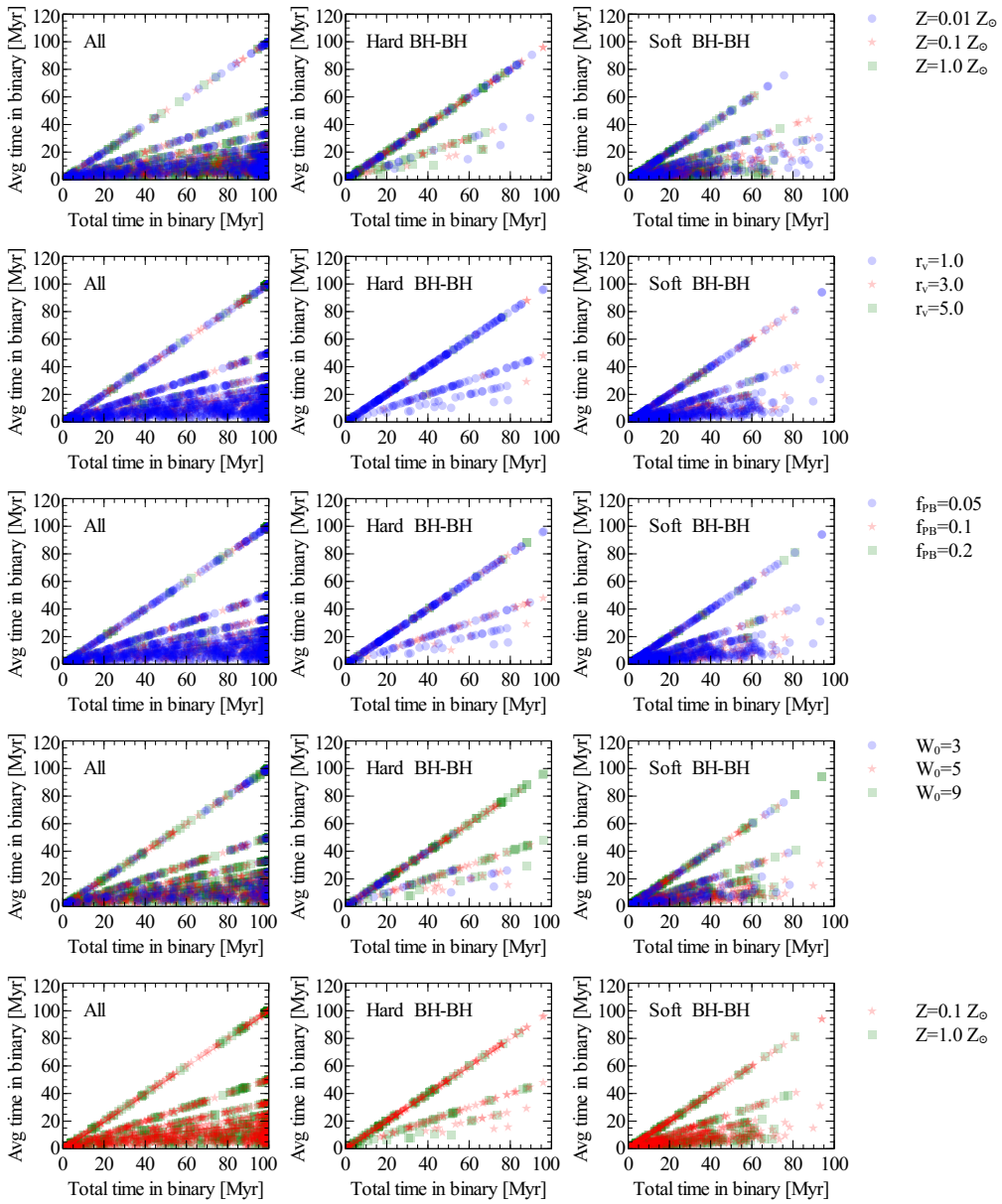

Figure 4.18: Average time spent in binary by each BH as a function of the total time spent in binary. In the first column the total time is calculated from the first time the BH (or its progenitor) is found in a binary, regardless of the evolutionary phase of the BH progenitor of the other component of the binary. The second and the third column, instead, consider only the time a BH-BH spent in a hard BH-BH binary or in a soft BH-BH binary. The first row refers to the simulations analyzed in Ziosi et al. (2014). Rows from the second to the last one show the BHs found in the new simulations. Each row considers the simulations marginalized over r_v, $f_{\rm PB}$, W_0, Z. Different colors indicate BHs belonging to simulations with different values of the chosen property.

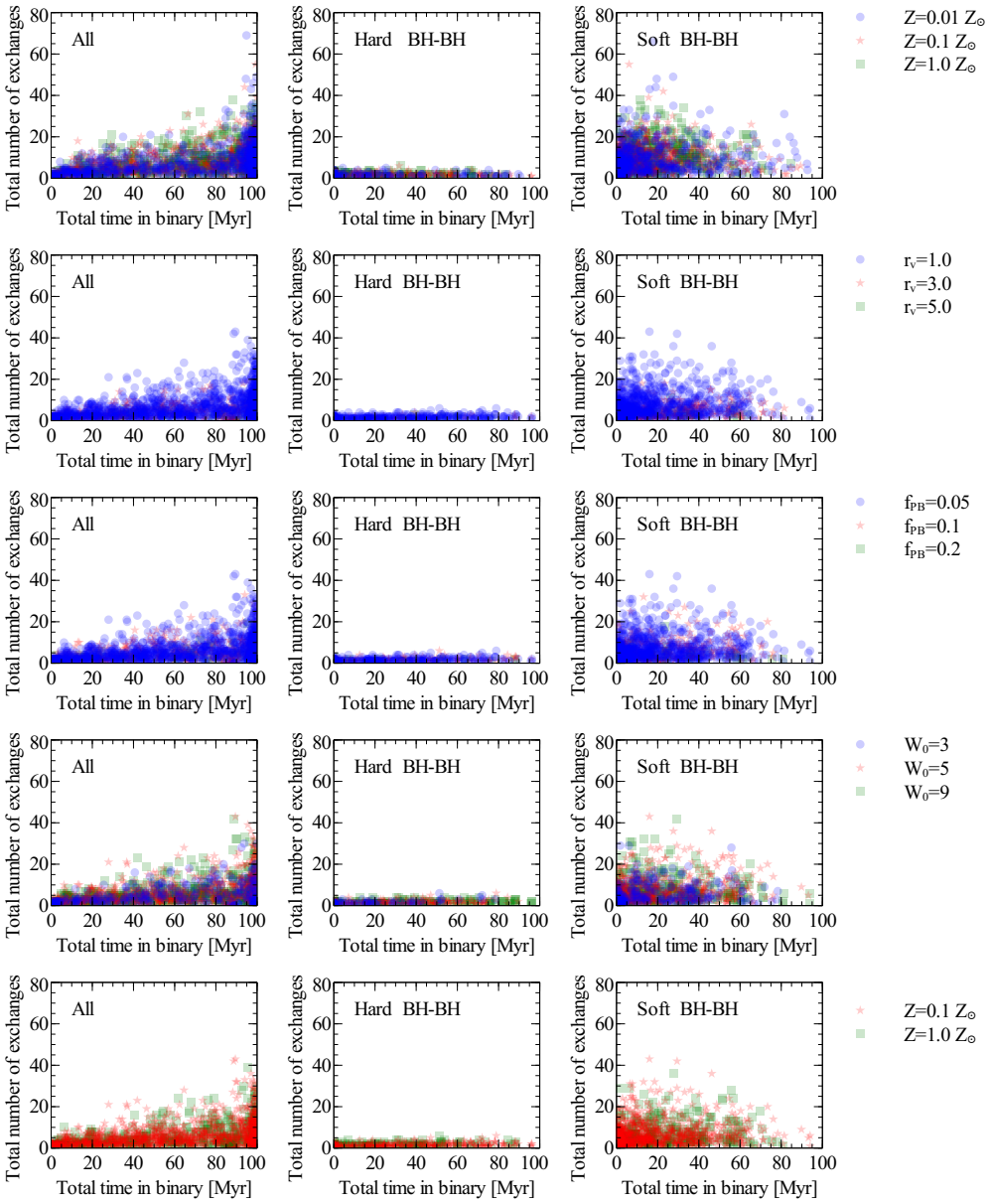

Figure 4.19: Total number of exchanges as a function of the total time in binary. The first column shows the total time an object spent being a binary member, regardless of the hardness of the type of the binary. The other column refers to the time spent in hard BH-BH or soft BH-BH binaries.

without making any assumption. The only small discrepancy is represented by the fact that the simulated NS-NS at very short and very long periods, do not correspond to an observed group of NS-NS in the same regions. The explanation is that at very short periods ($\lesssim 10^2$ s) the NS-NS have very short coalescence timescales ($\lesssim 1000$ yr), thus they merge in very short time resulting in a very small probability of being observed. Very long periods, instead, are too long ($\gtrsim 10^5$ yr) to permit an observation.

Name	P_{pulsar} [ms]	P_{binary} [d]	e	meas. M	t_{GW} [yr]
J0737-3039	2750.0	0.1	0.09	Yes	7.94+07
J1518+4904	40.9	8.6	0.25	No	2.51+12
B1534+12	37.9	0.4	0.27	Yes	2.51+09
J1756-2251	28.5	0.3	0.18	Yes	1.58+10
J1811-1736	104.2	18.8	0.83	Yes	1.00+13
B1820-11	279.8	357.8	0.79	No	6.31+15
J1829+2456	41.0	1.2	0.14	No	6.31+10
J1906+0746	144.1	0.2	0.09	Yes	3.16+08
B1913+16	59.0	0.3	0.62	Yes	3.16+08
B2127+11C	30.5	0.3	0.68	Yes	2.00+08

Table 4.5: Name, pulsar period, orbital period, eccentricity, flag to indicate if the masses were measured or not and t_{GW} of the observed NS-NS binaries.

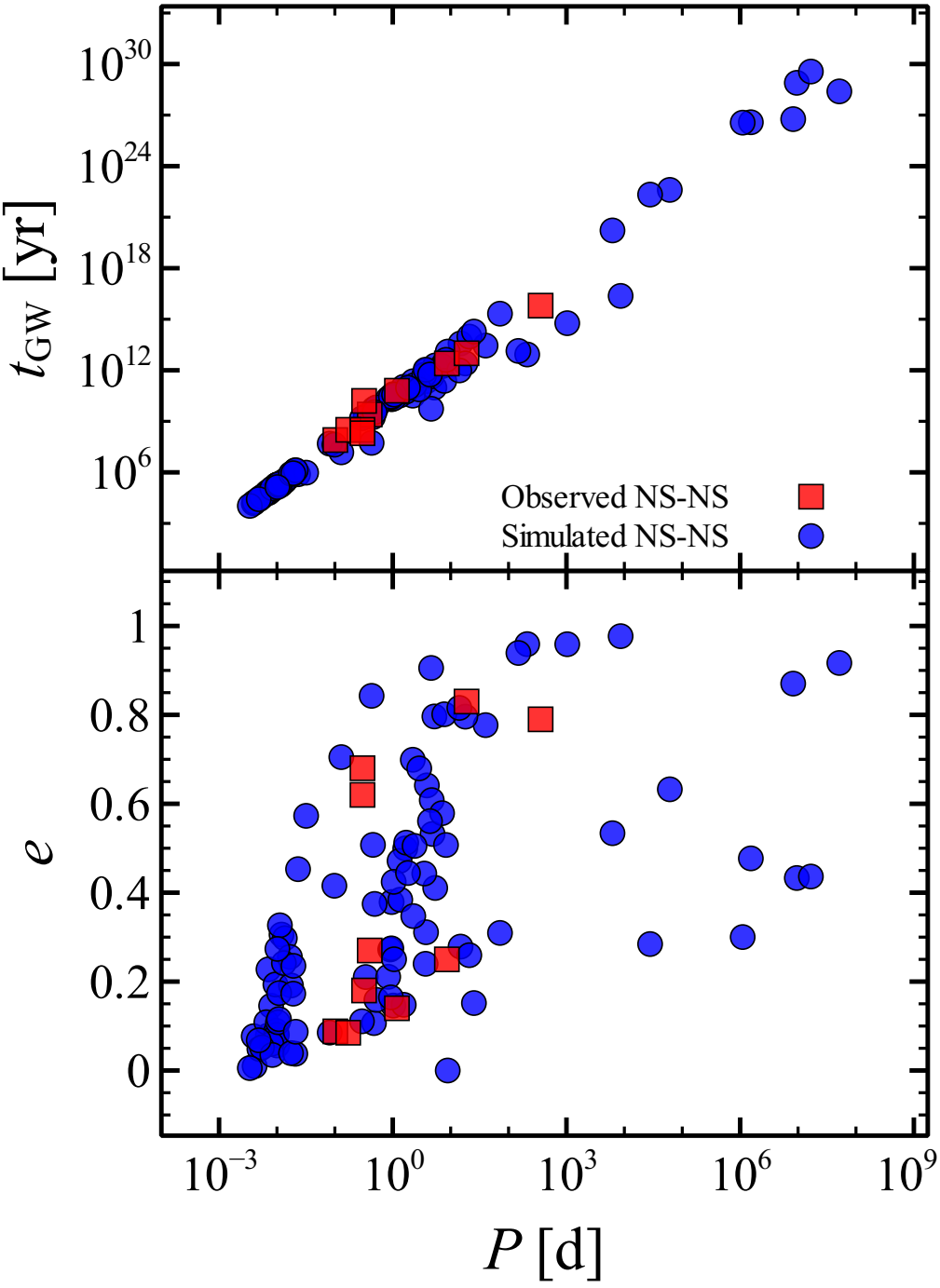

Figure 4.20: Period, eccentricity and coalescence timescale of the observed NS-NS binaries containing at least one pulsar (red square) compared (as in Fig. 1.9) with the simulated one (blue circles).

CHAPTER 5

GALACTIC TIDAL FIELD

YSCs do not evolve in isolations. They live in galaxies and their spatial distribution resembles that of the star formation regions, in particular they tend to distribute on the Galactic plane (see Fig. 5.1). The results I presented in the previous chapters rely on simulations of YSCs in isolations. Neglecting the tidal field might lead to dramatically overestimate the cluster lifetime, and thus the impact of the dynamics on the formation of DCOBs. Recently, Madrid, Hurley, and Martig, 2014 described the effects of a disk potential on globular clusters on different orbits: coplanar with the galactic disk, inclined or perpendicular. My aim is to extend their analysis to young dense SCs and to investigate the effect of a tidal field resembling that of the Milky Way on the formation and evolution of DCOBs.

In particular, I am interested in the case in which the cluster is not on a circular orbit coplanar with the galactic disk, but on an eccentric and inclined one. In this case, the potential changes rapidly with time, and the effect on the cluster can be much more effective. In fact, the rapid change of an external gravitational field causes a so called a tidal shock. This accelerates the stars

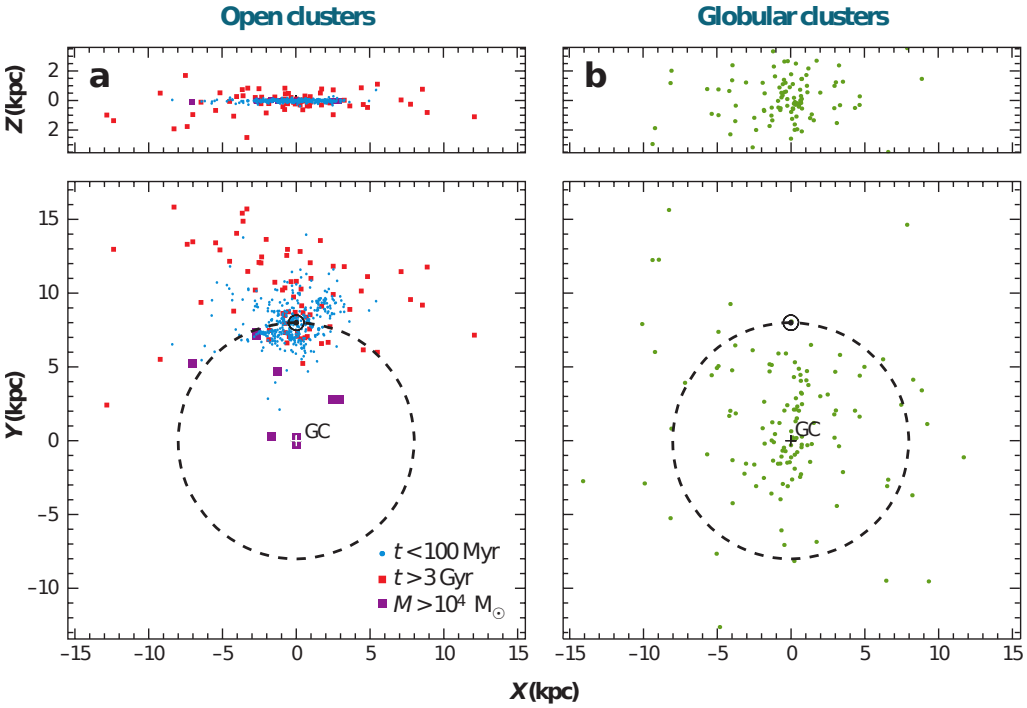

Figure 5.1: (a) Distribution of young (<100 Myr, filled blue circles) and old (>3 Gyr, filled red squares) open clusters in the Galactic plane, based on the catalog of Dias et al. (2002). The old open clusters are found preferentially toward the Galactic anti-center and above the plane compared to the young open clusters. The young massive clusters (purple squares) are located within the solar circle, which is probably a selection effect caused by the higher star-formation rate (per unit area) toward the Galactic center. (b) Distribution of old globular clusters; data from the Harris (1996) catalog. (From Portegies Zwart, McMillan, and Gieles, 2010)

in the outer part of the cluster. The cluster responds expanding and several stars can trespass the tidal radius being stripped by the host galaxy. Other consequences are the acceleration of the core collapse and the decrease of the cluster lifetime (Aguilar, Hut, and Ostriker, 1988, Murali and Weinberg, 1997b, Murali and Weinberg, 1997a, Gnedin, Lee, and Ostriker, 1999).

In Section 5.1 I describe the tidal field we implemented in STARLAB, while Section 5.2 discusses actual implementation of the tidal field in STARLAB.

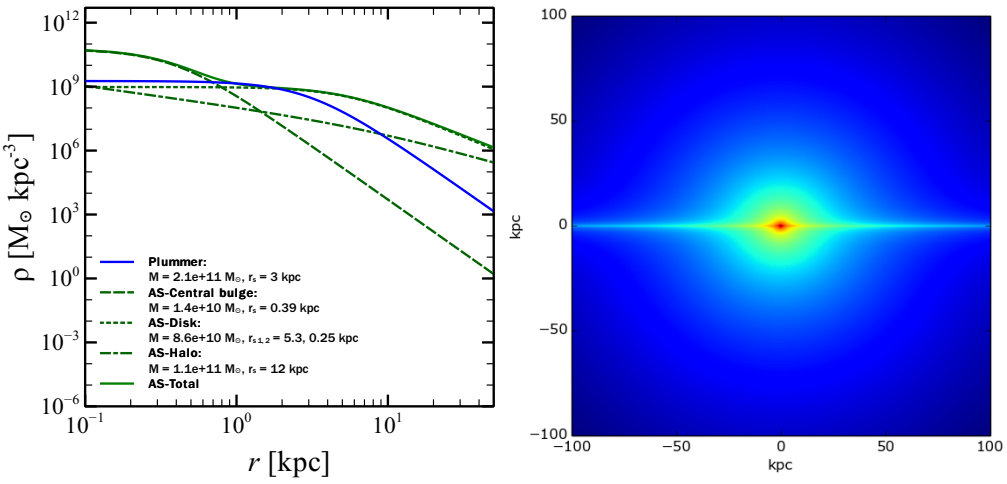

Figure 5.2: Radial density profile and colormap of Allen and Santillan (1991) galactic tidal field compared to the a Plummer sphere with the same total mass $M = 2.1 \times 10^{11}\,\mathrm{M}_\odot$. The parameters for the Allen and Santillan, 1991 tidal field are: **Bulge:** mass $M = 1.4 \times 10^{10}\,\mathrm{M}_\odot$, scale radius $a_1 = 0.39\,\mathrm{kpc}$; **Disk:** mass $M = 8.6 \times 10^{10}\,\mathrm{M}_\odot$, scale radii $a_2 = 5.3\,\mathrm{kpc}$, $b_2 = 0.25\,\mathrm{kpc}$; **Halo:** mass $M = 1.1 \times 10^{11}\,\mathrm{M}_\odot$, scale radius $b_3 = 12\,\mathrm{kpc}$.

5.1 Allen-Santillan tidal field

The public version of STARLAB includes a Plummer spherical tidal field, that does not fit our purposes. To reproduce the potential of the Milky Way, Dr. Mario Spera and I implemented the Allen and Santillan (1991) model in STARLAB. The Allen and Santillan (1991) model describes a potential composed of three parts: a (Plummer) bulge, a dark halo and a disk. It was developed to describe the potential of a Milky Way-like galaxy. The model aim is to be as accurate as possible while being analytic and very easy to manage. This means that it can be easily implemented in a code to simulate the dynamics of a galaxy and it does not slow down the code significantly.

Plummer bulge

This component is exactly the same as that presented in 2.2.1, it is repeated here only for consistency. However, while the potential form is the same, the scale parameter and the total mass would have a different value in a realistic case, to describe a part of a galaxy instead of an entire galaxy.

$$\phi_1(R) = -\frac{GM_1}{(R^2+b_1^2)^{1/2}} \tag{5.1}$$

$$M_1(R) = \frac{\nabla\phi_1(R)}{G} = M_1\frac{R^3}{\left(R^2+b_1^2\right)^{3/2}} \tag{5.2}$$

$$\rho_1(R) = \frac{\nabla^2\phi}{4\pi G} = \frac{3b_1^2M_1}{4\pi(R^2+b_1^2)^{5/2}} \tag{5.3}$$

$$a_{1i}(R) = -\frac{x_iGM_1}{(R^2+b_i^2)^{3/2}} \tag{5.4}$$

$$j_i(R) = -\frac{GM_1}{(R^2+b_1^2)^{3/2}}\left[v_i - \frac{3x_i(\mathbf{x}\cdot\mathbf{v})}{R^2+b_1^2}\right] \tag{5.5}$$

where $R = \sqrt{x_1^2+x_2^2+x_3^2}$, $\phi_1(R)$, $M_1(R)$, $\rho_1(R)$, $a_{1i}(R)$, $j_{1i}(R)$ and b are the radius, the potential, the enclosed mass, the density, the acceleration, the jerk and the scale radius in the Plummer model. The subscript i in the acceleration and jerk refers to the $i-$th coordinate.

Miyamoto&Nagai disk

The disk potential of the Allen and Santillan (1991) is derived from the Miyamoto and Nagai (1975) disk that, in turn, is a modified Plummer model. It is described by:

$$\phi_2(r,x_3) = -\frac{GM_2}{\left\{r^2+\left[a_2+\left(x_3^2+b_2^2\right)^{1/2}\right]^2\right\}^{1/2}} \tag{5.6}$$

$$\begin{aligned} M_2(r,x_3) &= \frac{\nabla\phi_2(r,x_3)}{G} = \frac{r^2}{G}\frac{\partial\phi_2(r,x_3)}{\partial r} + \frac{x_3^2}{G}\frac{\partial\phi_2(r,x_3)}{\partial x_3} \\ &= \frac{M_2\left\{\left(b_2^2+x_3^2\right)^{1/2}r^3 + x_3^3\left[a_2^2+(b_2^2+x_3^2)^{1/2}\right]\right\}}{\left\{r^2+\left[a_2^2+\left(b_2^2+x_3^2\right)^{1/2}\right]^2\right\}^{3/2}} \end{aligned} \tag{5.7}$$

$$\rho_2(r,x_3) = \frac{b_2^2M_2}{4\pi}\frac{a_2r^2+\left[a_2+3\left(x_3^2+b_2^2\right)^{1/2}\right]\left[a_2+\left(x_3^2+b_2^2\right)^{1/2}\right]^2}{\left\{r^2+\left[a_2^2+\left(x_3^2+b_2^2\right)^{1/2}\right]^2\right\}^{5/2}\left(x_3^2+b_2^2\right)^{3/2}} \tag{5.8}$$

$$a_{2i} = -\frac{x_1GM_2}{\left\{R^2-x_3^2+\left[a_2+\left(b_2^2+x_3^2\right)^{1/2}\right]^2\right\}^{3/2}}\left[1,1,\left(1+\frac{a_2}{(b_2^2+x_3^2)^{1/2}}\right)\right] \tag{5.9}$$

$$\begin{aligned} j_{2i} = &\frac{x_iGM_2}{\left\{R^2-x_3^2+\left[a_2+\left(b_2^2+x_3^2\right)^{1/2}\right]^2\right\}^{3/2}}\left[\frac{v_i}{x_i}-3\frac{\mathbf{x}\cdot\mathbf{v}+\frac{a_2}{(b_2^2+x_3^2)^{1/2}}x_3v_3}{\left\{R^2-x_3^2+\left[a_2+\left(b_2^2+x_3^2\right)^{1/2}\right]^2\right\}}\right]\times \\ &\times\left[1,1,\frac{(b_2^2+x_3^2)^{1/2}+a_2}{(b_2^2+x_3^2)^{1/2}}\right]-\left[0,0,\frac{x_3a_2GM_2}{\left\{R^2-x_3^2+\left[a_2+\left(b_2^2+x_3^2\right)^{1/2}\right]^2\right\}^{3/2}}\frac{x_3v_3}{(b_2^2+x_3^2)^{1/2}}\right] \end{aligned} \tag{5.10}$$

where $r=\sqrt{x_1^2+x_2^2}$ and a_2 and b_2 are two scale radii.

Dark Halo

The potential of the halo is given by

$$
\begin{aligned}
\phi_3(R) &= -\frac{1}{R}\frac{GM_3\,(R/a_3)^{2.02}}{1+(R/a_3)^{1.02}} - \frac{GM_3}{1.02a_3}\times \\
&\quad \times\left[-\frac{1.02}{1+(R/a_3)^{1.02}} + \ln\left[1+(R/a_3)^{1.02}\right]\right]_R^{R_{MAX}=100} \\
&= -\frac{1}{R}\frac{GM_3\,(R/a_3)^{2.02}}{1+(R/a_3)^{1.02}} - \frac{GM_3}{1.02a_3}\times \\
&\quad \times\left[C+\frac{1.02}{1+(R/a_3)^{1.02}} - \ln\left[1+(R/a_3)^{1.02}\right]\right] \\
&= -\frac{1}{R}\frac{GM_3\,(R/a_3)^{2.02}}{1+(R/a_3)^{1.02}} - \frac{GM_3}{1.02a_3}C+ \\
&\quad -\frac{GM_3}{1.02a_3}\frac{1.02}{1+(R/a_3)^{1.02}} + \frac{GM_3}{1.02a_3}\ln\left[1+(R/a_3)^{1.02}\right] \\
&= \frac{GM_3}{1.02a_3}\ln\left[1+(R/a_3)^{1.02}\right] - \frac{GM_3}{1.02a_3}C+ \\
&\quad -GM_3\frac{1.02a_3\,(R/a_3)^{2.02}+1.02R}{1.02a_3R\left[1+(R/a_3)^{1.02}\right]} \\
&= \frac{GM_3}{1.02a_3}\ln\left[1+(R/a_3)^{1.02}\right] - \frac{GM_3}{1.02a_3}C - \frac{GM_3}{a_3} \\
&= \frac{GM_3}{1.02a_3}\left\{\ln\left[1+(R/a_3)^{1.02}\right] - C - 1.02\right\} \\
&= \frac{GM_3}{1.02a_3}\left\{\ln\left[1+(R/a_3)^{1.02}\right] - 3.1863227746391254\right\}
\end{aligned}
\tag{5.11}
\tag{5.12}
$$

where the last line shows the computationally more efficient version. C comes from

$$
-\frac{1.02}{1+\left(\frac{R}{a}\right)^{1.02}} + \ln\left[1+\left(\frac{R}{a}\right)^{1.02}\right] \tag{5.13}
$$

substituting $R = R_{\rm MAX} = 100$ Gpc and $a = 12$ kpc.

The mass, the acceleration and the jerk are:

$$M_3(R) = \frac{M_3 (R/a_3)^{2.02}}{1+(R/a_3)^{1.02}} \tag{5.14}$$

$$\rho_3(R) = \frac{M_3}{4\pi a_3 R^2} (R/a_3)^{1.02} \frac{2.02+(R/a_3)^{1.02}}{\left[1+(R/a_3)^{1.02}\right]^2} \tag{5.15}$$

$$a_{3i} = -x_i G M_3 \frac{a_3^{-2.02}}{a_3} R^{-0.98} \tag{5.16}$$

$$j_{3i} = x_i \left[-GM_3 \frac{a_3^{-2.02}}{a_3} R^{-0.98} \right] \times \\ \times \left[\frac{v_i}{x_i} - 0.98 \frac{\mathbf{x}\cdot\mathbf{v}}{R^2} - 1.02 (R/a_3)^{1.02} \frac{\frac{\mathbf{R}\cdot\mathbf{v}}{R^2}}{1+(R/a_3)^{1.02}} \right] \tag{5.17}$$

a_3 is a scale radius.

5.2 Tidal field implementation

In principle, STARLAB comes with a routine dedicated to external tidal fields different from the Plummer one (`add_tidal`). However, this routine assumes a non inertial reference frame to be able to maintain the galactic center on the negative x-axis. This implementation implies a number of technical problems which made us prefer an alternative solution. We directly substituted the Allen and Santillan (1991) routines to the Plummer tidal field in the `add_plummer` function (`dyn_external.C` file). This substitution allowed us to avoid any other modification to the code, ensuring that the final result is not affected by unwanted bugs. Moreover, the Plummer tidal field was built on an inertial reference frame, thus providing and easier implementation and less computations during simulations. The host galaxy dynamical friction (i.e. the dynamical friction acting on the YSC) has been deactivated because it was only correct for a Plummer tidal field. All the relevant parameters for a Milky Way-like tidal field are now hard-coded into the STARLAB routines. This means that to simulate a YSC in the Allen and Santillan (1991) tidal field one only needs to call the `add_plummer` tool of the new code while creating the initial conditions,

without any parameter. `add_plummer` takes care of creating the correct initial conditions to instruct STARLAB about the new tidal field. For more information about how the tidal field is implemented and how to run simulations with the tidal field enable, see appendix A.1.2.

CHAPTER 6

CONCLUSIONS AND FUTURE PERSPECTIVES

6.1 Conclusions

I studied the population of DCOBs in YSCs to derive accurate predictions for Advanced Virgo and LIGO upcoming observations. To this purpose I ran and analyzed $\gtrsim 10^3$ direct N-body simulations with up-to-date metallicity dependent stellar evolution of YSCs. These recipes take into account the possibility of formation of BHs by "direct collapse", allowing the formation of more massive remnants. I also developed a suite of programs to make easier to check and manage simulations.

I followed DCOBs throughout their life investigating the impact of dynamics, metallicity and structural properties of the host YSCs on the population of BMCs.

I investigate how many DCOBs are produced for each model of YSCs and DCOB type ($\langle n_{\rm BH-BH}\rangle_{\rm SC} \sim 4$ for all BH-BH and $\langle n_{\rm BH-BH,hard}\rangle_{\rm SC} \sim 1$ for hard BH-BH,

$\langle n_{\rm BH-BH,BH-NS}\rangle_{\rm SC} \sim 0.1$ for NS-NS and BH-NS binaries) I also considered how this quantity changes with time. The number of hard BH-BH binaries grows monotonically in time from 0 to $\langle n_{\rm BH-BH,hard}\rangle_{SC}(t = 100\,{\rm Myr}) \sim 0.2 - 0.4$ while soft BH-BH binaries show a peak (after the core collapse, which occurs at different times for different densities) and then decrease to ~ 0.05.

In my simulations $\gtrsim 90\%$ of BH-BH binaries are the product of dynamical exchanges and this result indicates that BHs are extremely efficient in finding companions through dynamical exchanges.

Moreover, because low metallicity allows the formation of BHs with higher masses, at low metallicity BH-BH binaries form earlier and are more stable.

I also found that, because of dynamics, NS-NS binaries are ten times less numerous than BH-BH ones, despite the initial mass function.

BH-BH formation is favored also by high density ($\sim 3\times10^3\,{\rm M_\odot pc^{-3}}$) and high concentration (dimensionless central potential $W_0 \gtrsim 3$). However, it is not very sensitive to primordial binary fraction.

It is worth noting that only 23% of BH-BH BMCs come from exchanges. Nevertheless, dynamical encounters are important in primordial binaries, because they speed up the shrinking of BH-BH binary semi-major axis (SMA) a to the point at which the binary evolution is dominated by GW emission. Without dynamics, this process would have taken much more time (up to $\sim 10^{24}\,{\rm Gyr}$).

I found that 6% of NS-NS BMCs come from exchanges. I expected the vast majority (if not all) of NS-NS binaries to be primordial, because it is unlikely for a NS to acquire a NS companion in an environment where BHs dominate dynamical interactions.

Thus, it is interesting that we found even also some NS-NS binaries (6%) formed through exchanges.

Looking at BH masses, in my simulations, I found BHs are heavier at low metallicity (maximum BH mass $\sim 80\,{\rm M_\odot}$ at $Z = 0.01\,{\rm Z_\odot}$). This is a consequence of the stellar evolution and failed SN recipes adopted. Moreover, even more massive BHs can form when a BH merges with stellar companion. The maximum BH

mass I find in BH-BH binaries is $\sim 125\,M_\odot$.

The chirp masses reflect this trend. Chirp masses of the simulated BH-BH binaries are up to $\sim 80\,M_\odot$. The maximum chirp mass for a BMC binary is quite lower ($\sim 40\,M_\odot$) and the rest of BMCs chirp masses are below $20\,M_\odot$.

By comparing SMAs between BH-BH binaries and NS-NS ones show that, while NS-NS binaries are much less numerous than BH-BH, their SMA are much shorter (minimum SMA for NS-NS $a_{\mathrm{min,NS-NS}} \sim 10^{-3}$ AU compared to $a_{\mathrm{min,BH-BH}} \sim 10^{-1}$ AU). This is a consequence of selection: NS-NS binaries come from binaries close enough to survive two SN explosions and dynamical encounters.

This fact can be observed also in the coalescence timescale : NS-NS binaries have shorter coalescence timescales ($t_{\mathrm{GW,min,NS-NS}} \sim 10^{-5}$ Gyr compared to $t_{\mathrm{GW,min,BH-BH}} \sim 10^{-1}$ Gyr for BH-BH). In fact, 76% of NS-NS BMC binaries merge during the simulations (36% of all the NS-NS binaries), while none of BH-BH binaries does.

BH-BH binaries have never been directly observed in our Galaxy, but we observe 10 NS-NS binaries (Lorimer, 2008). This was a good opportunity to compare my simulations to observations.

The agreement between the observed and simulated NS-NS binaries properties (period, eccentricity and coalescence timescale)is very good. The only differences can be found at the shortest and longest periods. The differences are due to selection effects: at very short periods ($\lesssim 2$ hours) NS-NS binaries merge very fast and it is hard to observe them in this state, while the longest periods ($\gtrsim 10^3$ days) are too long to be observed since now.

The final step is to predict the expected merger and detection rates for DCOBs binaries. I also investigated whether they depend on YSC properties (mass, density, concentration primordial binary fractions, metallicity). I found no significant dependence of BH-BH merger rates on the structural properties of YSCs, within the considered ranges. However, uncertainties are still quite large.

The global merger rate for BH-BH binaries derived from my simulations is $R_{\mathrm{merger,BH-BH}} = 0.0019 \pm 0.0007\,\mathrm{Mpc^{-3}Myr^{-1}}$. The final BH-BH detection rates

shows a dependence, with large uncertainties, on the density and concentration of the host YSC: they are higher for more dense and concentrated clusters. This trend is the same as that of the average number of BH-BH binaries produced during the cluster life. Moreover, the BH-BH detection rate anti-correlates with the primordial binary fraction. This result needs further investigations. The global detection rate for BH-BH binaries is $R_{\mathrm{detection,BH-BH}} = 0.8 \pm 0.2\,\mathrm{yr}^{-1}$. The global merger and detection rates of NS-NS and BH-NS binaries are are $R_{\mathrm{merger,NS-NS}} = 0.258 \pm 0.005\,\mathrm{Mpc}^{-3}\mathrm{Myr}^{-1}$, $R_{\mathrm{merger,BH-NS}} = 0.0009 \pm 0.0002\,\mathrm{Mpc}^{-3}\mathrm{Myr}^{-1}$, $R_{\mathrm{detection,NS-NS}} = 0.65 \pm 0.01\,\mathrm{yr}^{-1}$, $R_{\mathrm{detection,BH-NS}} = 0.0107 \pm 0.0006\,\mathrm{yr}^{-1}$ for NS-NS and BH-NS, respectively.

The merger and detection rates of BH-BH and NS-NS binaries are consistent with the pessimistic rates provided by Virgo and LIGO collaboration (Abadie et al., 2010). The BH-NS merger and detection rate are even lower than the most pessimistic prediction in literature because BH-NS mergers are disfavored by dynamical processes that favor BH-BH production at the expense of BH-NS ones.

My thesis is a first important step towards understanding the formation and evolution of DCOBs in dynamically active young star clusters. It is essential to continue this line of research, in order to meet the challenge of forthcoming multi-messenger astrophysics.

6.2 Future perspectives

I would like to further investigate the subject according to the following research lines.

Statistical sample The natural continuation of this work is to improve the statistical sample with more realization.

Tidal field I would like to apply the newly implemented tidal field routines to investigate the role of the host galaxy tidal field on the DCOBs population.

SCs and DCO binaries during galaxy mergers As a continuation of my work on tidal fields I would like to investigate the evolution of star clusters and DCOBs during galaxy mergers.

SC formation from a gas cloud I would like to simulate the formation of young dense SCs from a gas cloud. This would provide insights on the distribution of SC properties as a function of the progenitor environment. STARLAB does not provide regularization algorithms.

Mikkola regularization STARLAB does not provide regularization algorithms. I would like to implement the "Mikkola regularization" (Mikkola and Aarseth, 1993; Mikkola and Merritt, 2006; Mikkola and Merritt, 2008) algorithm in STARLAB. This would make me able to perform an accurate integration of more massive clusters, and clusters with more binaries.

Multiple systems I noticed, in my simulations, the formation of about 2×10^4 systems with more than two components (multiple systems) and containing at least one object that will become a stellar remnant. I want to investigate the role of triple and multiple systems in the dynamics of DCOBs as well as the possibility of GW emission from a system composed of three compact objects.

APPENDIX

A.1 Run a simulation with STARLAB

To run a simulation with STARLAB two main steps are needed: (i) create appropriate initial conditions (ICs) and (ii) run STARLAB with the right flags on that ICs.

The first step can be requires to call in the right sequence the right tools STARLAB provide. The best way to do this is to write a script to do that. An example is something like:

```
#!/bin/bash

makeking -n 10000 -w 5 -i -u \
| makemass -f 8  -l 0.1 -u 150 \
| makesecondary -f 0.1 -q -l 0.1 \
| add_star -R 1 -Z 0.10 \
| scale -R 3 -M 1\
| makebinary -f 2 -o 1 -l 1 -u 107836.09 \
```

```
9 > ics-comb87-TFno-Rv3-NCM10000-fPB01-W5-Z010-run01-
    rnd00.txt
```

Assuming all the STARLAB tools are in a folder visible to the `$PATH` environment variable, here we are calling one after the other the commands to generate the ICs for a YSC like those I simulated.

`makeking -n 10000 -w 5 -i -u` generates the positions for a cluster of 10^4 equal mass particles following a King profile with $W_0 = 5$; the particles are numbered sequentially (`-i`) and the cluster is not scaled (`-u`)

`makemass -f 8 -l 0.1 -u 150` generate the masses of the primary and single stars from a given IMF (`-f`, where 1 corresponds to a power-law, 2 to a Miller&Scalo, 3 to a Scalo, 4 to a old Kroupa, 5 to a De Marchi, 6 to a old Kroupa+ 1991, 7 to a two power law, 8 to a Kroupa 2001 IMF); `-l` and `-u` specify the lower and upper mass limits in $M_\odot$

`makesecondary -f 0.1 -q -l 0.1` generates the masses of the secondary stars for the number of binaries specified by the fraction respect to the total number of center of masses by `-f`; the masses are drawn from a flat distribution with limits given by `-l` (and `-u` or 1 if not specified) in units of the primary masses limits (`-q` flag)

`add_star -R 1 -Z 0.10 , scale -R 3 -M 1` generates the physical properties of stars (radius, mass - which defaults to the total mass, metallicity in units of $Z_\odot = 0.019$) and scale them

`makebinary -f 2 -o 1 -l 1 -u 107836.09` generates the orbital properties of primordial binaries: `-f` specifies how to select them (2 is the SMA, while 1 and 3 select the angular momentum per units reduced mass or the energy, respectively), `-o 1 -l 1 -u 107836.09` specify the limits for the SMAs in units of $R_\odot$, where $107836.09\,R_\odot \sim 500\,AU$

Both `add_star` and `scale` allow to scale the system. For example

1. `./add_star -R 1 | ./scale -R 5` means $r_v = 5$ in units of 1 pc, thus $r_v = 5$
2. `./add_star -R 5 | ./scale -R 1` means $r_v = 1$ in units of 5 pc, thus $r_v = 5$

These two choice give the same result: the first is easier, the second gives more physical meaning to timescale. I chose the first one because it provides more explicit information in the output files.
Once the ICs are generated, STARLAB is ran by calling the `kira` tool with the appropriate flags:

```
kira -t 500 -d 1 -D 1 -f 0 -n 10 -e 0 -B -b 1 \
< ics-comb87-TFno-Rv3-NCM10000-fPB01-W5-Z010-run01-
   rnd00.txt \
> out-comb87-TFno-Rv3-NCM10000-fPB01-W5-Z010-run01-
   rnd00.txt \
2> err-comb87-TFno-Rv3-NCM10000-fPB01-W5-Z010-run01
   -rnd00.txt
```

where

`-t` set the total number of timestep we want to simulate

`-d` set the log output interval

`-D` set the snapshot (output) interval

`-f` set the dynamical friction

`-n` minimum number of particles allowed, if

`-e` set the softening

`-B` switch on binary evolution

`-b` set the frequency of full binary output

Input and output are managed through `STDIN`, `STOUT` and `STDERR`.

A.1.1 SLTOOLS

To run simulations with STARLAB with the help of SLTOOS, first you need to create one or more simulation configuration files, for example

```
{
        "Runs": 50,
        "Comb": 86,
        "Ncm" : 10000,
        "Fpb" : 0.05,
        "W"   : 3,
        "Z"   : 0.10,
        "Rv": 5,
        "EndTime" : 500,
        "Machine" : "yourCluster",
        "UserName" : "yourUserName",
        "PName": "project",
        "BinFolder": "/home/yourUserName/bin/"
}
```

where

- `Runs` is the number of random realizations you want to simulate
- `Comb` is the number that identify of this particular parameter set
- `Ncm` is the number of center of masses
- `Fpb` is the primordial binary fraction (how many stars are binaries at the beginning of the simulation
- `W` is the central adimensional potential
- `Z` is the metallicity in terms of the solar metallicity (only available in the Mapelli+2013 Starlab version)
- `Rv` is the initial virial radius of the cluster

- `EndTime` preliminary timestep when to stop the simulation, you can resume it later
- `Machine` name of the machine you are running on
- `UserName` is your `username` on that machine
- `PName` is the project your hours are accounted on
- `BinFolder` is the path where to find the binaries

Then run

```
sltools createICs -v -A
```

SLTOOLS will create for you a folder for each parameter combination, copy the configuration file inside and create as much script files as you need to create the ICs.
Run the generated script with

```
for RUN in $(ls create_*.sh); do bash $RUN; done
```

or you can run them using the `docker` container you can build starting from the image you can find at https://registry.hub.docker.com/u/brunetto/starlab-public-docker/ or from the Dockerfile at https://github.com/brunetto/starlab-public-docker/blob/master/Dockerfile or following the instructions at http://brunettoziosi.eu/posts/dockerized-starlab/.
If you plan to use the GPUs the second method is recommended since a GPU enable docker image is system-dependent.
If you are running your simulations on a cluster, once the ICs are created, they can be uploaded on to the cluster of your choice. Once everything is in its place, connect to the cluster and run

```
sltools css -A -m <machine>
```

to create the files needed to submit the jobs to the batch system. `machine` is the name of the cluster. Until now only few clusters are recognized, because I need to set few parameters to match the system configuration.

Once the batch manager scripts are created, all the jobs can be submitted with

```
sltools pbsLaunch
```

When the simulations are finished, it is possible to restart them with

```
sltools relaunch
```

or

```
sltools relaunch -e <end-time>
```

to specify when the simulation should end.
If the simulations run on a workstation without a batch manager system, they can be started with

```
kiraWrap -i <ICs file name> -t <timestep to
   simulate>
```

to run `kira` inside a wrapper that monitor the correct execution.

A.1.2 Include Allen and Santillan (1991) tidal field

Run simulations with the tidal field enabled

In order to run a simulation with the Allen and Santillan (1991) tidal field enabled, only two steps are required. First, substitute the code listed in the next Section to the `add_plummer` function in the `dyn_external.C` source that can be found in the `src/node/dyn/util/` folder and deactivate the dynamical friction, then compile STARLAB. Second, specify in the ICs generation that the tidal field is enabled. STARLAB will then read from the ICs the tidal field settings and will integrate the cluster correctly.
To modify the initial conditions we only need to add (in the right place) two instructions:

`add_plummer` to notify STARLAB that we want to enable the tidal field

`set_com` tells starlab to move the center of mass in order to place the YSC at a certain position (specified by the three numbers, one for each Cartesian

coordinate, in unit of kpc, after the `-r` flag) with a certain velocity (specified by the three numbers, in unit of the circular velocity, after the `-v` flag)

The final script to create ICs with the tidal field enable looks like:

```
#!/bin/bash

makeking -n 10000 -w 5 -i -u \
| makemass -f 8  -l 0.1 -u 150 \
| makesecondary -f 0.1 -q -l 0.1 \
| add_star -R 1 -Z 0.10 \
| add_plummer \
| set_com -r -7974.0 -393.0 -112.0 -v
   -0.03876967039166435 0.9154203350125925 \
| scale -R 3 -M 1\
| makebinary -f 2 -o 1 -l 1 -u 107836.09 \
> ics-comb87-TFno-Rv3-NCM10000-fPB01-W5-Z010-run01-
   rnd00.txt
```

Allen and Santillan (1991) implementation in STARLAB

This is the code to be substituted in the `add_plummer` function in the `dyn_external.C` source that can be found in the `src/node/dyn/util/`:

```
double Rscale = 1000.0;
double Mscale = 1.0e10;

//galactic parameters
double plummer_b = 387.3 / Rscale;
double plummer_M = 1.40592e10 / Mscale;

double disk_a = 5317.8 / Rscale;
double disk_M = 8.56080e10 / Mscale;
```

```
10 double disk_b = 250.0 / Rscale;
11
12 double halo_a = 12000.0 / Rscale;
13 double halo_M = 10.70680e10 / Mscale;
14
15 //ADD GALACTIC PLUMMER CONTRIBUTIONS
16
17 vec cdm_pos = b->get_root()->get_pos();
18 vec cdm_vel = b->get_root()->get_vel();
19 vec gal_cen = b->get_p_center();
20
21 double drx = pos[0] + cdm_pos[0] - gal_cen[0];
22 double dry = pos[1] + cdm_pos[1] - gal_cen[1];
23 double drz = pos[2] + cdm_pos[2] - gal_cen[2];
24
25 double dvx = vel[0] + cdm_vel[0];
26 double dvy = vel[1] + cdm_vel[1];
27 double dvz = vel[2] + cdm_vel[2];
28
29 double distance = (drx*drx + dry*dry + drz*drz) +
     plummer_b*plummer_b;
30 double sqrdist  = plummer_M / sqrt(distance*
     distance*distance);
31 distance = 1.0/distance;
32
33 double alpha = (dvx*drx + dvy*dry + dvz*drz)*
     distance;
34 double scalar3 = -3.0 * alpha * sqrdist;
35
36 double aux = sqrdist*dvx + scalar3 * drx;
37 double auy = sqrdist*dvy + scalar3 * dry;
```

```
38 double auz = sqrdist*dvz + scalar3 * drz;
39
40 acc[0] -= drx*sqrdist;
41 acc[1] -= dry*sqrdist;
42 acc[2] -= drz*sqrdist;
43
44 jerk[0] -= aux;
45 jerk[1] -= auy;
46 jerk[2] -= auz;
47
48 //ADD GALACTIC DISK CONTRIBUTIONS
49
50 double alp = disk_b*disk_b + drz*drz;
51 alp = sqrt(alp);
52
53 distance = drx*drx + dry*dry + drz*drz;
54 distance = sqrt(distance);
55
56 double A3 = distance*distance - drz*drz + (disk_a +
       alp)*(disk_a + alp);
57 double M2 = - disk_M/pow(A3, 1.5);
58
59 acc[0] += M2*drx;
60 acc[1] += M2*dry;
61 acc[2] += M2*drz*(alp+disk_a)/alp;
62
63 double A1 = dvx*drx + dvy*dry + dvz*drz;
64 double cost = A1 + disk_a/alp * drz*dvz;
65 cost = cost/A3;
66
67 double spunto = drz*dvz/alp;
```

```
68
69 double tmp1 = M2*drx*(dvx/drx - 3.0 * cost);
70 double tmp2 = M2*dry*(dvy/dry - 3.0 * cost);
71 double tmp3 = M2*drz*(dvz/drz - 3.0 * cost);
72
73 jerk[0] += tmp1;
74 jerk[1] += tmp2;
75 jerk[2] += tmp3*(alp+disk_a)/alp - M2*drz*disk_a/(
      alp*alp)*spunto;
76
77 //ADD GALACTIC HALO CONTRIBUTIONS
78
79 double A2 = 1.0 + pow(distance/halo_a, 1.02);
80 cost = - halo_M * pow(halo_a,-2.02)/A2*pow(distance
      ,-0.98);
81
82 acc[0] += cost*drx;
83 acc[1] += cost*dry;
84 acc[2] += cost*drz;
85
86 A3 = A1/(distance*distance);
87 alp = 1.02*(A2-1.0)*A3/A2;
88 alp = - 0.98*A3 - alp;
89
90 tmp1 = cost*drx*(dvx/drx + alp);
91 tmp2 = cost*dry*(dvy/dry + alp);
92 tmp3 = cost*drz*(dvz/drz + alp);
93
94 jerk[0] += tmp1;
95 jerk[1] += tmp2;
96 jerk[2] += tmp3;
```

```
97
98  //ADD VARIOUS CONTRIBUTIONS TO THE POTENTIAL
99
100 distance = drx * drx + dry * dry + drz * drz;
101 double x = sqrt(distance)/halo_a;
102 double r2d_2 = drx * drx + dry * dry;
103 double diskdist = disk_a + sqrt(drz*drz + disk_b*
       disk_b);
104
105 //plummer potential contribution
106 pot -= plummer_M / sqrt(distance + plummer_b*
       plummer_b);
107
108 //halo potential contribution
109 pot += halo_M/(1.02*halo_a)*(log(1.0+pow(x,1.02))
       -3.1863227746391254);
110
111 //disk potential contribution
112 pot -= disk_M / sqrt(r2d_2 + diskdist*diskdist);
```

BIBLIOGRAPHY

Aarseth, S. J. (1963). "Dynamical evolution of clusters of galaxies, I". In: MNRAS 126, p. 223.

— (2003). *Gravitational N-Body Simulations*.

Aasi, J. et al. (2012). "The characterization of Virgo data and its impact on gravitational-wave searches". In: *Classical and Quantum Gravity* 29.15, 155002, p. 155002. DOI: 10.1088/0264-9381/29/15/155002. arXiv: 1203.5613 [gr-qc].

— (2013). "Search for gravitational waves from binary black hole inspiral, merger, and ringdown in LIGO-Virgo data from 2009-2010". In: Phys. Rev. D 87.2, 022002, p. 022002. DOI: 10.1103/PhysRevD.87.022002. arXiv: 1209.6533 [gr-qc].

Abadie, J. et al. (2010). "TOPICAL REVIEW: Predictions for the rates of compact binary coalescences observable by ground-based gravitational-wave detectors". In: *Classical and Quantum Gravity* 27.17, 173001, p. 173001. DOI: 10.1088/0264-9381/27/17/173001. arXiv: 1003.2480 [astro-ph.HE].

Abadie, J. et al. (2012a). "Search for gravitational waves from intermediate mass binary black holes". In: Phys. Rev. D 85.10, 102004, p. 102004. DOI: 10.1103/PhysRevD.85.102004. arXiv: 1201.5999 [gr-qc].

— (2012b). "Search for gravitational waves from low mass compact binary coalescence in LIGO's sixth science run and Virgo's science runs 2 and 3". In: Phys. Rev. D 85.8, 082002, p. 082002. DOI: 10.1103/PhysRevD.85.082002. arXiv: 1111.7314 [gr-qc].

Abramovici, A. et al. (1992). "LIGO - The Laser Interferometer Gravitational-Wave Observatory". In: *Science* 256, pp. 325–333. DOI: 10.1126/science.256.5055.325.

Accadia, T. and The Virgo Collaboration (2012). *Advanced Virgo Technical Design Report*. Tech. rep. VIR-0128A-12. URL: https://tds.ego-gw.it/ql/?c=8940.

Acernese, F. and The Virgo Collaboration (2009). *Advanced Virgo Technical Design Report*. Tech. rep. VIR-0027A-09. URL: https://tds.ego-gw.it/ql/?c=6589.

Aguilar, L., P. Hut, and J. P. Ostriker (1988). "On the evolution of globular cluster systems. I - Present characteristics and rate of destruction in our Galaxy". In: ApJ 335, pp. 720–747. DOI: 10.1086/166961.

Allen, C. and A. Santillan (1991). "An improved model of the galactic mass distribution for orbit computations". In: Rev. Mexicana Astron. Astrofis. 22, pp. 255–263.

Baumgardt, H. (2001). "Scaling of N-body calculations". In: MNRAS 325, pp. 1323–1331. DOI: 10.1046/j.1365-8711.2001.04272.x. eprint: astro-ph/0012330.

Baumgardt, H. and J. Makino (2003). "Dynamical evolution of star clusters in tidal fields". In: MNRAS 340, pp. 227–246. DOI: 10.1046/j.1365-8711.2003.06286.x. eprint: astro-ph/0211471.

Belczynski, K., V. Kalogera, and T. Bulik (2002). "A Comprehensive Study of Binary Compact Objects as Gravitational Wave Sources: Evolutionary Channels, Rates, and Physical Properties". In: ApJ 572, pp. 407–431. DOI: 10.1086/340304. eprint: astro-ph/0111452.

Belczynski, K. et al. (2006). "Initial Populations of Black Holes in Star Clusters". In: ApJ 650, pp. 303–325. DOI: 10.1086/506186. eprint: astro-ph/0508005.

Belczynski, K. et al. (2007). "On the Rarity of Double Black Hole Binaries: Consequences for Gravitational Wave Detection". In: ApJ 662, pp. 504–511. DOI: 10.1086/513562. eprint: astro-ph/0612032.

Belczynski, K. et al. (2010a). "On the Maximum Mass of Stellar Black Holes". In: ApJ 714, pp. 1217–1226. DOI: 10.1088/0004-637X/714/2/1217. arXiv: 0904.2784 [astro-ph.SR].

Belczynski, K. et al. (2010b). "The Effect of Metallicity on the Detection Prospects for Gravitational Waves". In: ApJ 715, pp. L138–L141. DOI: 10.1088/2041-8205/715/2/L138. arXiv: 1004.0386 [astro-ph.HE].

Belczynski, Krzysztof et al. (2013). "Cyg X-3: A Galactic Double Black Hole or Black-hole-Neutron-star Progenitor". In: *The Astrophysical Journal* 764.1, p. 96. URL: http://stacks.iop.org/0004-637X/764/i=1/a=96.

Binney, J. and S. Tremaine (2008). *Galactic Dynamics: Second Edition*. Princeton University Press.

Brown, D. A. and P. J. Zimmerman (2010). "Effect of eccentricity on searches for gravitational waves from coalescing compact binaries in ground-based detectors". In: Phys. Rev. D 81.2, 024007, p. 024007. DOI: 10.1103/PhysRevD.81.024007. arXiv: 0909.0066 [gr-qc].

Burgay, M. et al. (2003). "An increased estimate of the merger rate of double neutron stars from observations of a highly relativistic system". In: Nature 426, pp. 531–533. DOI: 10.1038/nature02124. eprint: astro-ph/0312071.

Carpenter, J. M. (2000). "2MASS Observations of the Perseus, Orion A, Orion B, and Monoceros R2 Molecular Clouds". In: AJ 120, pp. 3139–3161. DOI: 10.1086/316845. eprint: astro-ph/0009118.

Clark, J. et al. (2014). "Prospects for joint gravitational wave and short gamma-ray burst observations". In: *ArXiv e-prints*. arXiv: 1409.8149 [astro-ph.HE].

Clausen, D., S. Sigurdsson, and D. F. Chernoff (2013). "Black hole-neutron star mergers in globular clusters". In: MNRAS 428, pp. 3618–3629. DOI: 10.1093/mnras/sts295. arXiv: 1210.8153 [astro-ph.HE].

Coward, D. M. et al. (2012). "The Swift short gamma-ray burst rate density: implications for binary neutron star merger rates". In: MNRAS 425, pp. 2668–2673. DOI: 10.1111/j.1365-2966.2012.21604.x. arXiv: 1202.2179 [astro-ph.CO].

Davis, P. J., U. Kolb, and C. Knigge (2012). "Is the common envelope ejection efficiency a function of the binary parameters?" In: MNRAS 419, pp. 287–303. DOI: 10.1111/j.1365-2966.2011.19690.x. arXiv: 1106.4741 [astro-ph.SR].

Dehnen, W. and J. I. Read (2011). "N-body simulations of gravitational dynamics". In: *European Physical Journal Plus* 126, 55, p. 55. DOI: 10.1140/epjp/i2011-11055-3. arXiv: 1105.1082 [astro-ph.IM].

Dewi, J. D. M., P. Podsiadlowski, and A. Sena (2006). "Double-core evolution and the formation of neutron star binaries with compact companions". In: MNRAS 368, pp. 1742–1748. DOI: 10.1111/j.1365-2966.2006.10233.x. eprint: astro-ph/0602510.

Dominik, M. et al. (2012). "Double Compact Objects. I. The Significance of the Common Envelope on Merger Rates". In: ApJ 759, 52, p. 52. DOI: 10.1088/0004-637X/759/1/52. arXiv: 1202.4901 [astro-ph.HE].

— (2013). "Double Compact Objects. II. Cosmological Merger Rates". In: ApJ 779, 72, p. 72. DOI: 10.1088/0004-637X/779/1/72. arXiv: 1308.1546 [astro-ph.HE].

Downing, J. M. B. et al. (2010). "Compact binaries in star clusters - I. Black hole binaries inside globular clusters". In: MNRAS 407, pp. 1946–1962. DOI: 10.1111/j.1365-2966.2010.17040.x. arXiv: 0910.0546 [astro-ph.SR].

— (2011). "Compact binaries in star clusters - II. Escapers and detection rates". In: MNRAS 416, pp. 133–147. DOI: 10.1111/j.1365-2966.2011.19023.x. arXiv: 1008.5060 [astro-ph.GA].

Duquennoy, A. and M. Mayor (1991). "Multiplicity among solar-type stars in the solar neighbourhood. II - Distribution of the orbital elements in an unbiased sample". In: A&A 248, pp. 485–524.

Elson, R., P. Hut, and S. Inagaki (1987). "Dynamical evolution of globular clusters". In: ARA&A 25, pp. 565–601. DOI: 10.1146/annurev.aa.25.090187.003025.

Esposito, P. et al. (2015). "Periodic signals from the Circinus region: two new cataclysmic variables and the ultraluminous X-ray source candidate GC X-1". In: *ArXiv e-prints*. arXiv: 1506.05808 [astro-ph.HE].

Finn, L. S. (1996). "Binary inspiral, gravitational radiation, and cosmology". In: Phys. Rev. D 53, pp. 2878–2894. DOI: 10.1103/PhysRevD.53.2878. eprint: gr-qc/9601048.

Fryer, C. L. (1999). "Mass Limits For Black Hole Formation". In: ApJ 522, pp. 413–418. DOI: 10.1086/307647. eprint: astro-ph/9902315.

Fryer, C. L. and V. Kalogera (2001). "Theoretical Black Hole Mass Distributions". In: ApJ 554, pp. 548–560. DOI: 10.1086/321359. eprint: astro-ph/9911312.

Fryer, C. L. et al. (2012). "Compact Remnant Mass Function: Dependence on the Explosion Mechanism and Metallicity". In: ApJ 749, 91, p. 91. DOI: 10.1088/0004-637X/749/1/91. arXiv: 1110.1726 [astro-ph.SR].

Fukushige, T. and D. C. Heggie (2000). "The time-scale of escape from star clusters". In: MNRAS 318, pp. 753–761. DOI: 10.1046/j.1365-8711.2000.03811.x. eprint: astro-ph/9910468.

Gieles, M. and S. F. Portegies Zwart (2011). "The distinction between star clusters and associations". In: MNRAS 410, pp. L6–L7. DOI: 10.1111/j.1745-3933.2010.00967.x. arXiv: 1010.1720 [astro-ph.GA].

Giersz, M. and D. C. Heggie (1994). "Statistics of N-Body Simulations - Part Two - Equal Masses after Core Collapse". In: MNRAS 270, p. 298. eprint: astro-ph/9403024.

Gnedin, O. Y., H. M. Lee, and J. P. Ostriker (1999). "Effects of Tidal Shocks on the Evolution of Globular Clusters". In: ApJ 522, pp. 935–949. DOI: 10.1086/307659. eprint: astro-ph/9806245.

Goddard, Q. E., N. Bastian, and R. C. Kennicutt (2010). "On the fraction of star clusters surviving the embedded phase". In: MNRAS 405, pp. 857–869. DOI: 10.1111/j.1365-2966.2010.16511.x. arXiv: 1002.2894 [astro-ph.CO].

Goodman, J. and P. Hut (1993). "Binary-single-star scattering. V - Steady state binary distribution in a homogeneous static background of single stars". In: ApJ 403, pp. 271–277. DOI: 10.1086/172200.

Harris, W. E. (1996). "A Catalog of Parameters for Globular Clusters in the Milky Way". In: AJ 112, p. 1487. DOI: 10.1086/118116.

Harry, G. M. and the LIGO Scientific Collaboration (2010). "Advanced LIGO: the next generation of gravitational wave detectors". In: *Classical and Quantum Gravity* 27.8, p. 084006. URL: http://stacks.iop.org/0264-9381/27/i=8/a=084006.

Hartman, J. W. (1997). "On the velocity distribution of radio pulsars at birth." In: A&A 322, pp. 127–130.

Heggie, D. and P. Hut (2003). *The Gravitational Million-Body Problem: A Multidisciplinary Approach to Star Cluster Dynamics*.

Heggie, D. C. (1975). "Binary evolution in stellar dynamics". In: MNRAS 173, pp. 729–787.

Hénon, M. (1960). "L'évasion des étoiles hors des amas isolés". In: *Annales d'Astrophysique* 23, p. 668.

— (1961). "Sur l'évolution dynamique des amas globulaires". In: *Annales d'Astrophysique* 24, p. 369.

Hills, J. G. (1989). "Effect of intruder mass on collisions with hard binaries. I - Zero-impact parameter". In: AJ 97, pp. 222–235. DOI: 10.1086/114973.

— (1992). “Effect of intruder mass on collisions with hard binaries. II - Dependence on impact parameter and computations of the interaction cross sections”. In: AJ 103, pp. 1955–1969. DOI: 10.1086/116204.

Hobbs, G. (2011). “Pulsars as gravitational wave detectors”. In: *High-Energy Emission from Pulsars and their Systems*. Ed. by D. F. Torres and N. Rea, p. 229. DOI: 10.1007/978-3-642-17251-9_20. arXiv: 1006.3969 [astro-ph.SR].

Holmberg, E. (1941). “On the Clustering Tendencies among the Nebulae. II. a Study of Encounters Between Laboratory Models of Stellar Systems by a New Integration Procedure.” In: ApJ 94, p. 385. DOI: 10.1086/144344.

Hopkins, A. M. and J. F. Beacom (2006). “On the Normalization of the Cosmic Star Formation History”. In: ApJ 651, pp. 142–154. DOI: 10.1086/506610. eprint: astro-ph/0601463.

Hulse, R. A. and J. H. Taylor (1975). “Discovery of a pulsar in a binary system”. In: ApJ 195, pp. L51–L53. DOI: 10.1086/181708.

Hurley, J. R., O. R. Pols, and C. A. Tout (2000). “Comprehensive analytic formulae for stellar evolution as a function of mass and metallicity”. In: MNRAS 315, pp. 543–569. DOI: 10.1046/j.1365-8711.2000.03426.x. eprint: astro-ph/0001295.

Kalogera, V. et al. (2004). “Erratum: “The Cosmic Coalescence Rates for Double Neutron Star Binaries”(ApJ, 601, L179 [2004])”. In: ApJ 614, pp. L137–L138. DOI: 10.1086/425868. eprint: astro-ph/0312101.

Kalogera, V. et al. (2007). “Formation of double compact objects”. In: Phys. Rep. 442, pp. 75–108. DOI: 10.1016/j.physrep.2007.02.008. eprint: astro-ph/0612144.

Katz, Joseph (2003). “Thermodynamics of Self-Gravitating Systems”. English. In: *Foundations of Physics* 33.2, pp. 223–269. ISSN: 0015-9018. DOI: 10.1023/A:1023776921610. URL: http://dx.doi.org/10.1023/A%3A1023776921610.

King, I. R. (1966). “The structure of star clusters. IV. Photoelectric surface photometry in nine globular clusters”. In: AJ 71, p. 276. DOI: 10.1086/109918.

Kraicheva, Z. T. et al. (1978). “Some characteristics of spectroscopic binary stars”. In: AZh 55, pp. 1176–1189.

Kroupa, P. (2001). “On the variation of the initial mass function”. In: MNRAS 322, pp. 231–246. DOI: 10.1046/j.1365-8711.2001.04022.x. eprint: astro-ph/0009005.

Kruijssen, J. M. D. et al. (2011). “Modelling the formation and evolution of star cluster populations in galaxy simulations”. In: MNRAS 414, pp. 1339–1364. DOI: 10.1111/j.1365-2966.2011.18467.x. arXiv: 1102.1013.

Lada, C. J. and E. A. Lada (2003). “Embedded Clusters in Molecular Clouds”. In: ARA&A 41, pp. 57–115. DOI: 10.1146/annurev.astro.41.011802.094844. eprint: astro-ph/0301540.

Lamers, H. J. G. L. M., M. Gieles, and S. F. Portegies Zwart (2005). "Disruption time scales of star clusters in different galaxies". In: A&A 429, pp. 173–179. DOI: 10.1051/0004-6361:20041476. eprint: astro-ph/0408235.

Lorimer, D. R. (2008). "Binary and Millisecond Pulsars". In: *Living Reviews in Relativity* 11, p. 8. arXiv: 0811.0762.

Lynden-Bell, D. (1999). "Negative Specific Heat in Astronomy, Physics and Chemistry". In: *Physica A Statistical Mechanics and its Applications* 263, pp. 293–304. DOI: 10.1016/S0378-4371(98)00518-4. eprint: cond-mat/9812172.

Lynden-Bell, D. and R. Wood (1968). "The gravo-thermal catastrophe in isothermal spheres and the onset of red-giant structure for stellar systems". In: MNRAS 138, p. 495.

Madrid, J. P., J. R. Hurley, and M. Martig (2014). "The Impact of Galaxy Geometry and Mass Evolution on the Survival of Star Clusters". In: ApJ 784, 95, p. 95. DOI: 10.1088/0004-637X/784/2/95. arXiv: 1402.2289 [astro-ph.GA].

Maggiore, M. (2008). Oxford University Press.

Makino, J. et al. (2003). "GRAPE-6: Massively-Parallel Special-Purpose Computer for Astrophysical Particle Simulations". In: PASJ 55, pp. 1163–1187. DOI: 10.1093/pasj/55.6.1163. eprint: astro-ph/0310702.

Mapelli, M. and A. Bressan (2013). "Impact of metallicity on the evolution of young star clusters". In: MNRAS 430, pp. 3120–3127. DOI: 10.1093/mnras/stt119. arXiv: 1301.4227 [astro-ph.GA].

Mapelli, M., M. Colpi, and L. Zampieri (2009). "Low metallicity and ultra-luminous X-ray sources in the Cartwheel galaxy". In: MNRAS 395, pp. L71–L75. DOI: 10.1111/j.1745-3933.2009.00645.x. arXiv: 0902.3540 [astro-ph.HE].

Mapelli, M. et al. (2010b). "Ultra-luminous X-ray sources and remnants of massive metal-poor stars". In: MNRAS 408, pp. 234–253. DOI: 10.1111/j.1365-2966.2010.17048.x. arXiv: 1005.3548 [astro-ph.CO].

Mapelli, M. et al. (2010a). "Gravitational Waves from Intermediate-mass Black Holes in Young Clusters". In: ApJ 719, pp. 987–995. DOI: 10.1088/0004-637X/719/2/987. arXiv: 1006.1664.

Mapelli, M. et al. (2012). "A cosmological view of extreme mass-ratio inspirals in nuclear star clusters". In: A&A 542, A102, A102. DOI: 10.1051/0004-6361/201118444. arXiv: 1205.2702 [astro-ph.CO].

McMillan, S. L. W., P. N. McDermott, and R. E. Taam (1987). "The formation and evolution of tidal binary systems". In: ApJ 318, pp. 261–277. DOI: 10.1086/165365.

Mikkola, S. (1997). "Non-canonical perturbations in symplectic integration". In: *Celestial Mechanics and Dynamical Astronomy* 68, pp. 249–255. DOI: 10.1023/A:1008278821576.

Mikkola, S. and S. J. Aarseth (1993). "An implementation of N-body chain regularization". In: *Celestial Mechanics and Dynamical Astronomy* 57, pp. 439–459. DOI: 10.1007/BF00695714.

Mikkola, S. and D. Merritt (2006). "Algorithmic regularization with velocity-dependent forces". In: MNRAS 372, pp. 219–223. DOI: 10.1111/j.1365-2966.2006.10854.x. eprint: astro-ph/0605054.

— (2008). "Implementing Few-Body Algorithmic Regularization with Post-Newtonian Terms". In: AJ 135, pp. 2398–2405. DOI: 10.1088/0004-6256/135/6/2398. arXiv: 0709.3367.

Miyamoto, M. and R. Nagai (1975). "Three-dimensional models for the distribution of mass in galaxies". In: PASJ 27, pp. 533–543.

Murali, C. and M. D. Weinberg (1997b). "Globular cluster evolution in M87 and fundamental plane ellipticals". In: MNRAS 288, pp. 767–776. eprint: astro-ph/9602058.

— (1997a). "Evolution of the Galactic globular cluster system". In: MNRAS 291, p. 717.

O'Leary, R. M. et al. (2006). "Binary Mergers and Growth of Black Holes in Dense Star Clusters". In: ApJ 637, pp. 937–951. DOI: 10.1086/498446. eprint: astro-ph/0508224.

O'Shaughnessy, R. et al. (2008). "Constraining Population Synthesis Models via Empirical Binary Compact Object Merger and Supernova Rates". In: ApJ 672, pp. 479–488. DOI: 10.1086/523620. eprint: astro-ph/0610076.

Özel, F. et al. (2010). "The Black Hole Mass Distribution in the Galaxy". In: ApJ 725, pp. 1918–1927. DOI: 10.1088/0004-637X/725/2/1918. arXiv: 1006.2834 [astro-ph.GA].

Padmanabhan, T. (1990). "Statistical mechanics of gravitating systems". In: Phys. Rep. 188, pp. 285–362. DOI: 10.1016/0370-1573(90)90051-3.

Panter, B. et al. (2008). "The cosmic evolution of metallicity from the SDSS fossil record". In: MNRAS 391, pp. 1117–1126. DOI: 10.1111/j.1365-2966.2008.13981.x. arXiv: 0804.3091.

Peters, P. C. (1964). "Gravitational Radiation and the Motion of Two Point Masses". In: *Phys. Rev.* 136 (4B), B1224–B1232. DOI: 10.1103/PhysRev.136.B1224. URL: http://link.aps.org/doi/10.1103/PhysRev.136.B1224.

Peters, P. C. and J. Mathews (1963). "Gravitational Radiation from Point Masses in a Keplerian Orbit". In: *Physical Review* 131, pp. 435–440. DOI: 10.1103/PhysRev.131.435.

Pfahl, E., P. Podsiadlowski, and S. Rappaport (2005). "Relativistic Binary Pulsars with Black Hole Companions". In: ApJ 628, pp. 343–352. DOI: 10.1086/430515. eprint: astro-ph/0502122.

Pilyugin, L. S., J. M. Vílchez, and T. Contini (2004). "Oxygen and nitrogen abundances in nearby galaxies. Correlations between oxygen abundance and macroscopic properties". In: A&A 425, pp. 849–869. DOI: 10.1051/0004-6361:20034522. eprint: astro-ph/0407014.

Pitkin, M. et al. (2011). "Gravitational Wave Detection by Interferometry (Ground and Space)". In: *Living Reviews in Relativity* 14, p. 5. arXiv: 1102.3355 [astro-ph.IM].

Plummer, H. C. (1911). "On the problem of distribution in globular star clusters". In: MNRAS 71, 460ÃÂÂ 470.

Porras, A. et al. (2003). "A Catalog of Young Stellar Groups and Clusters within 1 Kiloparsec of the Sun". In: AJ 126, pp. 1916–1924. DOI: 10.1086/377623. eprint: astro-ph/0307510.

Portegies Zwart, S. (2004). "The Ecology of Black Holes in Star Clusters". In: *ArXiv Astrophysics e-prints*. eprint: astro-ph/0406550.

Portegies Zwart, S. F. and S. L. W. McMillan (2002). "The Runaway Growth of Intermediate-Mass Black Holes in Dense Star Clusters". In: ApJ 576, pp. 899–907. DOI: 10.1086/341798. eprint: astro-ph/0201055.

Portegies Zwart, S. F., S. L. W. McMillan, and M. Gieles (2010). "Young Massive Star Clusters". In: ARA&A 48, pp. 431–493. DOI: 10.1146/annurev-astro-081309-130834. arXiv: 1002.1961 [astro-ph.GA].

Portegies Zwart, S. F. and F. Verbunt (1996). "Population synthesis of high-mass binaries." In: A&A 309, pp. 179–196.

Portegies Zwart, S. F. et al. (2001). "Star cluster ecology - IV. Dissection of an open star cluster: photometry". In: MNRAS 321, pp. 199–226. eprint: astro-ph/0005248.

Quinlan, G. D. (1996). "The dynamical evolution of massive black hole binaries I. Hardening in a fixed stellar background". In: New A 1, pp. 35–56. DOI: 10.1016/S1384-1076(96)00003-6. eprint: astro-ph/9601092.

Sadowski, A. et al. (2008). "The Total Merger Rate of Compact Object Binaries in the Local Universe". In: ApJ 676, pp. 1162–1169. DOI: 10.1086/528932. arXiv: 0710.0878.

Samsing, J., M. MacLeod, and E. Ramirez-Ruiz (2014). "The Formation of Eccentric Compact Binary Inspirals and the Role of Gravitational Wave Emission in Binary-Single Stellar Encounters". In: ApJ 784, 71, p. 71. DOI: 10.1088/0004-637X/784/1/71. arXiv: 1308.2964 [astro-ph.HE].

Siellez, K., M. Boër, and B. Gendre (2014). "Simultaneous event detection rates by electromagnetic and gravitational wave detectors in the advanced era of LIGO and Virgo". In: MNRAS 437, pp. 649–655. DOI: 10.1093/mnras/stt1915. arXiv: 1310.2106 [astro-ph.HE].

Sigurdsson, S. and L. Hernquist (1993). "Primordial black holes in globular clusters". In: Nature 364, pp. 423–425. DOI: 10.1038/364423a0.

Silva-Villa, E. and S. S. Larsen (2010). "The star cluster-field star connection in nearby spiral galaxies. I. Data analysis techniques and application to NGC 4395". In: A&A 516, A10, A10. DOI: 10.1051/0004-6361/201014267. arXiv: 1003.4626 [astro-ph.CO].

Spitzer, Jr. L. (1969). "Equipartition and the Formation of Compact Nuclei in Spherical Stellar Systems". In: ApJ 158, p. L139. DOI: 10.1086/180451.

Spitzer, Jr. L. and M. H. Hart (1971). "Random Gravitational Encounters and the Evolution of Spherical Systems. I. Method". In: ApJ 164, p. 399. DOI: 10.1086/150855.

Spitzer, L. (1987). *Dynamical evolution of globular clusters*.

Stiefel, E. (1971). *Linear and regular celestial mechnics*.

Vink, J. S. and A. de Koter (2005). "On the metallicity dependence of Wolf-Rayet winds". In: A&A 442, pp. 587–596. DOI: 10.1051/0004-6361:20052862. eprint: astro-ph/0507352.

Vink, J. S., A. de Koter, and H. J. G. L. M. Lamers (2001). "Mass-loss predictions for O and B stars as a function of metallicity". In: A&A 369, pp. 574–588. DOI: 10.1051/0004-6361:20010127. eprint: astro-ph/0101509.

von Hoerner, S. (1960). "Die numerische Integration des n-Körper-Problemes für Sternhaufen. I". In: ZAp 50, pp. 184–214.

Voss, R. and T. M. Tauris (2003). "Galactic distribution of merging neutron stars and black holes - prospects for short gamma-ray burst progenitors and LIGO/VIRGO". In: MNRAS 342, pp. 1169–1184. DOI: 10.1046/j.1365-8711.2003.06616.x. eprint: astro-ph/0303227.

Wang, J. B. et al. (2015). "Searching for gravitational wave memory bursts with the Parkes Pulsar Timing Array". In: MNRAS 446, pp. 1657–1671. DOI: 10.1093/mnras/stu2137. arXiv: 1410.3323.

Wang, Q.-D. (1991). "The global solution of the n-body problem". In: *Celestial Mechanics and Dynamical Astronomy* 50, pp. 73–88.

Weber, J. (1968). "Gravitational-Wave-Detector Events". In: *Phys. Rev. Lett.* 20 (23), pp. 1307–1308. DOI: 10.1103/PhysRevLett.20.1307. URL: http://link.aps.org/doi/10.1103/PhysRevLett.20.1307.

Yoshida, H. (1982). "A New Derivation of the Kustaanheimo-Stiefel Variables". In: *Celestial Mechanics* 28, pp. 239–242. DOI: 10.1007/BF01230677.

Zhu, X.-J. et al. (2014). "An all-sky search for continuous gravitational waves in the Parkes Pulsar Timing Array data set". In: MNRAS 444, pp. 3709–3720. DOI: 10.1093/mnras/stu1717. arXiv: 1408.5129.

Ziosi, B. M. et al. (2014). "Dynamics of stellar black holes in young star clusters with different metallicities - II. Black hole-black hole binaries". In: MNRAS 441, pp. 3703–3717. DOI: 10.1093/mnras/stu824. arXiv: 1404.7147.

Ziosi, Brunetto (2015). *sltools: StarLab Swiss Knife - v1.2*. DOI: 10.5281/zenodo.18980. URL: http://dx.doi.org/10.5281/zenodo.18980.